Abstract

NOWAK, JOSHUA MICHAEL. Examination of the Strontium Catalysis of Hydrino Reactions in a Capacitively-Coupled Audio-Frequency Cylindrical Plasma Discharge. (Under the direction of Prof. Mohamed A. Bourham).

Strontium catalysis may be an important aspect of a novel method of power production involving hydrino reactions. These reactions allow for the release of energy from hydrogen atoms as its electron falls to an energy state below the ground state. The thermal behavior of He-H plasmas with and without Sr present was examined. The plasmas were modeled as capacitors using the Drude model for the dielectric constant. The Joule heating of the plasmas was determined and compared with differential thermal energy to see what effect the addition of strontium had on the thermal output. Most results were inconclusive, but it was clear that plasmas with 1.01% H had a marked increase in thermal output when Sr was added. This means that there may be strontium catalysis of the hydrino process in this case and further experimentation should be done to rule out other explanations for this increase.

Examination of the Strontium Catalysis of the Hydrino Reaction in an Audio-Frequency, Capacitively Coupled, Cylindrical Plasma Discharge

by
Joshua Michael Nowak

A thesis submitted to the Graduate Faculty of
North Carolina State University
in partial fulfillment of the
requirements for the Degree of
Master of Science

Nuclear Engineering

Raleigh, NC

2009

APPROVED BY:

_____
J. Gilligan

_____ _____
M.A. Bourham G. Mitchell

(Chair of Advisory Committee) (Minor Representative)

Dedication

To James Pelliccio, Jr. for teaching me more than he will ever know.

Biography

Joshua Nowak was born in Philadelphia, Pennsylvania on December 24, 1982. He graduated from Coatesville Area Senior High School in Coatesville, Pennsylvania in June 2001. In August 2001, he began undergraduate studies at North Carolina State University in Raleigh, North Carolina. In May 2005, he graduated with a B.S. degree in Nuclear Engineering. In August 2005, he began graduate studies in the area of plasma science at North Carolina State University.

Acknowledgements

I would like to thank my parents for their continued support throughout all of my education. They have been a continued inspiration to me, and I could never have done this without them.

I would also like to thank Dr. M. A. Bourham. His enthusiasm inspired me to do research, and his never ending support has made everything that I have done possible. He has never been too busy to help in any way possible. I couldn't imagine a better advisor.

Thank you to Dr. J. Gilligan and Dr. G. Mitchell for agreeing to be on my advisory committee. It is greatly appreciated.

Finally, I would like to thank Mr. Joseph Hollowell who made me realize how much I could achieve.

Table of Contents

List of Figures

List of Tables

List of Appendices

Chapter 1

Introduction

The increased demand on energy worldwide is growing fast and it is imperative to seek out new energy sources and clean methods of energy production. The increased emphasis, both nationally [1] and internationally [2], on lowering greenhouse gas emissions, as well as the limited supply of resources, have made it clear that the burning of fossil fuels does not represent the future of energy production [3]. Solar power is a virtually endless source of energy. It is, however, prohibitively expensive, still at low efficiency and becomes even less efficient in certain geographic locations [4]. Wind power is even more prohibitive in its geographic availability though not as costly. Hydroelectric plants, though they do not produce greenhouse gases, greatly impact the surrounding environment because of the dams required, and not all locations are suitable for such power plants [4]. Even though they also produce no greenhouse gases, the world is not yet sold on nuclear power plants due to safety concerns as well as concerns about spent nuclear fuel, however, nuclear power is considered clean and at very high efficiency [4]. These issues with current sources of energy may be addressed with further research in the areas specific to each source. However, if a new, clean, and plentiful source of power can be established, it would be of great interest to bring cheap power to all parts of the world.

One novel method for energy production involves decreasing electron energy states which in turn releases electron energy in the forms of heat and light [5]. Normally, in order

for electrons to drop energy states thereby releasing energy, an input energy must be supplied to excite the electrons and increase electron energy states. The energy is then released as the electron de-excites and returns to its natural state [6,7]. A solution which requires no initial increase in energy states has been proposed and could revolutionize power production [8,9,10,11]. If electrons could drop to energy states below their natural state, they could release a nearly endless supply of energy. Recently, new energy states have been proposed for the hydrogen atom which could be used for such a means of energy production [12,13,14].

It is well characterized what higher energy states can be formed for a hydrogen atom (or any atom) by exciting its electron. These energy states exist at discrete energy levels, which are reached from lower energy states through energy absorption and are reached from higher energy states through radiation at discrete wavelengths. Using classical quantum mechanics, Randell L. Mills proposes that there exist energy states for the hydrogen atom below the ground state [5]. These lower energy states, like the ground state and unlike the excited states, are non-radiative energy states. The condition for radiation from a moving point charge requires that its space-time Fourier transforms contains components consistent with waves traveling at the speed of light. Therefore it is proposed that these non-radiative states require space-time Fourier transforms that do not contain components consistent with waves traveling at the speed of light [5]. Applied to these electron energy states and explained more plainly, radiative energy states require that photons be released, and non-radiative energy states require that no photons be released. This means that these lower

energy states cannot be reached from the ground state through purely photonic reactions. The ground state, being non-radiative, will not release a photon and reach a different energy level. These lower non-radiative states can, however, be reached via non-radiative mechanisms such as multipole coupling or a resonant collision mechanism [5,12,15]. In the same manner as the excited states, hydrogen's non-radiative energy states are quantized discretely. Therefore the non-radiative mechanism that causes hydrogen's electron to lose energy must absorb or transfer only certain discrete energies from the electron. These energies theoretically correspond to integer multiples of 27.2 eV [5]. In short, there exist energy holes at these discrete energies to produce these lower energy state hydrogen atoms known as hydrinos [5,12,15]. For the purposes of this experimental research, interactions with third party electrons will be examined.

Ionization energies corresponding to these discrete energies are an excellent source of energy holes for the transfer of energy from the hydrogen electron. There are many different atoms and ions that may provide the energy holes required through means of their ionization energies. These atoms and ions capable of providing such energy holes are known as catalysts. This experimental research deals, specifically, with the second ionization potential of helium (54.418 eV) and two combinations of ionization potentials for strontium. The combination of the second and third ionization potentials for strontium yields 53.92 eV, which is about a factor of 2 of the 27.2 eV, and the combination of the first through fifth ionization potentials yields 188.21 eV, which is about a factor of 4 of the 27.2 eV [5]. These catalysts absorb the energy from the hydrogen atom and then release this excess energy via

energetic electrons, which may in turn radiate producing photons and excess heat or provide excess electrical energy in the case of a plasma discharge, as in the experiment of this thesis.

Plasma is an ideal environment for hydrino reactions, it is an enclosed environment for the reaction to occur, and more importantly in this case, is the fact that the helium reaction (and one of the strontium reactions) requires the initial ionization to occur before it can absorb its secondary ionization potential from the hydrogen atom. It is also very advantageous to use plasma because of the high temperatures that are reached in a plasma environment. This increases the mobility of the atoms and ions, greatly increasing the chance of interaction with each other through collective mechanisms [5,8,9,12,16,17,18,19].

Chapter 2

Review of Literature

This literature review provides an explanation why it is important to research the effect of strontium and helium catalysis of the resonant energy transfer associated with the hydrino reaction in an audio frequency plasma discharge.

In a previous work by others, and using a microwave generated plasma, spectroscopic measurements were taken of pure gas discharges for hydrogen, nitrogen, oxygen, carbon dioxide, helium, neon, argon, krypton, and xenon [12]. These measurements were also taken using gas mixtures of the aforementioned gases with hydrogen, with ratios of 98% of the specific gas and 2% hydrogen; experiments were performed at two different pressures of 20 and 1 Torr. The measurements produced unknown peaks for the hydrogen-helium mixture only. These peaks were not observed for any of the other mixtures or pure gases. They were attributed by the authors to be a result of the production of hydrogen atoms whose electron exists at an energy state below the natural ground state of the hydrogen electron. A broadening of the Balmer α line (H_α, 656.281 nm wavelength) was also observed for the hydrogen-helium gas mixture. However, there was no observable broadening of any non-hydrogen lines [12]. This experiment was repeated using only helium, neon, argon, and xenon mixed with hydrogen at a ratio of 90/10, as well as pure hydrogen. In this case, the helium-hydrogen and argon-hydrogen gas mixtures "showed extraordinary broadening" of the H_α line [16,20].

In a second experiment, the exact operation of the test cell is difficult to discern from the experimenters' description [17]. It is, however, an alternating current discharge operating at 6 Hz and voltages below 115 V. Spectroscopic data were taken for hydrogen, argon and a mixture of hydrogen and argon. The measurements of hydrogen were also taken with the addition of strontium, sodium, magnesium, and barium separately. This was then repeated at 1 Torr for a mixture of argon and hydrogen with the addition of strontium at 77% and 23%, respectively. It was observed that in order to achieve the same output radiation intensity as per the case of hydrogen with strontium, more input energy of 4000, 7000, and 6500 times was required for the hydrogen with sodium, magnesium and barium, respectively [17]. It was also seen that the addition of argon to the hydrogen with strontium reduced the required input power by a factor of 2 to produce the same light output [17].

In another experiment, a tungsten filament in a quartz vacuum vessel was used to produce a chemically generated plasma. The filament was within a titanium mesh cylinder coated with a thin film of potassium carbonate [18]. In this experiment an excess broadening of the H_α line was observed for plasma discharges of hydrogen with strontium, hydrogen-helium, hydrogen-argon, hydrogen-helium with strontium, and hydrogen-argon with strontium. This broadening was not observed for pure hydrogen, hydrogen-krypton, hydrogen-xenon, or hydrogen with magnesium indicating the importance of the catalyst and the gas mixture to induce excess broadening of the H_α line [19].

Another experiment was conducted using a DC glow discharge at 2 Torr, in which broadening of the H_α line was observed for helium-hydrogen and argon-hydrogen gas

mixtures. Under the same conditions, no excessive broadening was observed for pure hydrogen or the xenon and neon hydrogen mixtures [16].

Excessive broadening of the H_α line was also seen for helium-hydrogen and argon-hydrogen gas mixtures in capacitively and inductively coupled radio frequency plasma discharges. Again, for these plasmas no excess broadening was observed for pure hydrogen, neon-hydrogen, or xenon-hydrogen gas mixtures [16].

It is clear from the H_α line broadening that there is increased hydrogen energy in plasmas containing hydrogen with helium, argon, or strontium for microwave generated plasmas [12,16], very low frequency AC plasmas [17], chemically generated plasmas [19], DC glow discharges [9)16], capacitively coupled RF discharges [16,20,21], and inductively coupled RF discharges [15,16]. There has, however, not been any experimentation with audio frequency discharges in the frequency range of 3-15 kHz, which is the subject research of this thesis.

Chapter 3

Experiments with Audio Frequency Discharge

3.1 Hypotheses

The examination of hydrogen-helium plasmas with strontium is important as experiments in the use of the hydrino process as a power source have shown promise with such catalysis [8,9]. The fact that the research performed with the aforementioned plasma generation techniques has yielded promising results shows that there is a need for more research, especially at the audio frequency range of 3-15 kHz, which has not yet been tested by any other researchers. It is intended to further the knowledge regarding the catalysis of the hydrino reaction by expanding the plasma sources examined to include audio frequency discharges. The spectroscopic equipment used in this examination is two Ocean Optics HR2000 fixed grating spectrometers. Both spectrometers are fitted with a 600 line/mm grating, 25μm slit and Ocean Optics L2 internal lens to focus the light onto the CCD. The grating of the UV-VIS spectrometer is blazed at 500 nm and views the wavelengths between 300 nm and 736 nm. The VIS-NIR spectrometer has a range of 600 nm to 1025 nm with the grating blazed at 750 nm. The spectrometers are power calibrated using an Ocean Optics LS-1-CAL lamp. However, the precision of these spectrometers is not as high as the equipment used in the experiments conducted by other researchers and referenced elsewhere [8,12,16,17,18,19,21]. Therefore, the heat flow will also be analyzed to determine what energy increase, if any, occurred during the catalysis.

3.2 Delimitations

The experiment in this thesis work is not meant to determine whether the hydrino reaction is, in fact, occurring but it assumes that the hydrino theories are true and catalysis of hydrogen is taking place in the presence of helium and strontium. This experimental research is intended to increase the data on this novel process by adding another power source operating in the audio frequency range of 3-15 kHz to those already examined by other researchers. The catalysis data, consisting of temperature change, electrical input, and spectroscopy; will be analyzed and compared with control data obtained under the same conditions as the catalysis data. The models for the plasma and sheath permittivities are simplified models to provide reasonable approximations for the purpose of comparing the electrical energy absorbed by the plasmas versus any heat generation from the plasma.

3.3 Experimental Setup

The experimental device is a coaxial discharge composed of a 1½-inch glass tube with 2¾-inch vacuum flanges at each end. Figure 1 shows a conceptual drawing of the discharge chamber in which a central electrode serves as the high voltage electrode and an inner mesh serves as the ground, the discharge is formed between the central electrode and an inner cylindrical mesh.

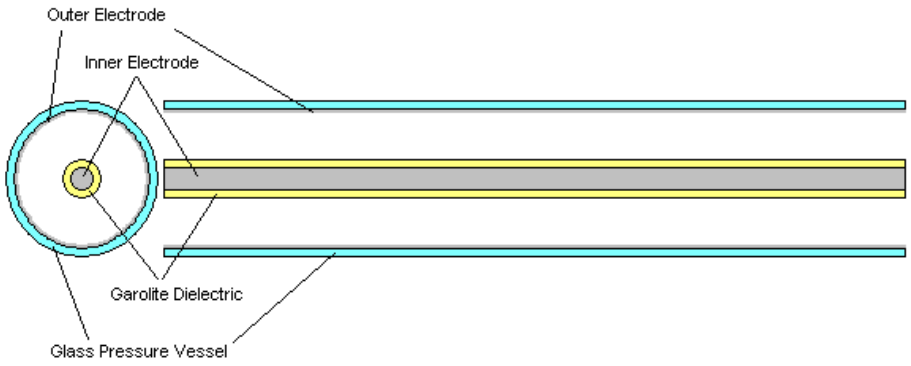

Figure 1 Conceptual drawing of the discharge chamber

The central electrode is 3/16-inch diameter stainless steel rod. Two insulated end caps composed of Garolite G-10 support the weight of the inner electrode and prevent arcing near the grounded end flanges. The inner electrode may be covered in a dielectric material with a 0.25-inch outer diameter to operate the discharge in the dielectric-barrier mode. The end caps limit the discharge to a 30 cm visible region through the glass tube. The inside of the glass tube is covered with a stainless steel mesh welded to the metal ends of the glass tube, connected to ground through the outer vacuum chamber, and serves as the outer electrode. The HV transformer steps up the voltage with a ratio of 125:1 from a 1 kW audio frequency TITAN Series power supply (Compact Power, Inc.). The device is capable of supplying 11 kV_{RMS} at 90 mA_{RMS}. The power supply can operate with up to 4 A_{RMS} at 260 V_{RMS}. Figure 2 shows a drawing of the device in which gas inlet and outlet are shown and the location of the thermocouples to monitor inlet and outlet temperatures.

Diagnostics include a Tektronix P6015A HV probe to measure the voltage across the discharge, and a Pearson coil (Pearson Electronics, Inc Model 2100) to measure the current

flowing through the discharge. A Baratron gauge (MKS Series 902, 0-1000 Torr) is mounted on the discharge inlet to measure the pressure in the test cell. The working gas flows into the cell through MKS flow controllers with typical setup uses two 500 sccm (N_2) MKS 1179A flow controllers to deliver the supply gases. A mechanical pump (200 cfm) is adequate to reduce the pressure below the zero of the Baratron gauge. A fiber optic feedthrough allows direct examination of the plasma through a 600μm optic fiber (250 nm-800 nm). The optical signal is routed to an Ocean Optics HR2000 spectrometer (600 line/mm) through a 400 μm batch cord (10m length). The spectrometer is absolutely calibrated using the Ocean Optics LS-1-CAL lamp. In addition to optical diagnosis, two K-type contact thermocouples are mounted at the inlet and the outlet for direct measurement of the ambient gas temperature.

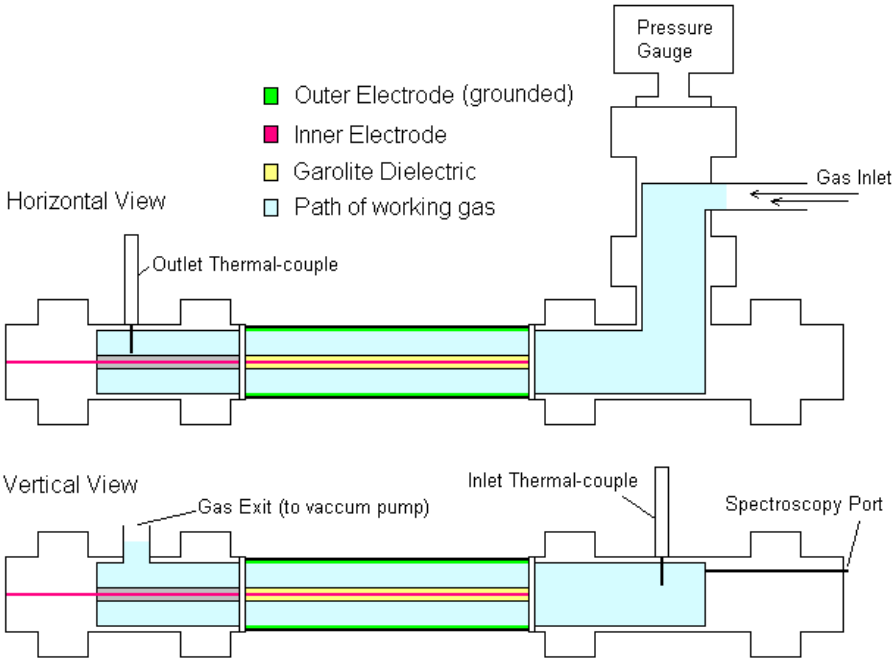

Figure 2 Detailed drawing of the experimental setup showing vacuum connections, inlet and outlet thermocouples and spectroscopy access

The electric system uses a TITAN hybrid switchmode AC power supply with built-in function generator operating in the frequency range 45 Hz – 15 kHz. The power supply can provide up to 8 Amp current in 2 switchable modes, 0-130 V or 0-260 V. The design can provide up to 12 kV, and higher, to induce breakdown in a dielectric-barrier discharge (DBD) at atmospheric pressure, however, lower voltages of 1-3 kV are sufficient for low pressure and vacuum operations. The electrodes are coupled to the output of the 2 out-of-phase (180^{o} out-of-phase) transformers; each provides half of the required voltage. The design uses two AD6286 high voltage transformers, 10 kV insulation; each has a step-up ratio of 1:125. The transformers are center-tapped to ground and the input leads are coupled to the source that provides variable frequency input at adjustable voltage. The output is coupled to a step-down transformer to adjust the output to a maximum of 110 V, which is the maximum allowable input to the out-of-phase transformers. The switchmode power supply provides 130 V or 260 V sinusoidal output at a selected pre-set frequency between 4 - 15 kHz, and the output is fed to the step-down transformer to adjust the output to 50 V input to the out-of-phase transformers, which in turn will provide 6.25 kV on each transformer output and hence the peak-to-peak voltage on the electrodes will be 12.5 kV. Figure 3 shows the electrical circuit of the system in which the plasma discharge is modeled as a capacitor filled with plasma and has a dielectric constant determined by the nature of the generated plasma.

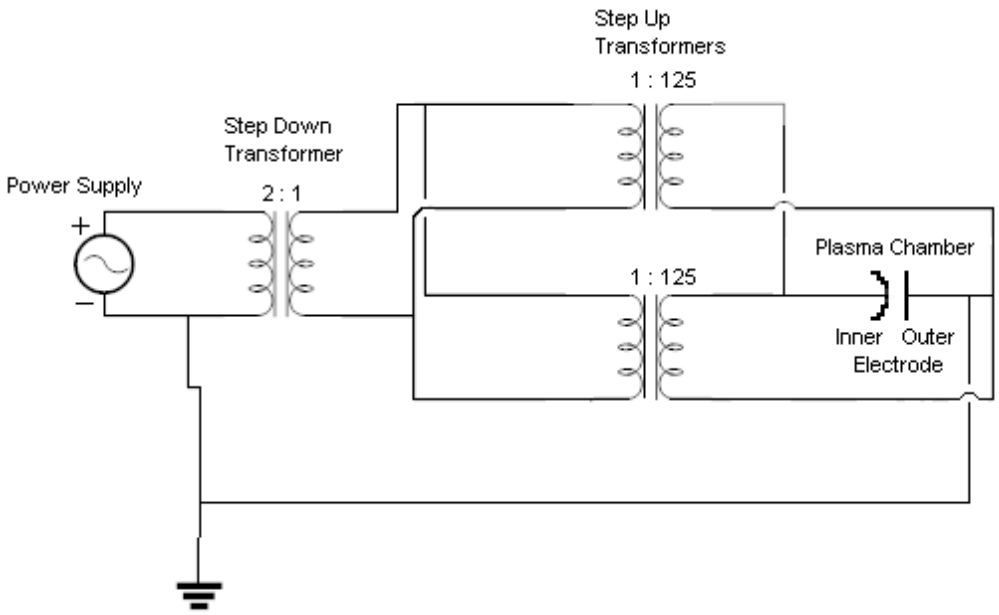

Figure 3 Electrical circuit of the system showing the power supply, step-down transformer, out-of-phase transformers and the plasma chamber modeled as a capacitor

Discharge current and voltage are always sinusoidal with typical 90^o phase between the voltage and current indicating the capacitive behavior of the test cell. The capacitance of the plasma in the coaxial system, C_{cell}, is a simplified capacitance of a cylindrical geometry in which the permittivity is that of the plasma $\varepsilon_{plasma} = \varepsilon_o k_{plasma}$, where ε_o is the permittivity of free space and k_{plasma} is the plasma dielectric constant. Typical waveforms are shown in Figure 4 for a pure helium discharge, where the current wave form shows the breakdown features at the peak value of each half cycle. A picture of pure helium discharge at a base pressure of 1.0 Torr and a discharge current of 30 mA is shown in Figure 5, in which it is clear the discharge is uniform over its entire length.

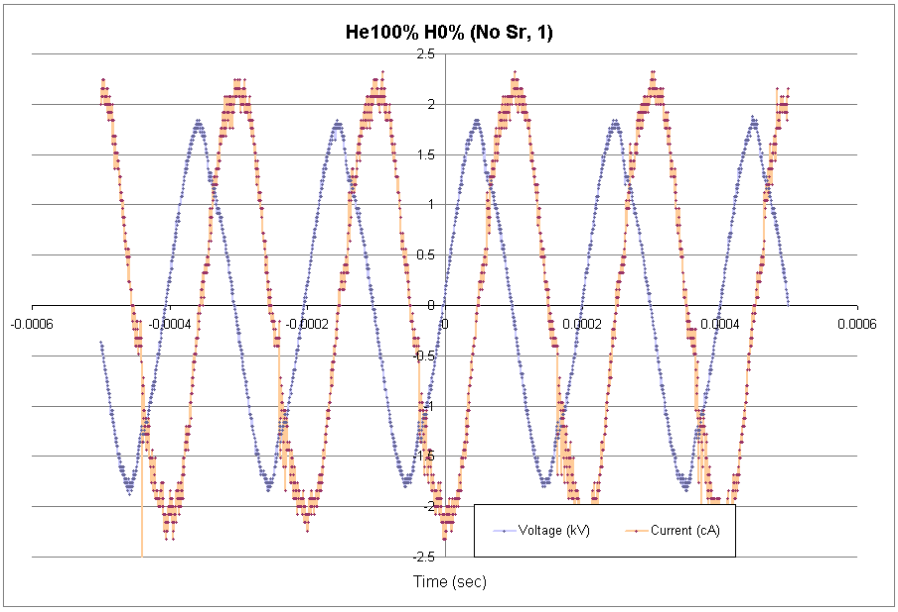

Figure 4 Typical waveforms for a pure helium discharge in the test cell

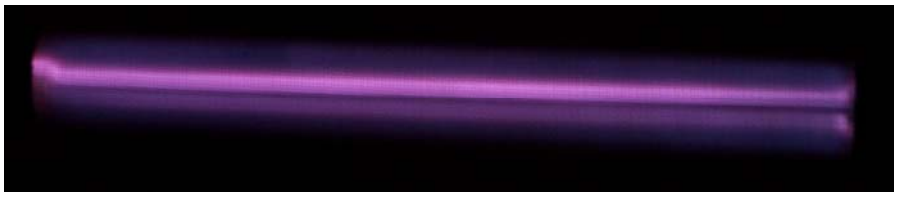

Figure 5 Picture of a helium discharge at 1.0 Torr and 30mA discharge current

3.4 Experimental Procedure

There were two sets of data taken. Each set of data was comprised of plasmas containing pure helium as well as helium-hydrogen mixtures in which 1.01, 2.00, 2.97, 3.92, and 4.86% hydrogen was used. For each experimental test the chamber was evacuated to base pressure, few milli-Torr then the gas or gas mixture was allowed to flow. The operating frequency was kept at 5 kHz for all experiments. Discharge current and voltage were monitored and recorded for each data set, and thermocouple readings were continuously monitored to record the temperature of the inlet and outlet for sufficient time to reach thermal equilibrium. After thermal equilibrium was reached, the voltage and current waveforms were saved and transferred to spreadsheets for analysis. This process was repeated for each gas mixture with time in between to allow the chamber to reach thermal equilibrium with the environment. The entire process was then repeated for each gas mixture with strontium present on the outer electrode to determine the effect of strontium as a catalyst in excess energy release from the discharge.

The procedure for the second data set was identical but for a few minor exceptions. The chamber was not allowed to reach thermal equilibrium with the environment between gas mixtures. This was changed in hopes that the strontium would corrode less because even though the chamber was kept under vacuum, it was seen that the strontium corroded greatly over the course of data set 1. Also, for the second data set, spectral data were taken for each experiment.

Chapter 4

Plasma Model

As the focus of this project is whether or not there is an increase in energy output per unit of energy input for plasmas containing hydrogen with catalysts present, the amount of electrical energy that is transferred to the plasma must be determined. Joule (Ohmic) heating is the main mechanism for the energy input for unmagnetized weakly ionized plasma, which is the typical mechanism for cold plasmas where the resistivity is relatively high. The electron conductivity of weakly-ionized plasma is determined, primarily, by the electron-neutral collision and hence the conductivity equation may be given by the following equation [22].

$$\sigma = \frac{n_e e^2}{m_e \nu_{en}} \tag{1}$$

Where e is the unit charge of the electron, n_e is the electron number density, m_e is the mass of the electron, and ν_{en} is the electron-neutral collision frequency. This leads to a good approximation for the power input into the plasma through Joule heating [22].

$$P_{(per\ unit\ volume)} = \frac{n_e e^2}{m_e \nu_{en}} E^2 \tag{2}$$

where E is the electric field. This power per unit volume will be integrated over the plasma volume and the electric field is determined from the voltage across the discharge. Hence, Eq. 2 will have two unknowns, the electron-neutral collision frequency ν_{en} and the electron number density n_e. These two important parameters can be determined from an equivalent

electric circuit model of the discharge and the permittivity equation of the plasma. To put an equivalent circuit model, one can start from setting up the impedance equation for an oscillatory AC discharge as

$$Z = \frac{V_0}{I_0} e^{i\varphi} \tag{3}$$

where Z is the complex impedance of the circuit, V_0 is the amplitude of the applied voltage, I_0 is the amplitude of the current, and φ is the phase angle between the current and voltage. Due to the fact that the test cell is capacitively coupled to the power supply, then it is reasonable to model the plasma as a series of capacitors with complex dielectric constants, then the equivalent circuit impedance is given by

$$Z = \frac{1}{i\omega C} \tag{4}$$

where C is the total equivalent capacitance of the circuit [23,24,25]. This equivalent capacitance is composed of three capacitors, capacitance of the insulator C_g, which is made of garolite, the plasma sheath capacitance C_{sheath}, and the bulk plasma capacitance C_p. Hence, the circuit impedance is given by

$$Z = \frac{1}{i\omega}\left(\frac{1}{C_g} + \frac{1}{C_{sheath}} + \frac{1}{C_p}\right) \tag{5}$$

As the discharge is coaxial, the capacitance of a cylindrical capacitor $C = \varepsilon \frac{2\pi L}{\ell n[c/b]}$ is used to substitute for the individual capacitances in the discharge impedance of Eq. 5, where.

L is the length of the capacitor, b and c are the inner and outer radii, respectively, and ε is the permittivity of the material. For the coaxial discharge, shown in Figure 6, the impedance equation will be given by

$$Z = \frac{1}{i2\pi\omega L\varepsilon_o}\left(\frac{\ell n[b/a]}{\varepsilon_g/\varepsilon_o} + \frac{\ell n[c/b]}{\varepsilon_{sheath}/\varepsilon_o} + \frac{\ell n[d/c]}{\varepsilon(\omega)/\varepsilon_o}\right) \tag{6}$$

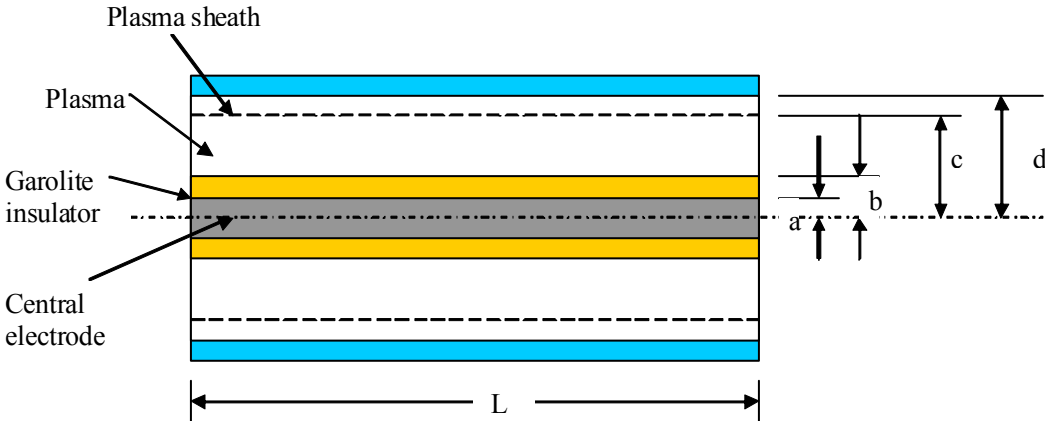

Figure 6 Discharge chamber showing inner electrode, garolite insulator, plasma region and plasma sheath at the boundary between plasma and chamber outer wall

There are currently no models for the permittivity of a cylindrical low frequency plasma sheath. However, it is shown by Lieberman and Lichtenberg that in a low frequency plasma the displacement current is negligible. This means that the sheath is resistive, not capacitive [26]. Eq. 6 can now be written as

$$Z = \frac{1}{i\omega 2\pi L\varepsilon_0}\left(\frac{\ell n\left[\frac{b}{a}\right]}{\varepsilon_g/\varepsilon_0} + \frac{\ell n\left[\frac{c}{b}\right]}{\varepsilon(\omega)/\varepsilon_0}\right) + R_{Sheath} \tag{7}$$

A model was developed assuming that the frequency is low enough such that the sheaths act more like DC plasma sheaths rather than RF plasma sheaths.

The plasma sheath capacitance was derived using the DC plasma sheath model with a time varying voltage and current. This is a good approximation because the operating frequency is low enough for the electron and ions to fully react to each cycle [26,27,28].

The permittivity of the garolite material is known, and therefore what is remaining in the impedance equation is the permittivity of the plasma itself.

The Drude Model was used to determine the permittivity of the plasma. This model takes into account the frequency of the applied voltage, the restoring force of a resonant (natural) frequency for the electrons, and the drag created by collisions in the plasma [23]. Because this is weakly ionized plasma, the collision frequency can be approximated as the electron-neutral collision frequency, and the equation for this model becomes,

$$\frac{\varepsilon(\omega)}{\varepsilon_o} = 1 + \frac{\omega_p^2}{\left(\omega_o^2 - \omega^2 - i\omega\nu_{en}\right)} \tag{8}$$

Where ε_o is the permittivity of free space, ω_o is the resonant frequency, ω is the frequency of the applied field, and ω_p is the electron plasma frequency given by,

$$\omega_p^2 = \frac{ne^2}{m\varepsilon_o} \tag{9}$$

This resonant frequency is caused by the binding energy that the atom exerts on the electron. Since the current is carried by the free electrons in the plasma, there is no resonant frequency, and hence $\omega_o = 0$. This simplifies the equation slightly; however there is a great deal of

algebra to obtain a useful form of the impedance. Eliminating the resonant frequency the Drude model becomes

$$\frac{\varepsilon(\omega)}{\varepsilon_o} = \frac{\left(-\omega^2 - i\omega\nu_{en}\right) + \omega_p^2}{\left(-\omega^2 - i\omega\nu_{en}\right)} \tag{10}$$

Inversing Eq. 10 one gets $\frac{1}{\varepsilon(\omega)/\varepsilon_o} = \frac{\left(-\omega^2 - i\omega\nu_{en}\right)}{\left(\omega_p^2 - \omega^2 - i\omega\nu_{en}\right)}$ which yields

$\frac{1}{\varepsilon(\omega)/\varepsilon_o} = \frac{\left(\omega^4 - \omega^2\omega_p^2 + \omega^2\nu_{en}^2\right) - i\omega\omega_p^2\nu_{en}}{\left(\omega_p^2 - \omega^2\right)^2 + \omega^2\nu_{en}^2}$ to separate the real and imaginary parts.

Substituting into the impedance equation one gets:,

$$Z = \frac{1}{i\omega 2\pi L\varepsilon_0}\left(\frac{\ell n\left(\frac{b}{a}\right)}{\left(\varepsilon_g/\varepsilon_0\right)} + \ell n\left(\frac{c}{b}\right)\frac{\omega^4 - \omega^2\omega_p^2 + \nu_{en}^2\omega^2 - i\nu_{en}\omega\omega_p^2}{\left(\omega_p^2 - \omega^2\right)^2 + \nu_{en}^2\omega^2}\right) + R_{Sheath}$$

, which can be separated into its real and imaginary parts as shown in Eq. 11 below:

$$Z = \frac{1}{2\pi\omega L\varepsilon_o}\left(\frac{\nu_{en}\omega\omega_p^2}{\left(\omega^2 - \omega_p^2\right)^2 + \omega^2\nu_{en}^2}\ell n\left[\frac{c}{b}\right] - i\left[\frac{\varepsilon_o}{\varepsilon_g}\ell n\left[\frac{b}{a}\right] + \frac{\left(\omega^4 - \omega^2\omega_p^2 + \omega^2\nu_{en}^2\right)}{\left(\omega^2 - \omega_p^2\right)^2 + \omega^2\nu_{en}^2}\ell n\left[\frac{c}{b}\right]\right]\right) \tag{11}$$

Defining the real part

$$\alpha = \frac{1}{2\pi\omega L\varepsilon_o}\left(\frac{\nu_{en}\omega\omega_p^2}{\left(\omega^2 - \omega_p^2\right)^2 + \omega^2\nu_{en}^2}\right)\ell n\left[\frac{c}{b}\right] + R_{sheath} \tag{12}$$

And the imaginary part

$$\beta = \frac{-1}{2\pi\omega L\varepsilon_o}\left(\frac{\varepsilon_o}{\varepsilon_g}\ell n\left[\frac{b}{a}\right]+\frac{\left(\omega^4-\omega^2\omega_p^2+\omega^2\nu_{en}^2\right)}{\left(\omega^2-\omega_p^2\right)^2+\omega^2\nu_{en}^2}\ell n\left[\frac{c}{b}\right]\right) \tag{13}$$

Then the impedance is given by $Z=\alpha+i\beta=\frac{V_o}{I_o}e^{i\phi}$ from which $\frac{V_o}{I_o}=\left(\alpha^2+\beta^2\right)^{\frac{1}{2}}$ and $\tan(\phi)=\frac{\beta}{\alpha}$. By setting the real and imaginary parts to be equal to each other, then $\alpha=\frac{V_0}{I_0}\cos(\phi)$ and $\beta=\frac{V_0}{I_0}\sin(\phi)$.

In Eq. 12, the sheath resistance may be neglected and hence, and upon substitution for $\alpha=\frac{V_0}{I_0}\cos(\phi)$ in Eq. 12 yields an equation with three unknowns: electron number density (n_e), electron-neutral collision frequency (ν_{en}), and the plasma sheath thickness (s_b).

$$\frac{V_0}{I_0}\sin(\phi)=\frac{1}{\omega 2\pi L\varepsilon_0}\left(\frac{\ell n\left(\frac{b}{a}\right)}{\left(\varepsilon_g/\varepsilon_0\right)}+\ell n\left(\frac{s_b}{b}\right)\frac{\omega^4-\omega^2\left(\frac{n_e e^2}{m\varepsilon_0}\right)+\nu_{en}^2\omega^2}{\left(\left(\frac{n_e e^2}{m\varepsilon_0}\right)-\omega^2\right)^2+\nu_{en}^2\omega^2}\right) \tag{14}$$

Measured, known, values for this equation are the amplitude of the current and voltage and the phase angle, and one can solve these equations to obtain the electron-neutral collision frequency as well as the electron number density.

The electron-neutral collision frequency is determined by $\nu_{en}=n_n v_e\sigma$, where n_n is the number of neutral atoms, v_e is the electron velocity and σ is the collision cross section. The

number of neutral atoms is obtained from the ideal gas law $n_n = \frac{P}{kT}$ with parameters taken at the gas inlet.

The electron velocity is taken to be the average thermal velocity $\bar{v}_e = \sqrt{\frac{8kT_e}{\pi m}}$ and the collision cross section, is determined from [29], [30], and [31]. Combining these equations yields an equation whose only unknown is the electron temperature (T_e), hence the electron-neutral collision frequency is given by $\nu_{en} = \sigma \frac{P}{kT}\sqrt{\frac{8kT_e}{\pi m}}$.

The electron temperature in such discharge is assumed to be around 1.0 eV, which allows for a solution for the electron number density. This number density is then compared to the Saha equation $\frac{n_i}{n_n} = 2.4\times10^{21}\frac{T^{3/2}}{n_i}e^{-U_i/kT}$ from [32] with the quasi-neutrality assumption $n_e = n_i$ a, and therefore $n_i = \sqrt{n_n \cdot 2.4\times10^{21}T^{3/2}e^{-U_i/kT}}$. The electron temperature is iterated in the ion number density equation $n_i = \sqrt{n_n \cdot 2.4\times10^{21}T^{3/2}e^{-U_i/kT}}$ until an agreement is reached between the electron number density and the electron number density from Eq. 14.

Up to this point, it is assumed that the plasma sheath has no dimension which is obviously not physical. This assumption, however, can be corrected. The maximum sheath thickness can be found by assuming that the plasma is a DC plasma, which is a fair assumption here because the frequency of the applied electric field is low enough that the sheath is allowed to form fully during each cycle [26,27,28].

Poisson's Equation must be solved in cylindrical coordinates for the sheath. $\nabla \cdot E = \frac{\rho}{\varepsilon_0}$, where $\rho = en_s$ and n_s is the number density at the sheath edge. Putting the divergence in cylindrical coordinates and using $E = -\nabla V$ Poisson's becomes $-\frac{1}{r}\frac{\partial}{\partial r}\left(r\frac{\partial V}{\partial r}\right) = \frac{en_s}{\varepsilon_0}$, and upon integration over r from the sheath edge (s_b) to r' and assuming that the voltage difference at the plasma sheath boundary is zero one gets:

$$-\left(r'\frac{\partial V}{\partial r'}\right) = \frac{en_s}{2\varepsilon_0}\left(r'^2 - s_b^2\right)$$

The integrating over r' from s_b to c and assuming that the voltage difference across the sheath is approximately $-V_0$ yields

$$V_0 = \frac{en_s}{2\varepsilon_0}\left(\frac{s_b^2 - c^2}{2} + s_b^2 \ell n\left[\frac{c}{s_b}\right]\right) \tag{15}$$

Here it is assumed that $n_s = n_i = n_e$ (quasi-neutrality approximation). The solution for n_e from Eq. 14 is substituted into Eq. 15. The sheath thickness is solved for and used in Eq. 14 and into the collision frequency equation $\nu_{en} = \sigma \frac{P}{kT}\sqrt{\frac{8kT_e}{\pi m}}$ to find a new n_e. The equations are then iterated until agreement is reached. A Maple math program was used to solve these equations and the program is included in Appendix F.

An expression for the electric field for a cylindrical capacitor can be introduced as

$$E = \frac{\Delta V}{r\ \ell n[c/b]} \tag{16}$$

Where ΔV is the real part of the voltage difference and is given by $\Delta V = V_o Sin(\omega t)$ and hence the integration of Eq. 2 $P_{(per\ unit\ volume)} = \frac{n_e e^2}{m_e \nu_{en}} E^2$ over the volume yields

$$P = \int_0^L \int_0^{2\pi} \int_b^c \frac{n_e e^2}{m_e \nu_{en}} \frac{V_o^2 Sin^2(\omega t)}{\left[\ell n(c/b)\right]^2 r^2}\, dr\, d\varphi\, dz \tag{17}$$

Upon integration one obtains the electric input power to the plasma due to Joule heating

$$P_{(Watts)} = \frac{n_e e^2}{m_e \nu_{en}} \frac{V_o^2 Sin^2(\omega t)}{\left[\ell n(c/b)\right]} 2\pi L \tag{18}$$

where n_e and v_{en} can been obtained from simultaneously solving the equations for the real and imaginary impedances (Eqs. 12 and 13).

The change in the thermal energy ΔQ, in joules, for the working gas can be shown to be $\Delta Q = C_p n \Delta T$ where n is the total number of gas molecules, C_p is the heat capacity of the gas at constant pressure, and ΔT is the change in temperature from the inlet to outlet of the gas. The total number of gas molecules flowing through the volume per unit time $\dot{n}$ can be approximated using the ideal gas law $\dot{n} = \frac{P\dot{V}}{RT}$, where P is the pressure at the inlet, $\dot{V}$ is the volumetric flow rate (taken from the mass flow controller readout), T is the temperature at the inlet, and R is the universal gas constant. The heat capacity of the gas must be corrected for the gas ratios and temperature, which takes into consideration the flow rates of the helium and hydrogen. The flow rate readings are corrected using the gas and thermal correction factors given by the manufacturers (MKS) of the mass flow controller, these values are 1.0 for helium and 1.01 for hydrogen. Therefore the corrected C_p can be given

by $C_p = \frac{(FR)_{He} C_{p(He)} + (FR)_{H_2} C_{p(H_2)}}{(FR)_{He} + (FR)_{H_2}}$, where $(FR)_{He}$ and $(FR)_{H2}$ represents the flow rates of helium and hydrogen, respectively. Hence, the thermal energy per unit time is given by

$$\Delta\dot{Q} = \frac{(FR)_{He} C_{p(He)} + (FR)_{H_2} C_{p(H_2)}}{(FR)_{He} + (FR)_{H_2}} \cdot \frac{P\left((FR)_{He} + (FR)_{H_2}\right)}{RT} \Delta T \qquad (19)$$

The Joule heating is expressed in terms of time *t*. This can be averaged out because it is in the form of a sine squared; the average of which is simply ½.

$$P_{(Ave)} = \frac{1}{2} \frac{n_e e^2}{m_e \nu_{en}} \frac{V_o^2}{\left[\ell n(c/b)\right]} 2\pi L \qquad (20)$$

The ratio of thermal energy (Eq. 17) to the electrical energy input (in the form of Joule heating, Eq. 18) gives the energy output per energy input under steady state conditions. This ratio can be compared for experiments with and without strontium to show how the addition of strontium affects the thermal output. If the thermal output per electrical input coming from Joule heating is assumed constant, then any increase in thermal output per electrical input would have to come from another source such as chemical reactions or the hydrino reaction. It is also important to compare each experiment with hydrogen present to its counterpart of pure helium.

Chapter 5

Experimental Results and Discussion

Experimental data includes electrical (voltage and current), thermal (inlet and outlet flow temperatures) and optical emission spectroscopy. This chapter discusses experimental data and the analysis performed to acquire useful information such as obtaining the root mean square for the voltage and current waveforms, the phase difference between the voltage and current, and the temperature differences between the inlet and outlet flow. Full documentation of all experimental data, wave forms, temperatures and optical emission spectra are found in the appendices. Discussion of experimental results is also included in this chapter to assess the thermal behavior of the discharge.

Voltage and Current Measurements

Typical waveforms of the discharge voltage and current are shown in Figure 7 for 100% Helium discharge without having any catalyst inside the discharge cell (no Strontium in the test cell). The voltage was measured using a Tektronix P6015A compensated capacitively-coupled high voltage probe Model TDS 2024 ratio 1:1000, and the current was measured via a

Pearson coil Model 2877 ratio 1V/1Amp. The waveforms were obtained by coupling the measuring sensors (voltage and current) to a Tektronix digital oscilloscope, which is connected to computer running WaveStar® software and converting data into an Excel spreadsheet. As shown in Figure 7, the voltage waveform is smoother than the current

waveform due to the series of breakdowns that appears on the current more than that on the voltage. The phase angle between the current and voltage is approximately 90^{o}, typical for this discharge.

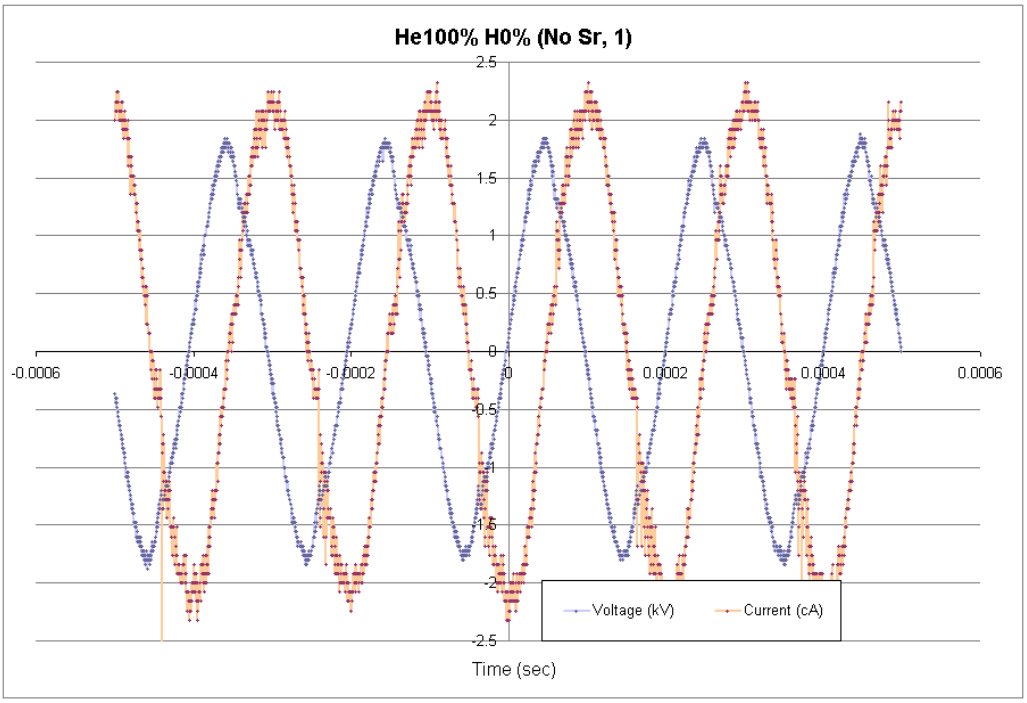

Figure 7 Voltage and current waveforms for 100% helium discharge, no strontium in the test cell

Figure 8 shows the current and voltage waveforms when 1.01% hydrogen is added to the discharge, in absence of strontium in the cell. It is clear from the figure that the current and voltage waveforms are not altered, which verifies that the electrical nature of the discharge is kept unchanged.

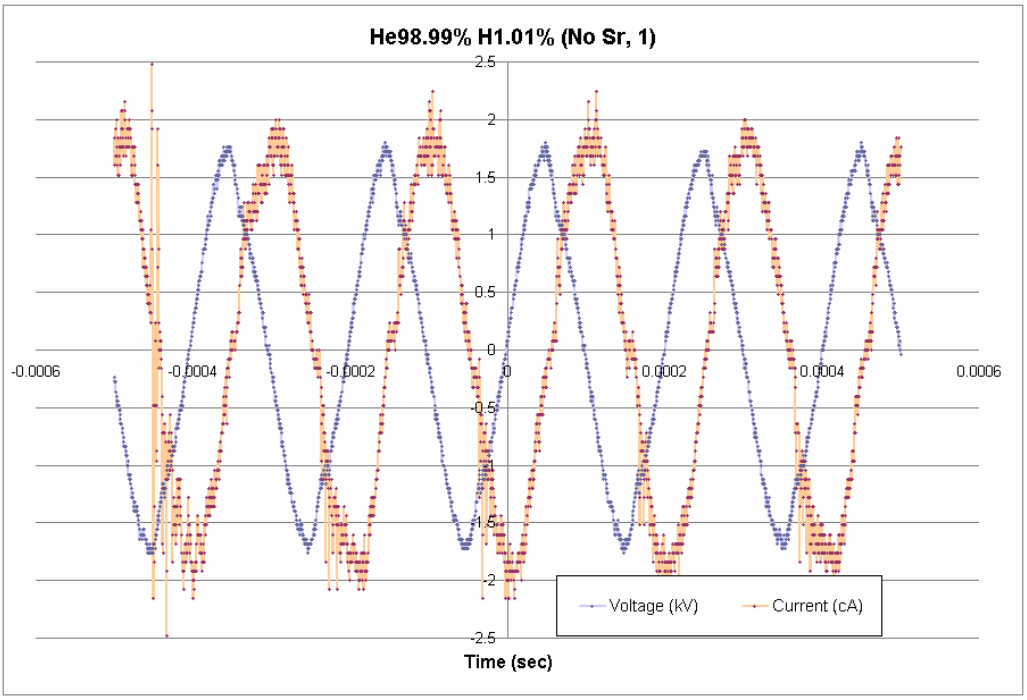

Figure 8 Voltage and current waveforms for 98.99% helium + 1.01% hydrogen discharge, no strontium in the test cell

Figure 9 shows the current and voltage waveforms when 1.01% hydrogen is added to the discharge, in presence of strontium in the cell. Again, it is clear that the current and voltage waveforms are not altered, which verifies that the electrical nature of the discharge is kept unchanged even with the addition of strontium into the cell. Similar results were obtained when the hydrogen percent was increased to 4.86% as shown in Figure 10.

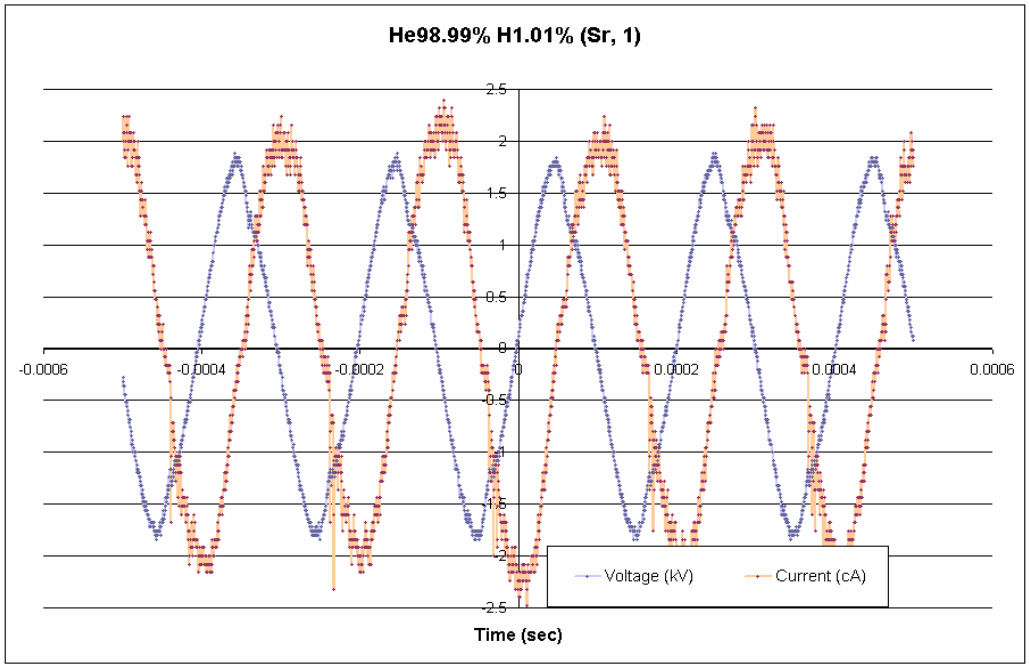

Figure 9 Voltage and current waveforms for 98.99% helium + 1.01% hydrogen discharge, with strontium in the test cell

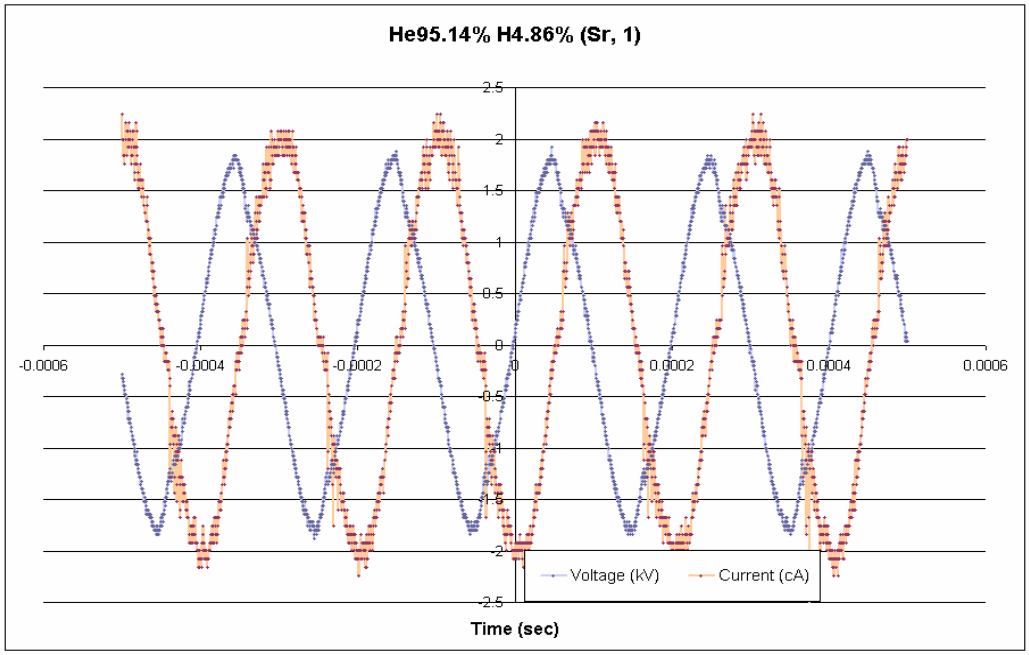

Figure 10 Voltage and current waveforms for 95.14% helium + 4.86% hydrogen discharge, with strontium in the test cell

In order to determine the RMS values of the voltage and current, the average of the square of the waveforms over two cycles was calculated and the square root of this value is taken as the RMS value of each waveform. This was performed for all of the waveforms obtained during all experiments with and without catalysts, including experiments with gas mixtures. Tables 1 and 2 show these values for date sets 1 and 2 in which strontium metal was inserted in the discharge as a catalyst, the data sets include varying the hydrogen content in the helium discharge up to 4.86% by volume. Data set 1 used an applied voltage of ~1.85 kV and Data set 2 used ~1.75 kV, and the discharge chamber was allowed to reach thermal equilibrium. As seen from Tables 1 for operation at greater than 1.8 kV, the voltage and current magnitudes are reduced when the catalyst (strontium) is inserted in the discharge at all hydrogen fractions. The data for pure helium discharge with strontium were erroneous thereby making the voltage and current data superfluous and thus were not counted. In Table 2 for operation in the range of 1.7 kV, where the chamber was not allowed to reach thermal equilibrium, the reduction with insertion of strontium metal is less than that observed in Data set 1, also the current is much less than that of Data set 1. However, the reduction in the voltage and current with insertion of strontium could be explained in terms of less discharge power would be needed with strontium under the assumption that strontium may provide excess energy to the discharge.

The data for all experiments, with and without catalysts, are shown in Appendices A and B.

Table 1: RMS Current and Voltage; Data Set 1

Data Set 1: RMS Voltage and Current

	With Strontium		Without Strontium	
	V (kV)	I (mA)	V (kV)	I (mA)
H 0%	N/A	N/A	1.8237	23.715
H 1.01%	1.8352	22.336	1.7401	20.377
H 2.00%	1.8507	22.325	1.7500	21.080
H 2.97%	1.8277	21.970	1.7380	21.241
H 3.92%	1.8579	22.444	1.7268	20.844
H 4.86%	1.8438	22.520	1.7440	21.811

Table 2: RMS Current and Voltage; Data Set 2

Data Set 2: RMS Voltage and Current

	With Strontium		Without Strontium	
	V (kV)	I (mA)	V (kV)	I (mA)
H 0%	1.76150	18.710	1.73540	18.868
H 1.01%	1.73655	18.636	1.75312	19.929
H 2.00%	1.73360	18.815	1.73270	19.799
H 2.97%	1.72765	18.550	1.74390	19.510
H 3.92%	1.75030	19.110	1.74590	19.060
H 4.86%	1.74570	18.640	1.75540	19.390

Gas Temperature Measurements

Temperatures of the inlet and the outlet were measured using Omega Engineering thermocouples Model TAC 30K with A/D converters. Both thermocouples were placed at the inlet and outlet outside the plasma region, thus measuring the temperature of the gas as it flows to or from the plasma region.

A sample of the measured inlet (blue) and outlet (green) temperatures taken during a test in which 100% helium was used for the discharge and in absence of catalyst (no

strontium in the discharge) is shown in Figure 11. It is clear from the figure that the temperature of the outlet is only about 1.87 ºC higher than that of the inlet, indicating no appreciable heat generation.

For a test in which 98.99% He plus 1.01% hydrogen were used for the discharge and in absence of catalyst (no strontium in the discharge), as shown in Figure 12, the temperature of the outlet was 4.29 ºC higher than that of the inlet.

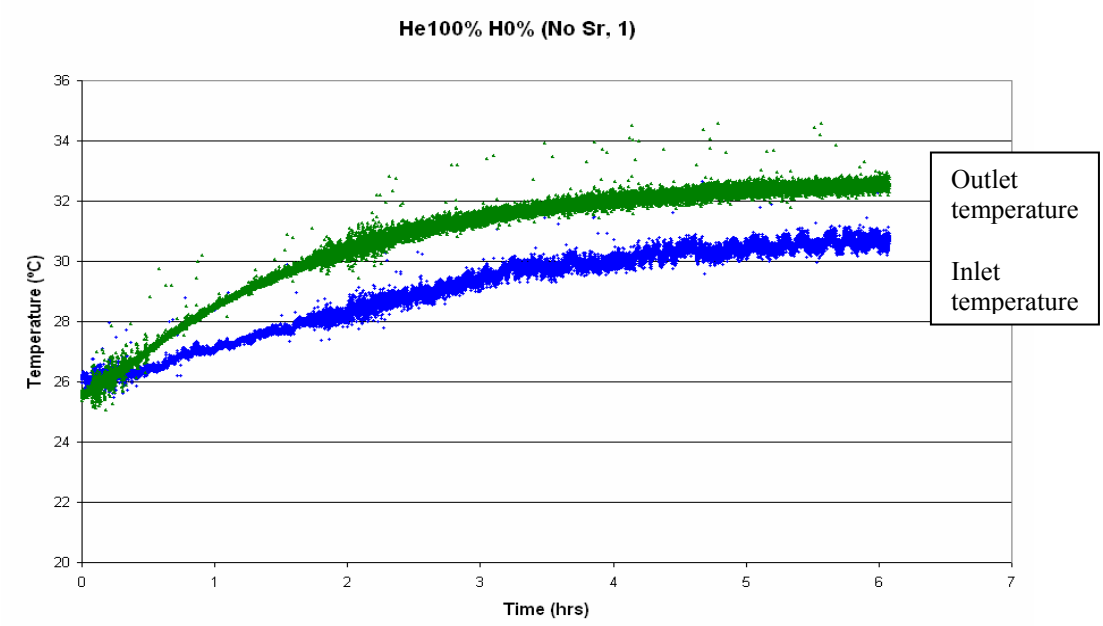

Figure 11 Gas temperature data for 100% He, no strontium in the test cell

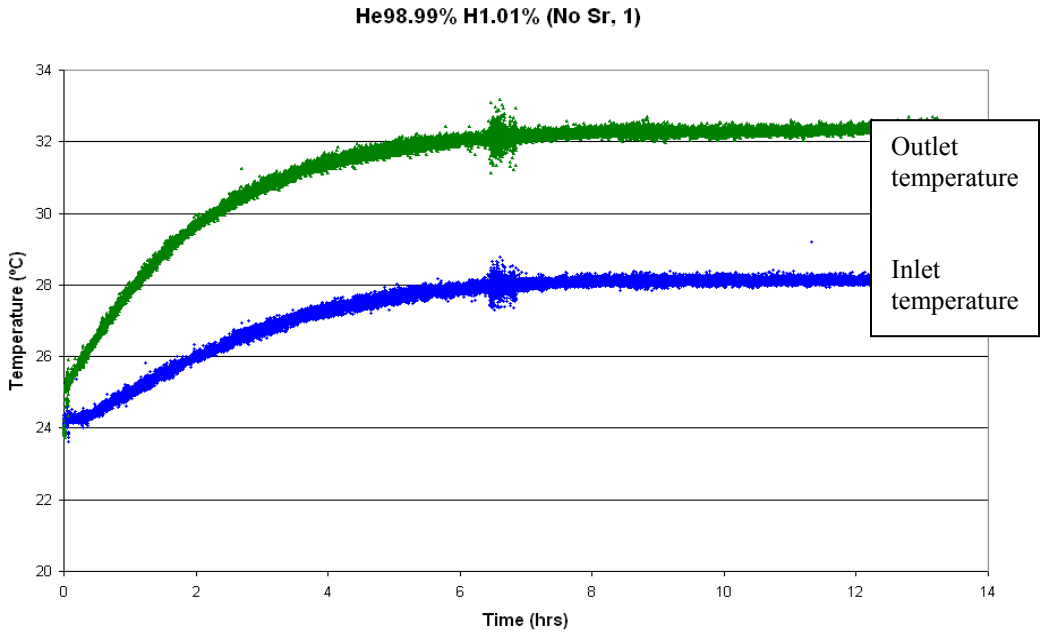

Figure 12 Gas temperature data for 98.99% He plus 1.01% hydrogen, no strontium in the test cell

Temperature difference is calculated from the measured inlet and outlet temperatures to determine the amount of temperature rise in each case, i.e. in each gas mixing combination, with and without strontium metal in the discharge. The temperature difference is used to evaluate the heat generation when compared to the electric power input to the discharge.

For a test in which 98.99% He plus 1.01% hydrogen were used for the discharge and in presence of catalyst (strontium in the discharge), as shown in Figure 13, the temperature of the outlet was 3.09 ºC higher than that of the inlet.

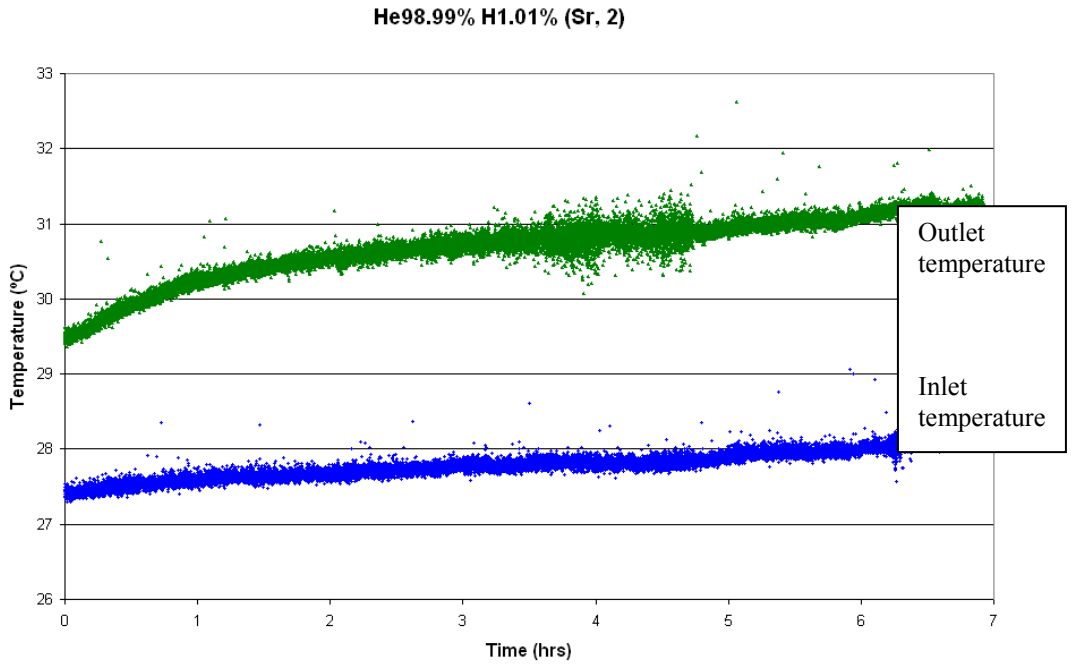

Figure 13 Gas temperature data for 98.99% He plus 1.01% hydrogen, with strontium in the test cell

For a test in which 95.14% He plus 4.86% hydrogen were used for the discharge and in presence of catalyst (strontium in the discharge), as shown in Figure 14, the temperature of the outlet was 3.7 ºC higher than that of the inlet.

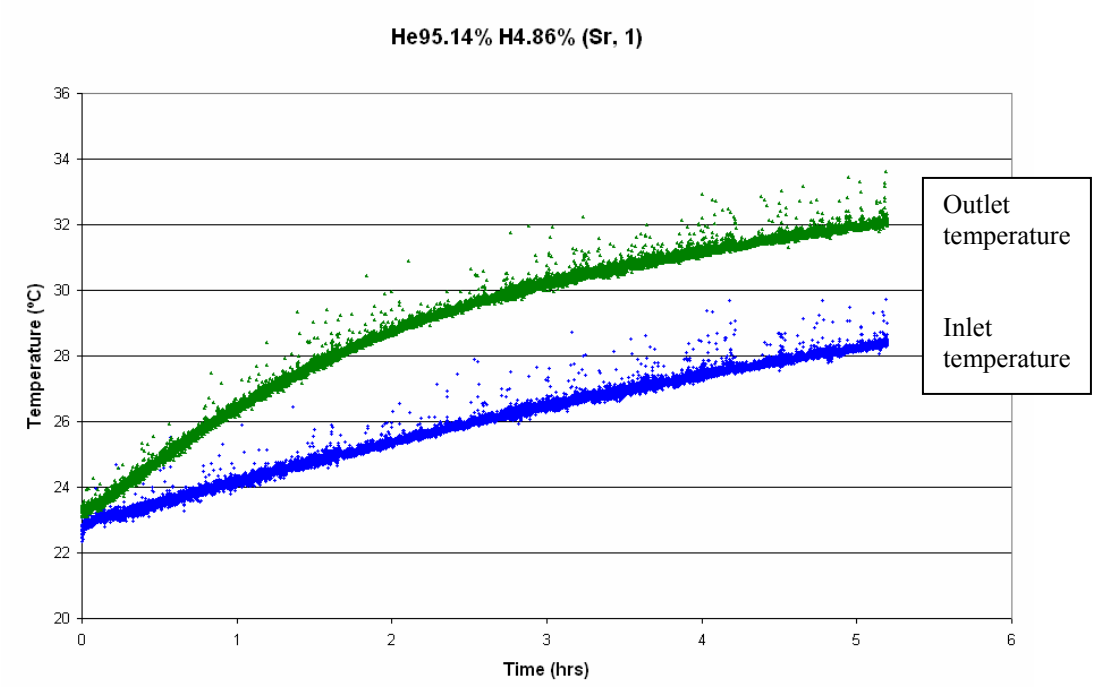

Figure 14 Gas temperature data for 95.14% He plus 4.86% hydrogen, with strontium in the test cell

Some of the thermal data were erroneous; however, all temperature data are shown in Appendices E and F, where not all the temperature data behaves so ideally. This is especially apparent in the second data set because the chamber was not allowed to reach thermal equilibrium with the surrounding environment. Temperature profiles similar to Figure 7 are considered smooth and ideal, for such temperature profiles the temperature difference was calculated by taking the difference of the average temperatures over regions of relative equilibrium. For profiles that not exactly idea, the difference was calculated by first taking the temperature difference at each point and taking the average of this difference. The approximate temperature differences are shown in the Table 3.

The temperature profiles in Data set 1 for pure helium and hydrogen at 1.01% produced erroneous data and hence they were not considered as representative measurements.

Table 3: Temperature Difference between inlet and outlet

	Temperature Difference (ºC)			
	Data Set 1		Data Set 2	
	No Sr	Sr	No Sr	Sr
H 0%	1.870	N/A	1.975	2.100
H 1.01%	4.290	N/A	2.320	3.085
H 2%	3.860	4.75	2.370	2.400
H 2.97%	2.705	4.30	2.375	2.290
H 3.92%	2.750	3.89	2.350	1.930
H 4.86%	2.890	3.70	2.410	2.120

Optical Emission Spectral Data

Two Ocean Optics HR2000 fixed grating spectrometers were used to obtain the spectra. Both spectrometers are fitted with a 600 line/mm grating, 25 μm slit and Ocean Optics L2 internal lens to focus the light onto the CCD. The grating of the UV-VIS spectrometer is blazed at 500 nm and views the wavelengths between 300 nm and 736 nm. The VIS-NIR spectrometer has a range of 600 nm to 1025 nm with the grating blazed at 750 nm. The spectrometers are power calibrated using an Ocean Optics LS-1-CAL lamp. Spectral data are transferred from the two spectrometers to a PC via IEEE interface card and an Ocean Optics software package. Collected spectral data will be analyzed using PeakFit spectra package to determine the emission, and/or absorption lines. The spectra taken were

analyzed in the region around the H_α line because this is the peak of interest for the energy of the hydrogen atoms.

When hydrogen is present in a discharge the broadening of the H_α line can be used to calculate the electron number density [7,33,34]. The FWHM of Stark broadening is given by: $w_s = 2.5\times10^{-10}\alpha_{n'n}\left(n_e, T_e\right)n_e^{3/2}$, where $\alpha_{n'n}$ is the reduced wavelength ($\Delta\lambda / E_o$) and n_e is the electron number density (cm^{-3}) and $\Delta\lambda = 2W\times n_e\times10^{-16} + 3.5A\left(n_e\times10^{-16}\right)^{1/4}$, where A is the ion-broadening parameter (may be neglected for non hydrogen plasmas) [7a,33a,34a]. Neglecting the 'A' factor as the hydrogen concentration is quite small, then $\Delta\lambda \cong 2W\times n_e\times10^{-16}$ and hence $n_e \cong \frac{\Delta\lambda}{2W}\times10^{16} / m^3$.

Figure 15 shows the spectra taken for the discharge with 98.99% He plus 1.01% hydrogen, with (blue) and without (red) strontium in the test cell. The figure focuses on the H_α line to determine any observable line broadening. It is not clear from this figure if any appreciable broadening took place, apparently due to the very low fraction of hydrogen flowing into the cell. However, there is a line shift of 0.18 nm when strontium is present in the discharge

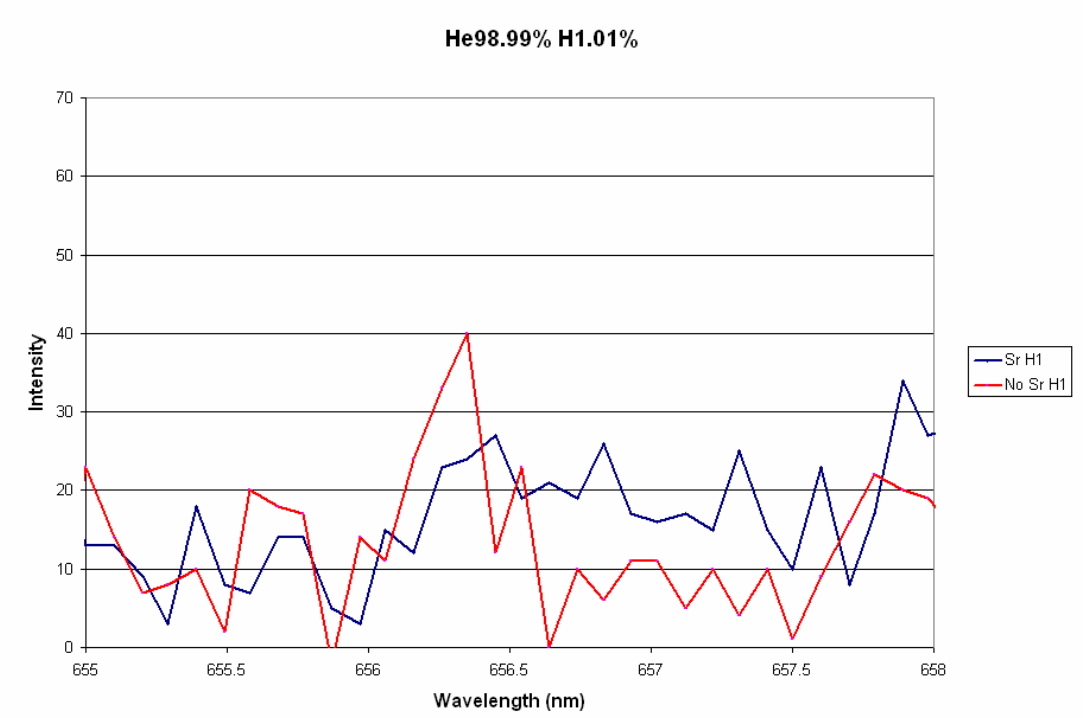

Figure 15 Optical emission spectral data for 98.99% He plus 1.01% hydrogen, with (blue) and without (red) strontium in the test cell

Figure 16 shows the spectra taken for the discharge with 96.08% He plus 3.92% hydrogen, with (blue) and without (red) strontium in the test cell. In this figure the H_α line is well defined for both cases (with and without strontium), almost at same line intensity. There is a slight broadening of the H_α line with the strontium in the discharge; however, it is not conclusive as an appreciable broadening.

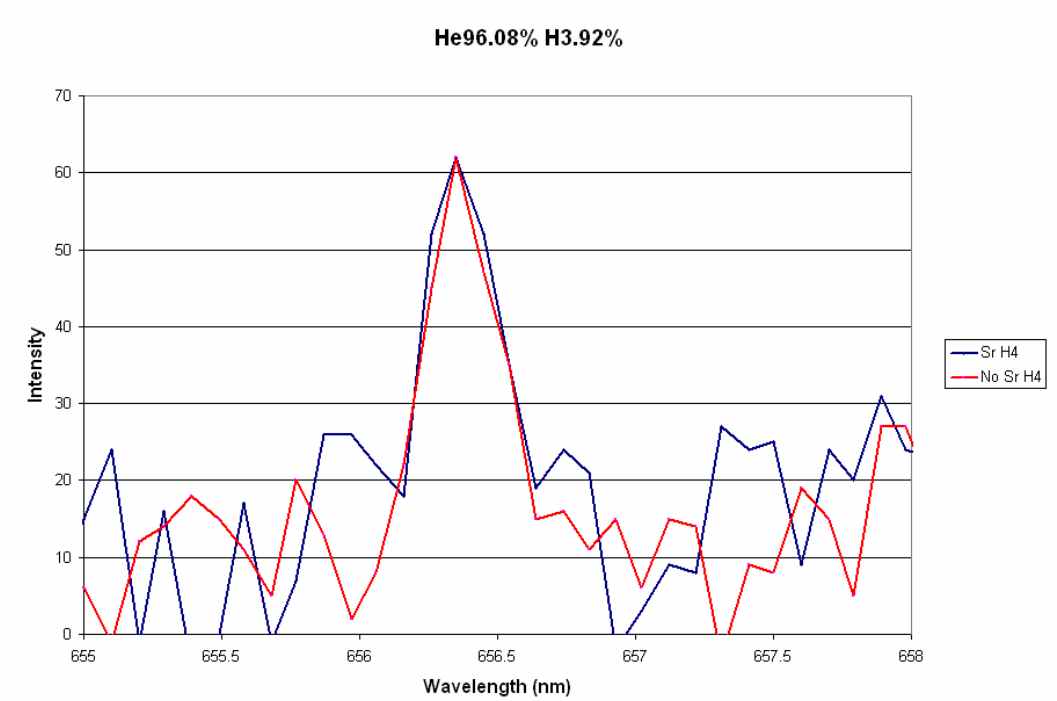

Figure 16 Optical emission spectral data for 96.08% He plus 3.92% hydrogen, with (blue) and without (red) strontium in the test cell

Figure 17 shows the spectra taken for the discharge with 95.14% He plus 4.86% hydrogen, with (blue) and without (red) strontium in the test cell. In this figure the H_α line is well defined for both cases (with and without strontium), and it is obvious that there is line broadening when strontium was present in the discharge.

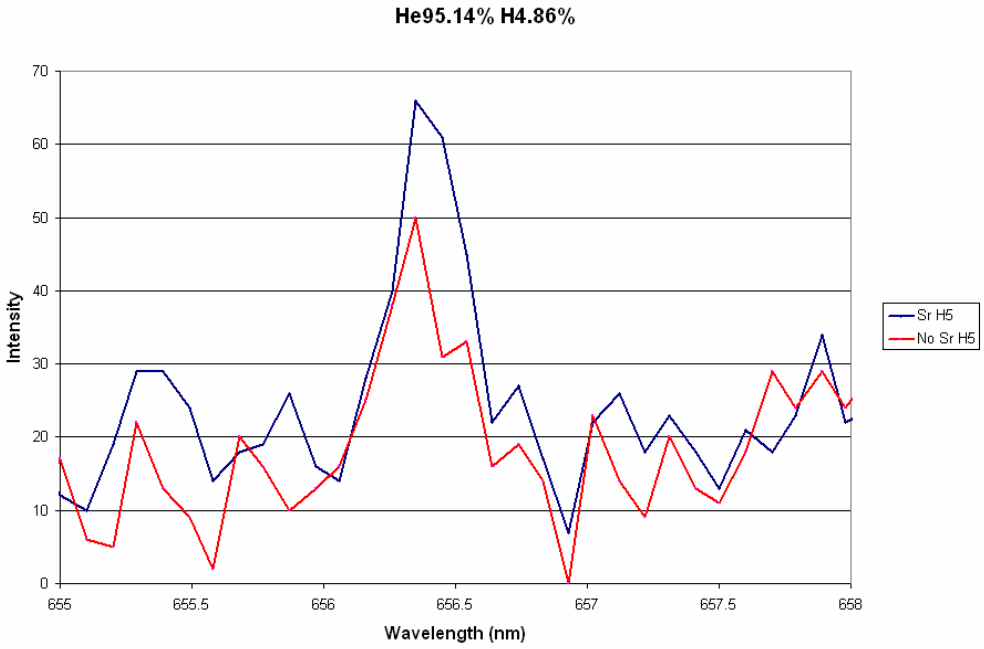

Figure 17 Optical emission spectral data for 95.14% He plus 4.86% hydrogen, with (blue) and without (red) strontium in the test cell

However, the line broadening shown in Fig. 17 when strontium is present in the discharge is not smooth, however, a 0.15 nm broadening is seen when strontium is introduced into the discharge.

Figure 18 shows the spectra taken for all experiments in presence of strontium in the discharge. The legend indicates the percent of hydrogen added to the helium in the cell. The numbers 0, 1, 2, 3, 4 and 5 are the mass flow rate of the hydrogen in sccm and correspond to 0, 1.01, 2.0, 2.97, 3.92 and 4.86% hydrogen, respectively. It is clear from the figure that the increase in the hydrogen percent increases the line intensity of the H_α line.

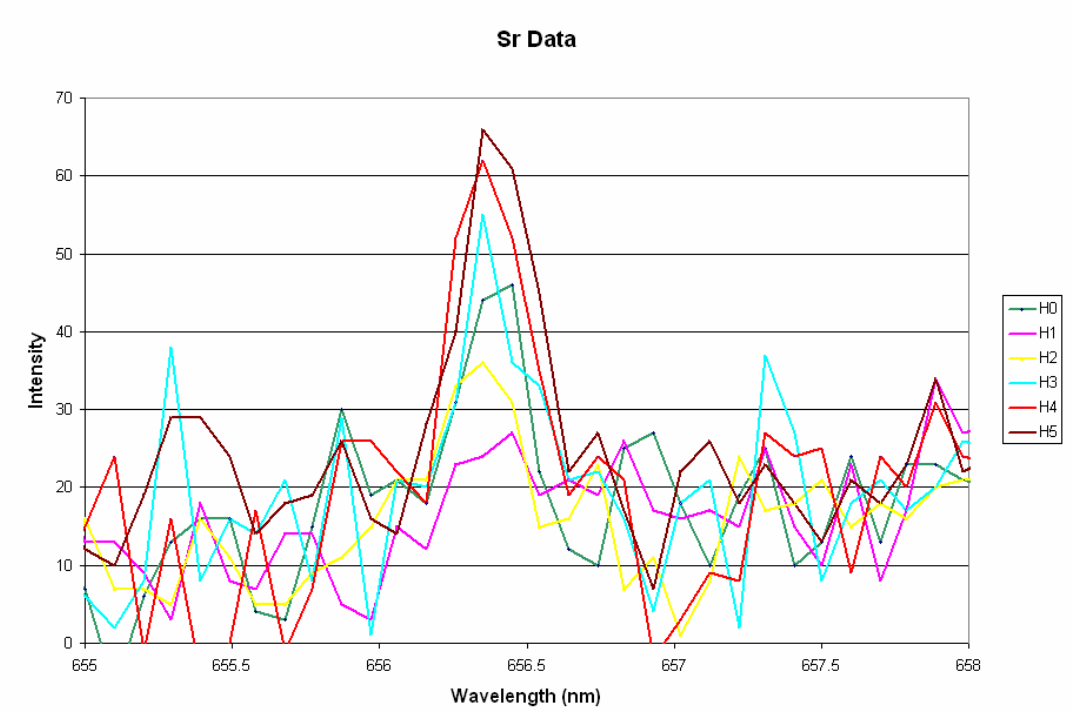

Figure 18 Optical emission spectral data for all experiments with strontium present in the test cell

Broadening data are not conclusive, however, if the 0.15 nm is taken into consideration and the FWHM of the H_α line is 0.5 nm, then the electron number density $n_e \cong \frac{\Delta\lambda}{2W} \times 10^{16} / m^3$ would be ~ 10^{15} m^{-3}. In most typical discharges, the electron number density varies between ~ 10^{13} to 10^{16} m^{-3} which is close to electron number density of ~ 10^{15} m^{-3} and hence the obtained electron number density is within expected range.

Plasma Model Results

The model described in chapter 4 was solved for each data set and the hydrogen concentration for the three separate cases. The first case assumed that the sheaths have no dimensions (inner and outer sheath thicknesses = 0), as if the sheath does not exist. The second case assumed that the outer sheath is at maximum thickness, as solved iteratively using Eq. 15 (Chapter 4), and that the inner sheath is at its minimum. The third case assumed that the inner sheath is at maximum thickness, again as solved with Eq. 15, and that the outer sheath is at its minimum. It will be shown that the solutions differ quantitatively, but they vary very little when the solutions are compared qualitatively. The electron-neutral collision frequencies were only slightly affected by the change in the sheath thicknesses. The three cases are shown below in Tables 4 and 5 with collision frequency for data sets 1 and 2, both with and without strontium present in the discharge.

Table 4: Collision frequency and electron number density; Data Set 1

Data Set 1: n_e and ν_{en}

		Electron number density (n_e)					
		Without Strontium			With Strontium		
H (%)	ν_{en}	Case 1	Case 2	Case 3	Case 1	Case 2	Case 3
0.00	3.726E+09						
1.01	3.805E+09	4.509E+15	4.502E+15	4.449E+15			
2.00	3.883E+09	4.691E+15	4.683E+15	4.625E+15	4.690E+15	4.681E+15	4.618E+15
2.97	3.970E+09	4.899E+15	4.890E+15	4.827E+15	4.903E+15	4.895E+15	4.834E+15
3.92	4.047E+09	5.097E+15	5.088E+15	5.029E+15	5.098E+15	5.089E+15	5.028E+15
4.86	4.124E+09	5.286E+15	5.276E+15	5.207E+15	5.290E+15	5.281E+15	5.214E+15

Table 5: Collision frequency and electron number density; Data Set 2

		Data Set 2: n_e and ν_{en}					
		Electron number density, n_e (m^{-3})					
		Without Strontium			With Strontium		
H (%)	ν_{en} (s^{-1})	Case 1	Case 2	Case 3	Case 1	Case 2	Case 3
0.00	3.726E+09	4.326E+15	4.319E+15	4.271E+15	4.323E+15	4.316E+15	4.263E+15
1.01	3.805E+09	4.512E+15	4.505E+15	4.455E+15	4.508E+15	4.501E+15	4.447E+15
2.00	3.883E+09	4.693E+15	4.685E+15	4.629E+15	4.693E+15	4.685E+15	4.630E+15
2.97	3.970E+09	4.907E+15	4.899E+15	4.845E+15	4.899E+15	4.890E+15	4.827E+15
3.92	4.047E+09	5.110E+15	5.103E+15	5.058E+15	5.094E+15	5.085E+15	5.022E+15
4.86	4.124E+09	5.299E+15	5.291E+15	5.238E+15	5.289E+15	5.280E+15	5.216E+15

From these tables, it is clear that the electron number density is in the range of $10^{15}/m^3$. Figure 19 shows the comparison for all three cases for data set 2 without strontium. It can be seen that although the solutions are not the same for the three cases, they are close and they follow the same pattern.

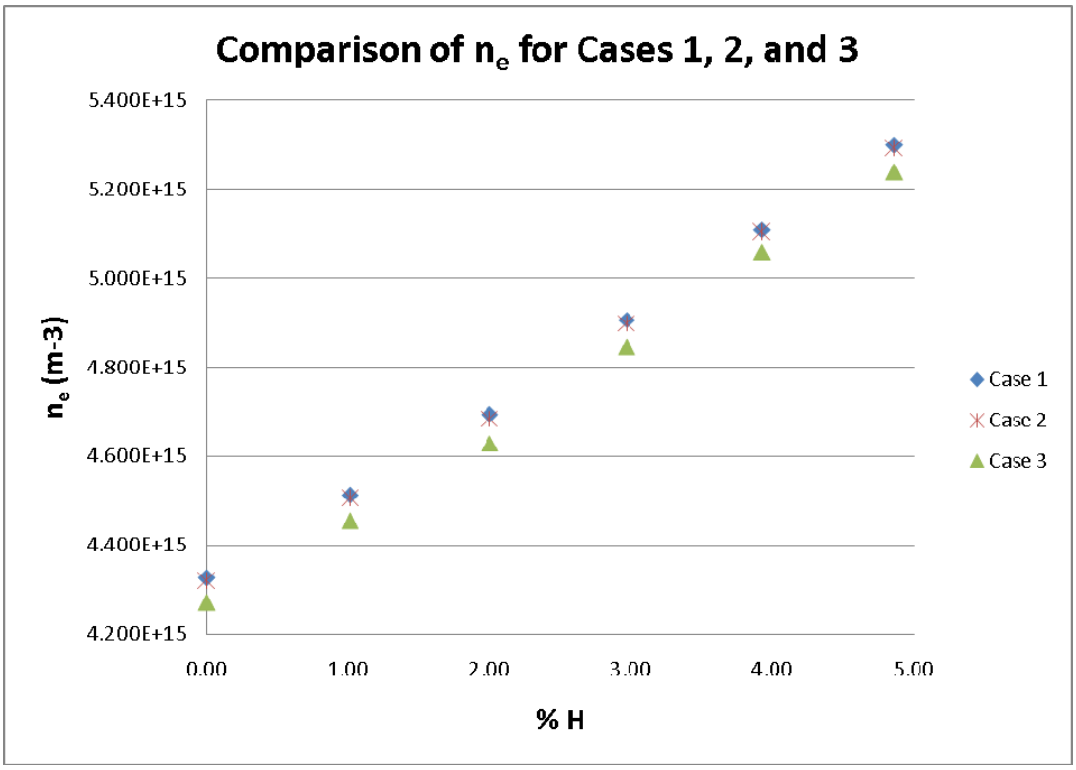

Figure 19 Comparison of calculated electron number density for Cases 1 (no sheaths), 2 (outer sheath at maximum thickness), and 3 (inner sheath at maximum thickness)

The Joule heating was determined using the electron neutral collision frequency and electron number density from the model using Eq. 18, and was calculated for cases 1 (no sheaths), 2 (outer sheath at maximum thickness), and 3 (inner sheath at maximum thickness) assuming that the sheath provides 85 – 95% of the voltage drop across the discharge (typical of sheath behavior). This means that 5 – 15% of the voltage drop is across the plasma itself. The following tables show the thermal output obtained from experimental temperature measurements using Eq. 19 and the calculated Joule heating for both data sets with and without strontium for all three cases at the upper and lower limits of voltage drop across the plasma bulk. The ratio between the thermal output and Joule heating input gives some

insight into the effect of strontium and hydrogen additions to the discharge. Table 6 displays the thermal output and Joule heating input for Data Set 1 without strontium for the voltage drop of 15% and 5% across the plasma bulk, while Table 7 displays the thermal output and Joule heating input for the same data set with strontium in the discharge.

Table 6: Thermal output and Joule heating input; Data Set 1 without strontium

Data Set 1 without Strontium

H (%)	$P_{thermal}$	$P_{Joule\ Heating}$ (W)					
		Case 1		Case 2		Case 3	
		15%	5%	15%	5%	15%	5%
0							
1.01	0.00728	1050.98	116.78	1049.23	116.58	1036.94	115.22
2	0.00664	1083.79	120.42	1081.88	120.21	1068.41	118.71
2.97	0.00472	1092.02	121.34	1090.00	121.11	1075.83	119.54
3.92	0.00486	1099.86	122.21	1098.02	122.00	1085.12	120.57
4.86	0.00518	1141.72	126.86	1139.59	126.62	1124.72	124.97

Table 7: Thermal output and Joule heating input; Data Set 1 with strontium

Data Set 1 with Strontium

H (%)	$P_{thermal}$	$P_{Joule\ Heating}$ (W)					
		Case 1		Case 2		Case 3	
		15%	5%	15%	5%	15%	5%
0							
1.01							
2	0.00818	1211.74	134.638	1209.44	134.382	1193.17	132.575
2.97	0.00750	1208.64	134.293	1206.51	134.056	1191.51	132.39
3.92	0.00688	1273.5	141.5	1271.31	141.257	1255.89	139.543
4.86	0.00663	1277.18	141.909	1274.9	141.656	1258.87	139.874

Table 8 displays the thermal output and Joule heating input for Data Set 2 without strontium for the voltage drop of 15% and 5% across the plasma bulk, while Table 9 displays the thermal output and Joule heating input for the same data set with strontium in the discharge.

Table 8: Thermal output and Joule heating input; Data Set 2 without strontium

Data Set 2 without Strontium

H (%)	$P_{thermal}$	$P_{Joule\ Heating}$ (W)					
		Case 1		Case 2		Case 3	
		15%	5%	15%	5%	15%	5%
0	0.0033	1024.26	113.81	1022.65	113.63	1011.28	112.36
1.01	0.00394	1067.38	118.60	1065.71	118.41	1053.99	117.11
2	0.00408	1062.85	118.09	1061.06	117.90	1048.45	116.49
2.97	0.00414	1101.13	122.35	1099.39	122.15	1087.22	120.80
3.92	0.00416	1127.12	125.24	1125.71	125.08	1115.84	123.98
4.86	0.00432	1159.61	128.85	1157.95	128.66	1146.30	127.37

Table 9: Thermal output and Joule heating input; Data Set 2 with strontium

Data Set 2 with Strontium

H (%)	$P_{thermal}$	$P_{Joule\ Heating}$ (W)					
		Case 1		Case 2		Case 3	
		15%	5%	15%	5%	15%	5%
0	0.00351	1054.54	117.17	1052.71	116.97	1039.78	115.53
1.01	0.00524	1046.50	116.28	1044.73	116.08	1032.25	114.69
2	0.00413	1064.00	118.22	1062.22	118.02	1049.66	116.63
2.97	0.0037	1079.00	119.89	1077.01	119.67	1063.01	118.11
3.92	0.00341	1129.41	125.49	1127.40	125.27	1113.28	123.70
4.86	0.0038	1144.74	127.19	1142.75	126.97	1128.79	125.42

The following tables show the thermal output of the gases per Joule heating input into the plasma. These numbers are important for normalizing the thermal output in order to make more accurate comparisons.

Table 10 displays the thermal output per Joule heating input for Data Set 1 without strontium for the voltage drop of 15% and 5% across the plasma bulk, while Table 11 displays the thermal output per Joule heating input for the same data set with strontium in the discharge.

Table 10: Thermal output per Joule heating input; Data Set 1 without strontium

Data Set 1 without Strontium

$P_{thermal} / P_{Joule\ Heating}$

H (%)	Case 1		Case 2		Case 3	
	15%	5%	15%	5%	15%	5%
0						
1.01	6.93E-06	6.24E-05	6.94E-06	6.25E-05	7.02E-06	6.32E-05
2	6.13E-06	5.52E-05	6.14E-06	5.53E-05	6.22E-06	5.60E-05
2.97	4.32E-06	3.89E-05	4.33E-06	3.90E-05	4.39E-06	3.95E-05
3.92	4.42E-06	3.98E-05	4.43E-06	3.99E-05	4.48E-06	4.03E-05
4.86	4.54E-06	4.08E-05	4.55E-06	4.09E-05	4.61E-06	4.15E-05

Table 11: Thermal output per Joule heating input; Data Set 1 with strontium

Data Set 1 with Strontium

$P_{thermal} / P_{Joule\ Heating}$

H (%)	Case 1		Case 2		Case 3	
	15%	5%	15%	5%	15%	5%
0						
1.01						
2	6.75E-06	6.07E-05	6.76E-06	6.08E-05	6.85E-06	6.17E-05
2.97	6.21E-06	5.59E-05	6.22E-06	5.60E-05	6.30E-06	5.67E-05
3.92	5.40E-06	4.86E-05	5.41E-06	4.87E-05	5.48E-06	4.93E-05
4.86	5.19E-06	4.67E-05	5.20E-06	4.68E-05	5.27E-06	4.74E-05

Table 12 displays the thermal output and Joule heating input for Data Set 2 without strontium for the voltage drop of 15% and 5% across the plasma bulk, while Table 13 displays the thermal output per Joule heating input for the same data set with strontium in the discharge.

Table 12: Thermal output per Joule heating input; Data Set 2 without strontium

Data Set 2 without Strontium

$P_{thermal} / P_{Joule\ Heating}$

H (%)	Case 1		Case 2		Case 3	
	15%	5%	15%	5%	15%	5%
0	3.23E-06	2.90E-05	3.23E-06	2.91E-05	3.27E-06	2.94E-05
1.01	3.69E-06	3.32E-05	3.69E-06	3.33E-05	3.74E-06	3.36E-05
2	3.84E-06	3.45E-05	3.84E-06	3.46E-05	3.89E-06	3.50E-05
2.97	3.76E-06	3.39E-05	3.77E-06	3.39E-05	3.81E-06	3.43E-05
3.92	3.69E-06	3.32E-05	3.69E-06	3.32E-05	3.73E-06	3.35E-05
4.86	3.73E-06	3.35E-05	3.73E-06	3.36E-05	3.77E-06	3.39E-05

Table 13: Thermal output per Joule heating input; Data Set 2 with strontium

Data Set 2 with Strontium

$P_{thermal} / P_{Joule\ Heating}$

H (%)	Case 1		Case 2		Case 3	
	15%	5%	15%	5%	15%	5%
0	3.33E-06	3.00E-05	3.34E-06	3.00E-05	3.38E-06	3.04E-05
1.01	5.00E-06	4.50E-05	5.01E-06	4.51E-05	5.07E-06	4.57E-05
2	3.88E-06	3.49E-05	3.89E-06	3.50E-05	3.94E-06	3.54E-05
2.97	3.43E-06	3.09E-05	3.43E-06	3.09E-05	3.48E-06	3.13E-05
3.92	3.02E-06	2.72E-05	3.03E-06	2.73E-05	3.07E-06	2.76E-05
4.86	3.32E-06	2.99E-05	3.33E-06	2.99E-05	3.37E-06	3.03E-05

In general, there is a slight increases in the thermal output per joule heating, however, it is difficult to conclude excess heat generation. At both the upper (15%) and lower (5%) bounds of percentage voltage drop across the bulk plasma, the behavior of the normalized thermal output remains the same as shown in Figure 20.

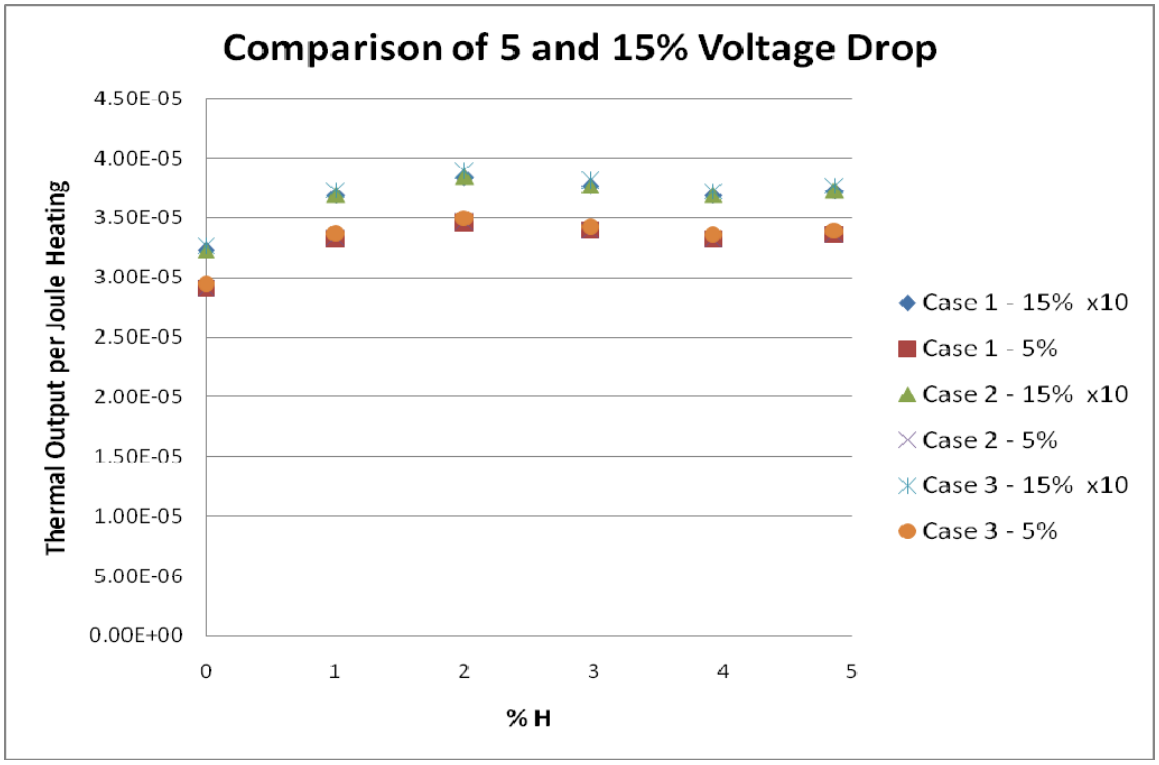

Figure 20 Comparison of the upper and lower bounds of 5 and 15% voltage drop across the bulk plasma for data set 2 without strontium for cases 1, 2, and 3

It is clear from the figure that the qualitative behavior of the normalized thermal output does not change with respect to the percent voltage drop across the plasma sheath. For the purposes of qualitative comparison, the case of 5% voltage drop will be examined.

It is also difficult to tell from the thermal output per Joule heating input, as shown in Tables 10 through 13, that there is significant heat generation. Figure 21 displays the thermal

output per Joule heating input and it is obvious that the normalized thermal output remains constant for all three cases, i.e. does not change with the change in sheath thickness.

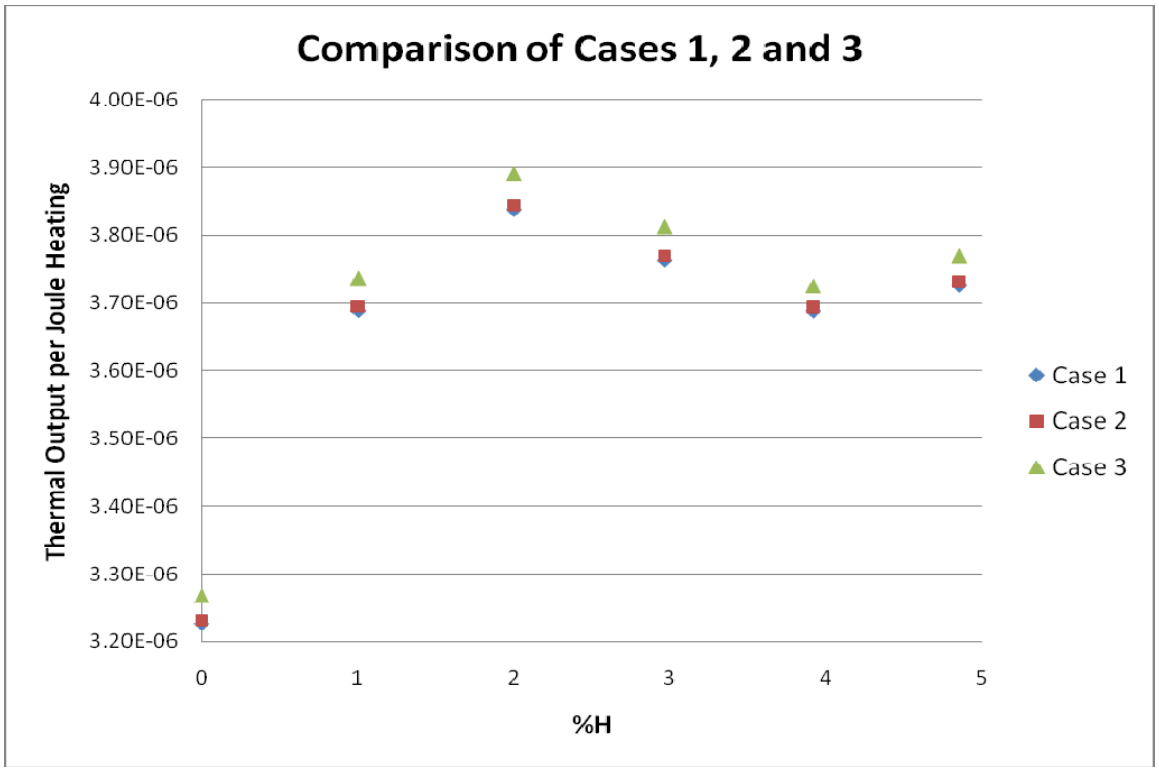

Figure 21 Comparison of cases 1, 2, and 3 for data set 2 without strontium for a 5% voltage drop across the bulk plasma

As the normalized thermal output does not change with respect to sheath thickness assumptions, case 1 (no sheath thickness) and case 3 (maximum inner sheath thickness) will not be considered in the qualitative analysis; case 2 (maximum outer sheath thickness) with 5% voltage drop across the plasma bulk, with and without strontium, will be the focus of qualitative comparison as a representative case.

Figure 22 shows a comparison of the normalized thermal output (thermal output per Joule heating input) for both data sets with and without strontium present for hydrogen

concentrations of 0, 1.01, 2, 2.97, 3.92, and 4.86% with helium comprising the rest of the gas.

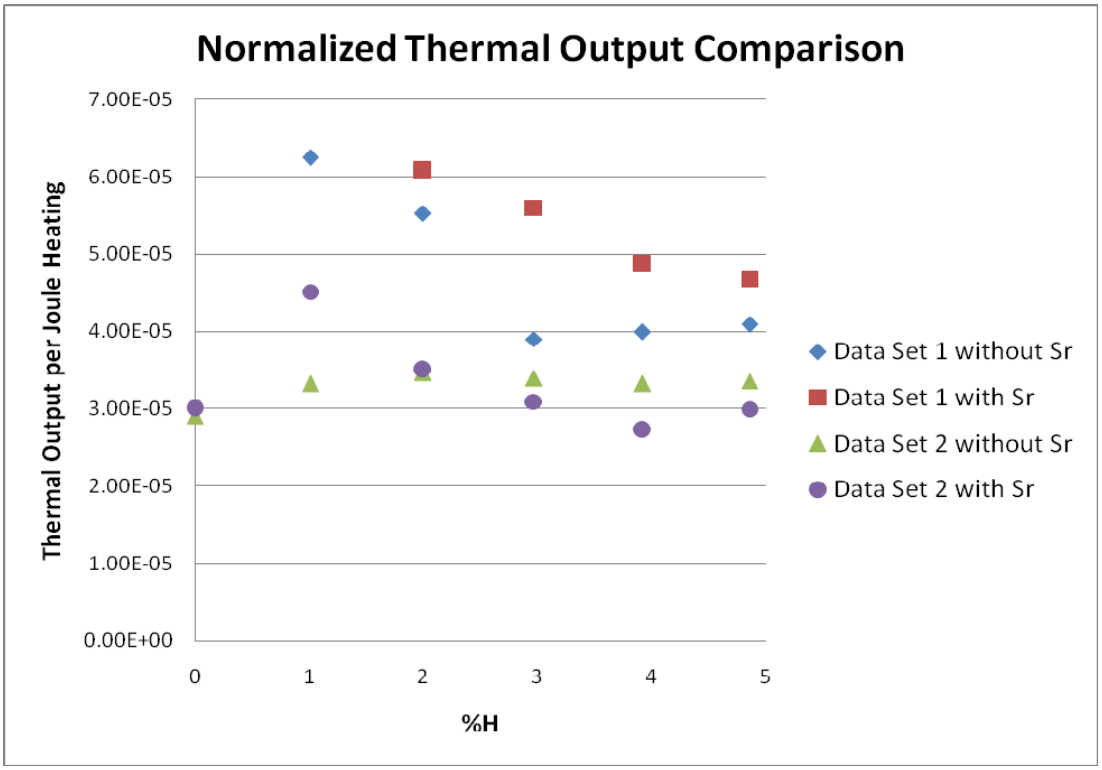

Figure 22 Comparison of normalized thermal output for data sets 1 and 2 both with and without strontium present for 0, 1.01, 2, 2.97, 3.92, 4.86% hydrogen with the remainder of the gas helium

As seen from Fig. 22, data set 1 shows an increase in the thermal output per Joule heating input when strontium is present in the discharge; however, it is not the case for data set 2 where there is no appreciable change except for the case of 1.01% hydrogen. These data are also shown forming Table 14.

Data set 1 shows a marked increase in thermal output in the presence of strontium for hydrogen concentrations at 2, 2.97, 3.92, and 4.86% as can be seen in Figure 22 and Table 14. Data set 2 showed less promising results for hydrogen concentrations of 2, 2.97, 3.92, and 4.86%. Without strontium present in the discharge, the thermal output increases slightly with the addition of 1.01% hydrogen and then remains relatively constant as more hydrogen is added. This indicates that a saturation point was reached at which there is little effect from the addition of more hydrogen.

Table 14: Normalized thermal output for data sets 1 and 2 both with and without strontium present

	Normalized Thermal Output			
	Data Set 1		***Data Set 2***	
H (%)	Without Sr	With Sr	Without Sr	With Sr
0			2.91E-05	3.00E-05
1.01	6.25E-05		3.33E-05	4.51E-05
2	5.53E-05	6.08E-05	3.46E-05	3.50E-05
2.97	3.90E-05	5.60E-05	3.39E-05	3.09E-05
3.92	3.99E-05	4.87E-05	3.32E-05	2.73E-05
4.86	4.09E-05	4.68E-05	3.36E-05	2.99E-05

Chapter 6

Conclusions

This novel method of energy production may represent the future of energy, but much more study is required. Past work has shown promise in energy production possibilities with catalysis of the hydrino process [8,9]. The work done here is intended to expand the breadth of study in this field to include audio frequency plasma discharges to the current work, which consists mainly of RF discharges at low frequencies in the kHz range; which was not conducted at such frequencies in previous work. The normalized thermal output of plasma discharges at audio frequency in the presence of helium and strontium, as catalysts, is an important step in furthering the knowledge of this catalysis. These normalized thermal outputs have been compared with each other in order to determine the best candidate for future work in this field.

The developed plasma model was effective in providing an estimate of the electron number density and it is shown that the number density is within the expected range of $10^{15}/m^3$, which is also the same range for the density obtained from optical emission spectroscopy. The plasma model provided estimates of electron temperature, electron-neutral collision frequency, and electron number density. The model parameters needed to calculate the Joule heating of the plasma were also obtained. The Joule heating to the discharge is important in normalizing the measured thermal output to quantify any excess heat generation from the discharge when strontium is added as a catalyst.

Data set 1 shows a marked increase in thermal output in the presence of strontium for hydrogen concentrations at 2, 2.97, 3.92, and 4.86%. There is no data for data set 1 with strontium for pure helium and 1.01% hydrogen because of anomalous temperature readings that were discarded. This is also the case for data set 1 without strontium for a pure helium discharge.

Data set 2 showed less promising results for hydrogen concentrations of 2, 2.97, 3.92, and 4.86%. Without strontium present, the thermal output increases slightly with the addition of 1.01% hydrogen and then remains relatively constant as more hydrogen is added. This indicates that a saturation point was reached at which there is little effect from the addition of more hydrogen. In the presence of strontium, the thermal output for hydrogen concentrations of 2, 2.97, 3.92, and 4.86% hovers around the same thermal output that was seen for the pure helium discharge. However, in the presence of strontium with a hydrogen concentration of 1.01%, there is a marked increase in thermal output. Again, a hydrogen concentration of 1.01% appears to be a candidate for future work.

Future Work

Conduct careful calorimetric measurements in fully insulated environment to ensure correct calculations of the thermal energy output. Changes in ambient room temperature may produce a source of error. This may be conducted in a fully insulated experiment in which thermal radiation losses are eliminated. Temperature measurements could be affected and may lead to erroneous data; adding infra red thermocouples would improve assessing thermal leakage from the system.

The effect of chemical reactions between strontium and hydrogen needs to be examined to determine if exothermal reactions are taking place during the experiment.

Employ other diagnostic techniques, such as electric probes, to determine the thickness of the sheath.

Expand the plasma model to incorporate inductive effects on the equivalent circuit elements of the discharge.

Employ a LabView interface to control the experiment, such as gas flow rates, operating voltage and current, frequency, ambient temperature, and chamber pressure; and incorporate the model mathematical solvers into the LabView to automatically display the plasma parameters in real time during the experiment.

References

[1] U.S. Bureau of Oceans and International Environmental and Scientific Affairs (2007). Fourth U.S. Climate Action Report to the UN Framework Convention on Climate Change. Wachington, D.C., 124 pp.

[2] IPCC (2007). Climate Change 2007: Synthesis Report. Contribution of Working Groups I, II and III to the Fourth Assessment Report of the Intergovernmental Panel on Climate Change [Core Writing Team, Pachauri, R.K and Reisinger, A. (eds.)]. IPCC, Geneva, Switzerland, 104 pp.

[3] Dresselhaus, M. S., & Thomas, I. L. (2001). Alternative energy technologies. *Nature, 414*, 332-337.

[4] Sims, R.E.H., Rogner, H.H., & Gregory, K. (2003). Carbon emission and mitigation cost comparisons between fossil fuel, nuclear, and renewable energy resources for electricity generation. *Energy Policy, 31*(13), 1315-1326.

[5] Mills, R. L. (2008). *The grand unified theory of classical physics.* Retrieved from http://www.blacklightpower.com/theory/book.shtml

[6] Griffiths, D. J. (1999). *Introduction to electrodynamics*. Upper Saddle River, New Jersey: Prentice Hall.

[7] Griem, H. R. (1997). *Principles of plasma spectroscopy*. New York: Cambridge University Press.

[8] Mills, R. L., He, J., Nansteel, M., & Dhandapani, B. (2007). Catalysis of atomic hydrogen to new hydrides as a new power source. *International Journal of Global Energy Issues, 28*(2/3), 304-324.

[9] Mills, R.L., Chen, X., Ray, P., He, J., & Dhandapani, B. (2003). Plasma power source based on catalytic reaction of atomic hydrogen measured by water bath calorimetry, *Thermochimica Acta,* 406(1-2), 35-36.

[10] Mills, R. L., Zea, H., He, J., Dhandapani, B. (2007). Water bath calorimetry on a catalytic reaction of atomic hydrogen. *International Journal of Hydrogen Energy, 32*(17), 4258-4266.

[11] Phillips, J., Mills, R., Chen, X. (2004). Water bath calorimetric study of excess heat generation in "resonant transfer" plasmas. *Journal of Applied Physics, 96*(6), 3095-3102.

[12] Mills, R., & Ray, P. (2003). Extreme ultraviolet spectroscopy of helium-hydrogen plasma. *Journal of Physics D: Applied Physics*, *36*(13), 1535-1542.

[13] Mills, R. L., Ray, P., Dhandapani, B., Nansteel, M., Chen, X., He, J. (2002). New power source from fractional quantum energy levels of atomic hydrogen that surpasses internal combustion. *Journal of Molecular Structure, 643*(1-3), 43-54.

[14] Mills, R. L., He, J., Chang, Z., Good, W., Lu, Y., Dhandapani, B. (2007). Catalysis of atomic hydrogen to novel hydrogen species H-(1/4) and H2(1/4) as a new power source. *International Journal of Hydrogen Energy, 32*(13), 2573-2584.

[15] Mills, R. L., Ray, P., Dhandapani, B. (2006). Evidence of an energy transfer reaction between atomic hydrogen and argon II or helium II as the source of excessively hot H atoms in radio-frequency plasmas. *Journal of Plasma Physics, 72*(4), 469-484.

[16] Mills, R. L., Ray, P. C., Nansteel, M., Chen, X., Mayo, R. M., & He, J., et al. (2003). Comparison of excessive balmer α line broadening of inductively and capacitively coupled RF, microwave, and glow-discharge hydrogen plasmas with certain catalysts. *IEEE Transactions on Plasma Science*, *31*(3), 338-355.

[17] Mills, R. L., Nansteel, M., & Ray, P. C. (2002). Argon-hydrogen-strontium discharge light source. *IEEE Transactions on Plasma Science*, *30*(2), 639-652.

[18] Conrads, H., Mills, R., & Wrubel, T. (2003). Emission in the deep vacuum ultraviolet from a plasma formed by incandescently heating hydrogen gas with trace amounts of potassium carbonate. *Plasma Sources Science and Technology*, *12*(3), 389-395.

[19] Mills, R. L., Nansteel, M., & Ray, P. C. (2002). Bright hydrogen-light source due to a resonant energy transfer with strontium and argon ions. *New Journal of Physics*, *4*, 70.1-70.28.

[20] Phillips, J., Chen, C. K., Akhtar, K., Dhandapani, B., Mills, R. (2007). Evidence of catalytic production of hot hydrogen in rf generated hydrogen/argon plasmas. *International Journal of Hydrogen Energy, 32*(14), 3010-3025.

[21] Mills, R. L., Ray, P., & Dhandapani, B. (2008). Excessive Balmer α line broadening of water-vapor capacitively-coupled rf discharge plasmas. *International Journal of Hydrogen Energy, 33*(2), 802-815.

[22] Fridman, A. A., & Kennedy, L. A. (2004). *Plasma physics and engineering.* New York: Taylor and Francis.

[23] Jackson, J. D. (1999). *Classical electrodynamics*. New York: Wiley.

[24] Hutchinson, I. H. (2002). *Principles of plasma diagnostics*. New York: Cambridge University Press.

[25] Lochte-Holtgreven, W. (1995). *Plasma diagnostics*. New York: AIP Press.

[26] Lieberman, M. A., & Lichtenberg, A. J. (1994). *Principles of plasma discharges and materials processing.* New York: Wiley.

[27] Griem, H. R., & Lovberg, R. H. (Eds.). (1970-71). *Plasma physics*. New York: Academic Press.

[28] Cairns, R. A. (1985). *Plasma physics*. Philadelphia: Heyden.

[29] Jones, R. K. (1985). Absolute total cross section for electron scattering from molecular hydrogen from 1 to 50 eV. *Physical Review A, 31*(5), 2898-2904.

[30] Nickel, J. C., Imre, K., Register, D. F., & Trajmar, S. (1985). Total electron scattering cross sections: I. He, Ne, Ar, Xe. *Journal of Physics B: Atomic, Molecular and Optical Physics, 18*, 125-133.

[31] Kennerly, R. E., & Bonham, R. A. (1978). Electron-helium absolute total scattering cross sections from 0.5 to 50 eV. *Physical Review A, 17*(6), 1844-1854.

[32] Chen, F. F. (1984). *Introduction to plasma physics and controlled fusion.* New York: Plenum Press.

[33] Griem, H. R. (1974). *Spectral line broadening by plasmas*. New York: Academic Press.

[34] Auciello, O., & Flamm, D. L. (Eds.). (1989). *Plasma diagnostics*. Boston: Academic Press.

Appendices

Appendix A: Data Set 1; Voltage and Current Waveforms

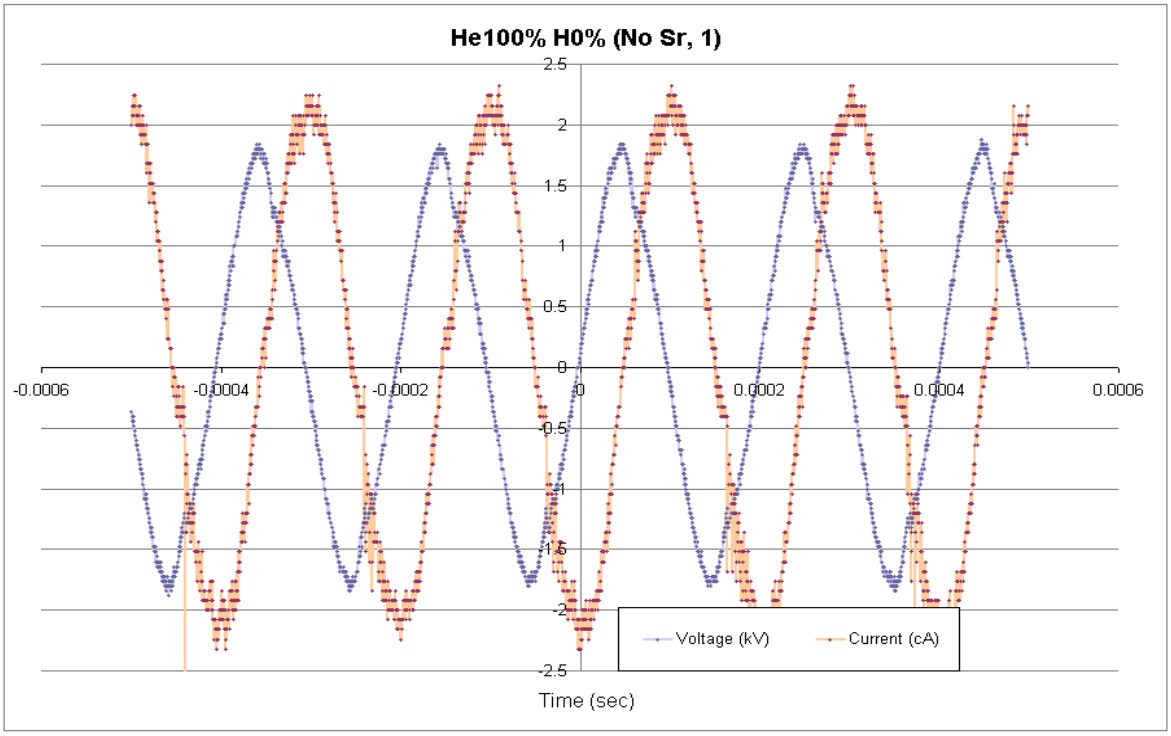

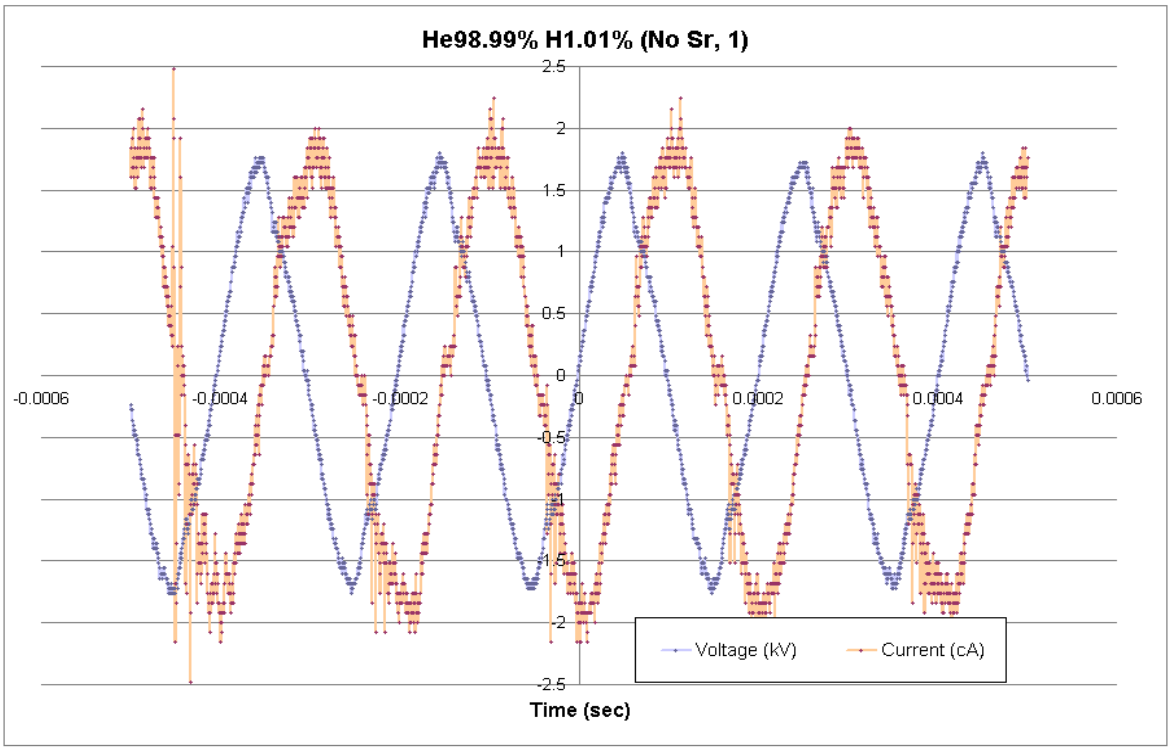

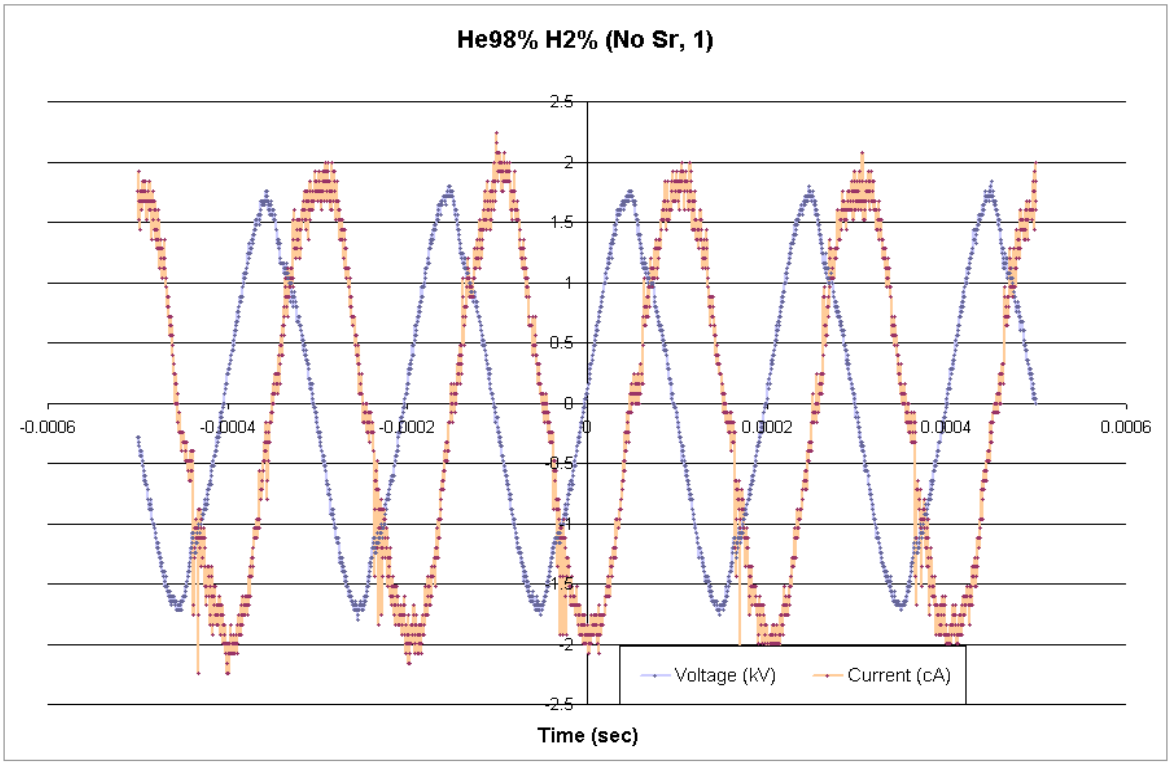
He98% H2% (No Sr, 1)
2.5
2
1.5
1
0.5
0
-0.0006
-0.0004
-0.0002
0
0.0002
0.0004
0.0006
-0.5
-1
-1.5
-2
-2.5
Voltage (kV)
Current (cA)
Time (sec)

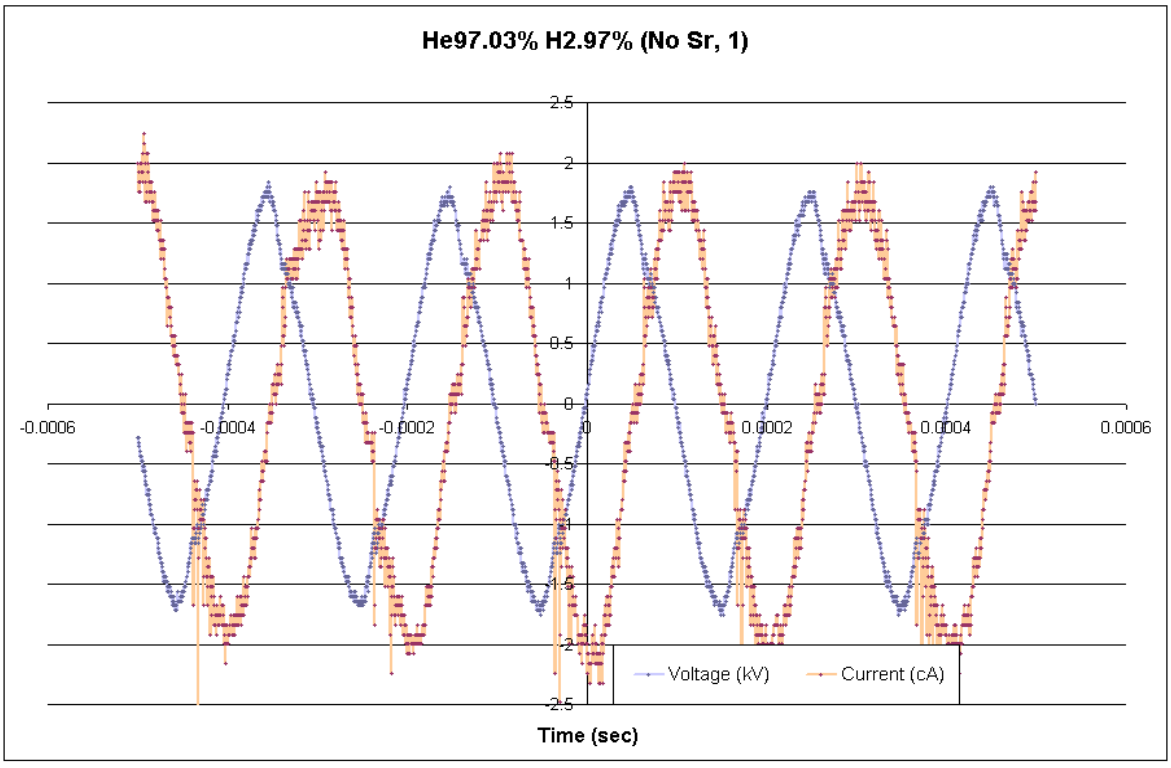
He97.03% H2.97% (No Sr, 1)
2.5
2
1.5
1
0.5
0
-0.0006
-0.0004
-0.0002
0
0.0002
0.0004
0.0006
-0.5
-1
-1.5
-2
-2.5
Voltage (kV)
Current (cA)
Time (sec)

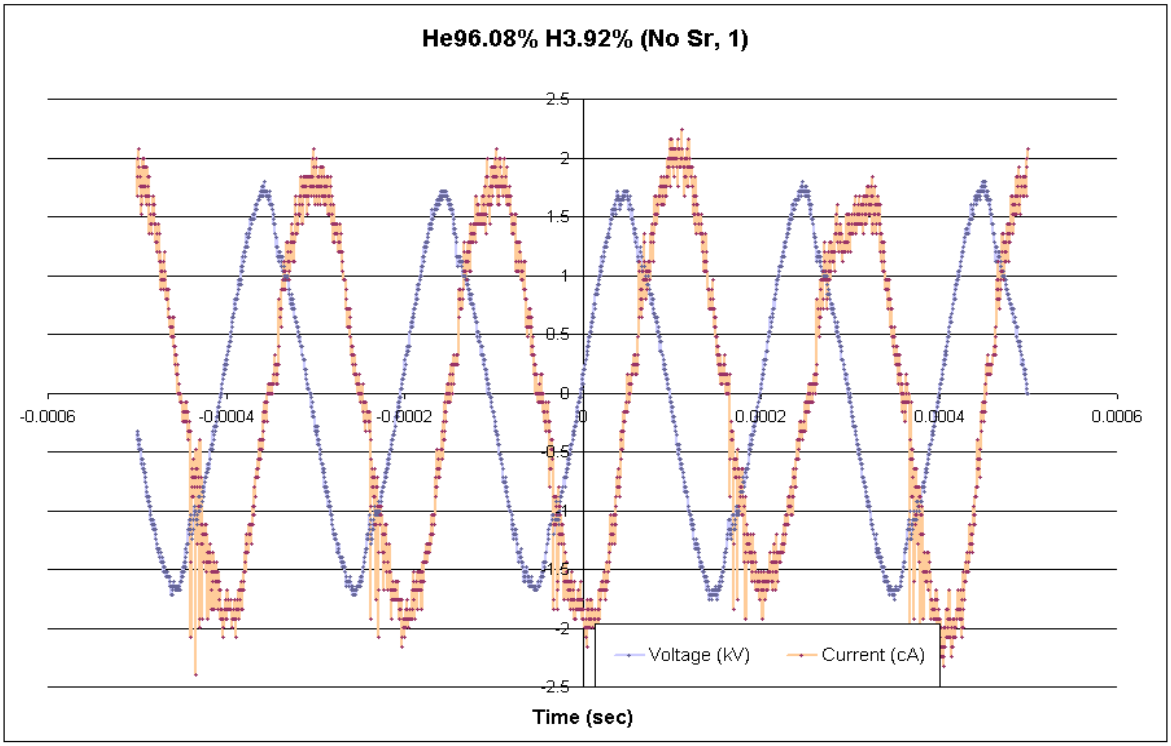
He96.08% H3.92% (No Sr, 1)
2.5
2
1.5
1
0.5
0
-0.5
-1
-1.5
-2
-2.5
-0.0006
-0.0004
-0.0002
0
0.0002
0.0004
0.0006
Voltage (kV)
Current (cA)
Time (sec)

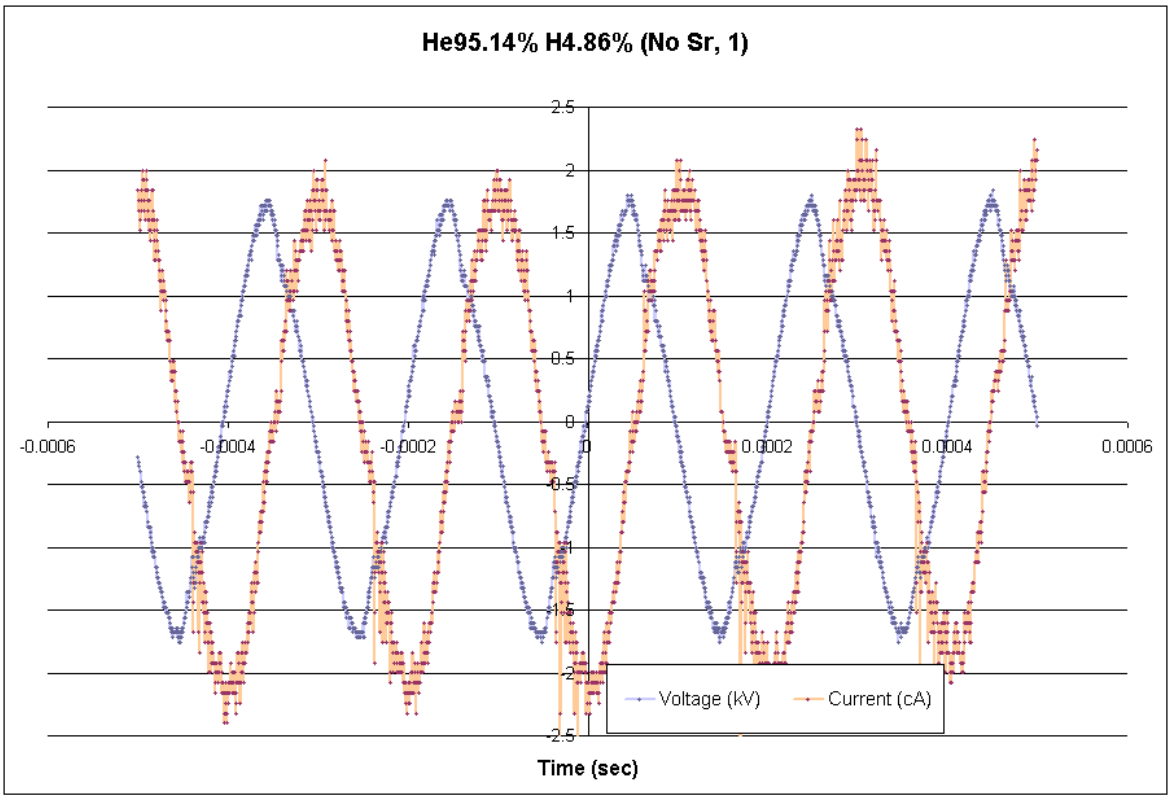
He95.14% H4.86% (No Sr, 1)
2.5
2
1.5
1
0.5
0
-0.5
-1
-1.5
-2
-2.5
-0.0006
-0.0004
-0.0002
0
0.0002
0.0004
0.0006
Voltage (kV)
Current (cA)
Time (sec)

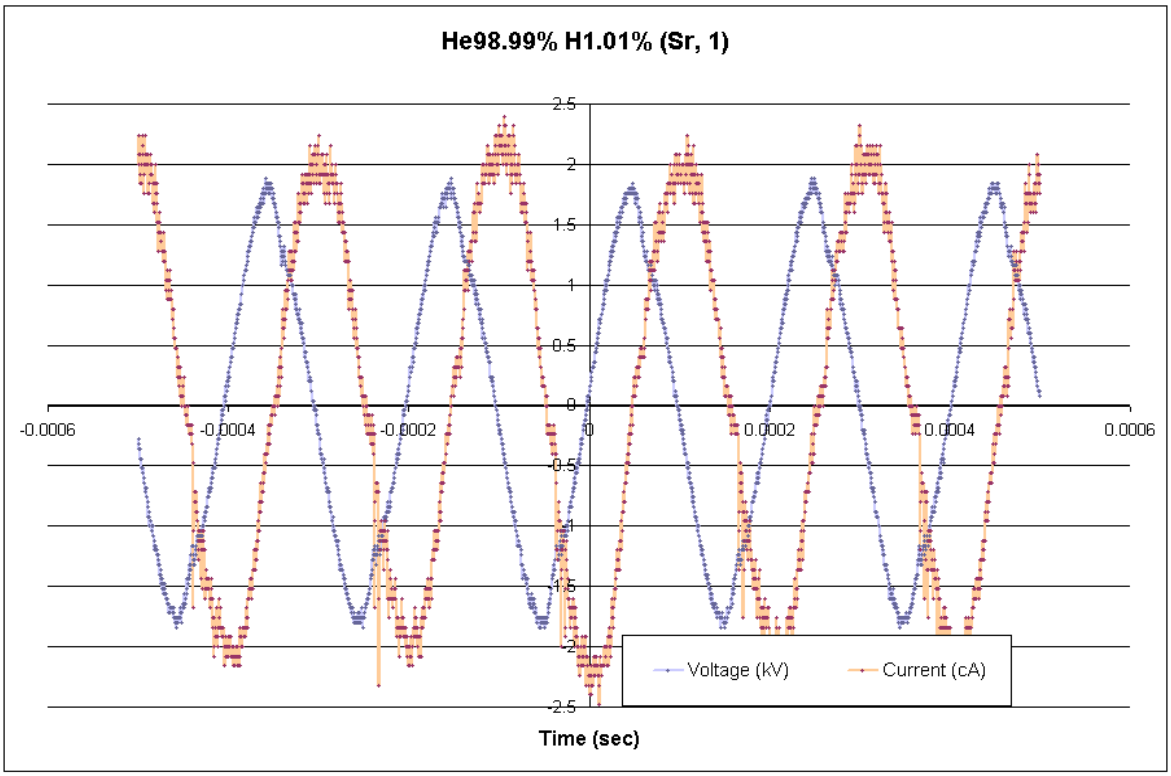
He98.99% H1.01% (Sr, 1)
2.5
2
1.5
1
0.5
0
-0.5
-1
-1.5
-2
-2.5
-0.0006
-0.0004
-0.0002
0
0.0002
0.0004
0.0006
Voltage (kV)
Current (cA)
Time (sec)

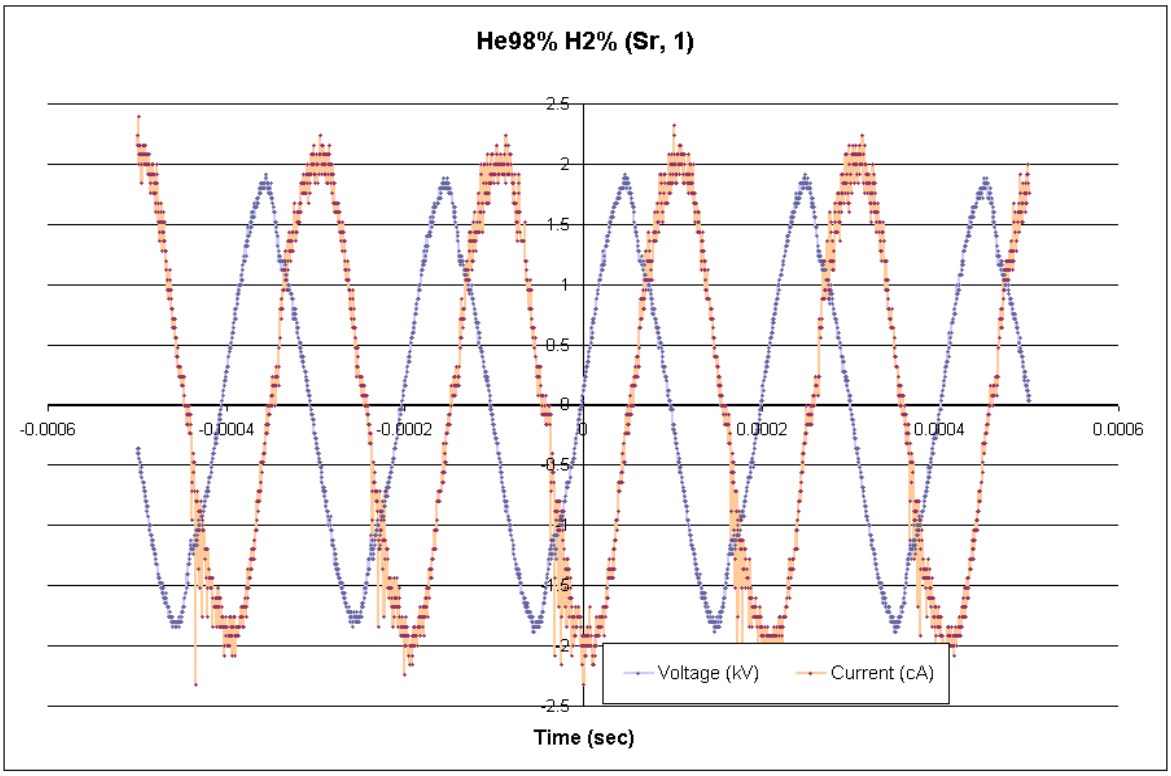
He98% H2% (Sr, 1)
2.5
2
1.5
1
0.5
0
-0.5
-1
-1.5
-2
-2.5
-0.0006
-0.0004
-0.0002
0
0.0002
0.0004
0.0006
Voltage (kV)
Current (cA)
Time (sec)

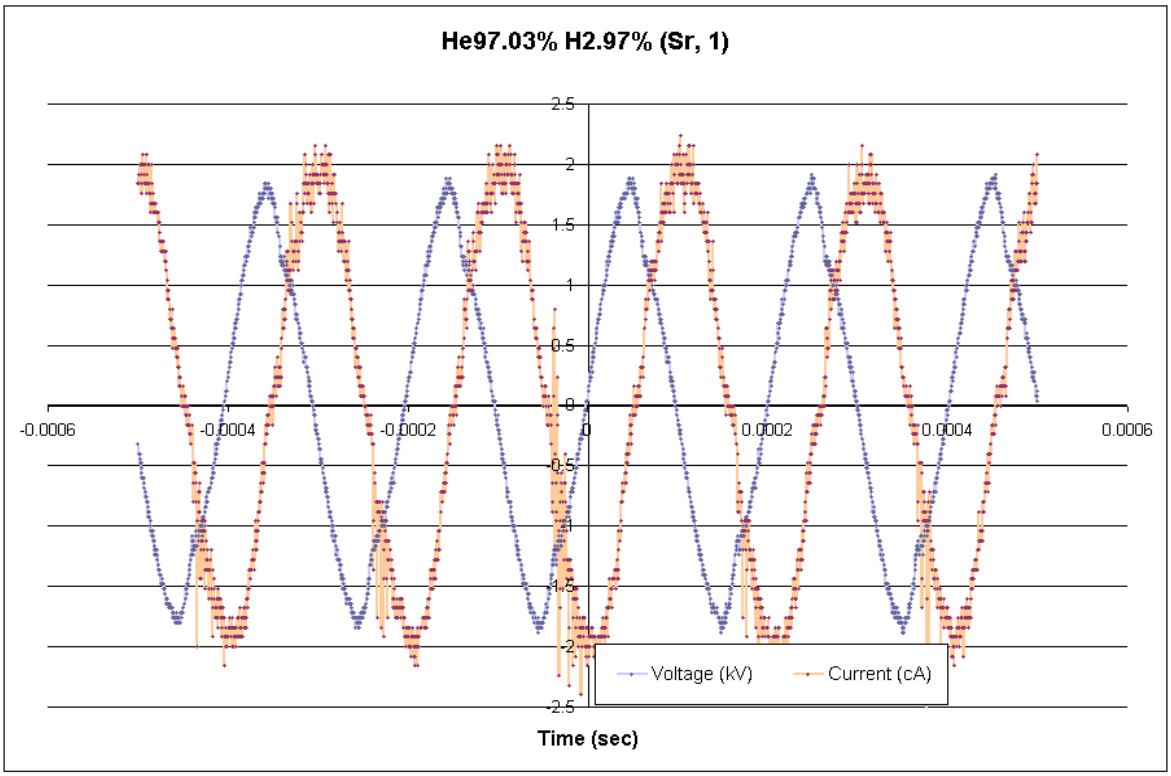
He97.03% H2.97% (Sr, 1)
2.5
2
1.5
1
0.5
0
-0.5
-1
-1.5
-2
-2.5
-0.0006
-0.0004
-0.0002
0
0.0002
0.0004
0.0006
Voltage (kV)
Current (cA)
Time (sec)

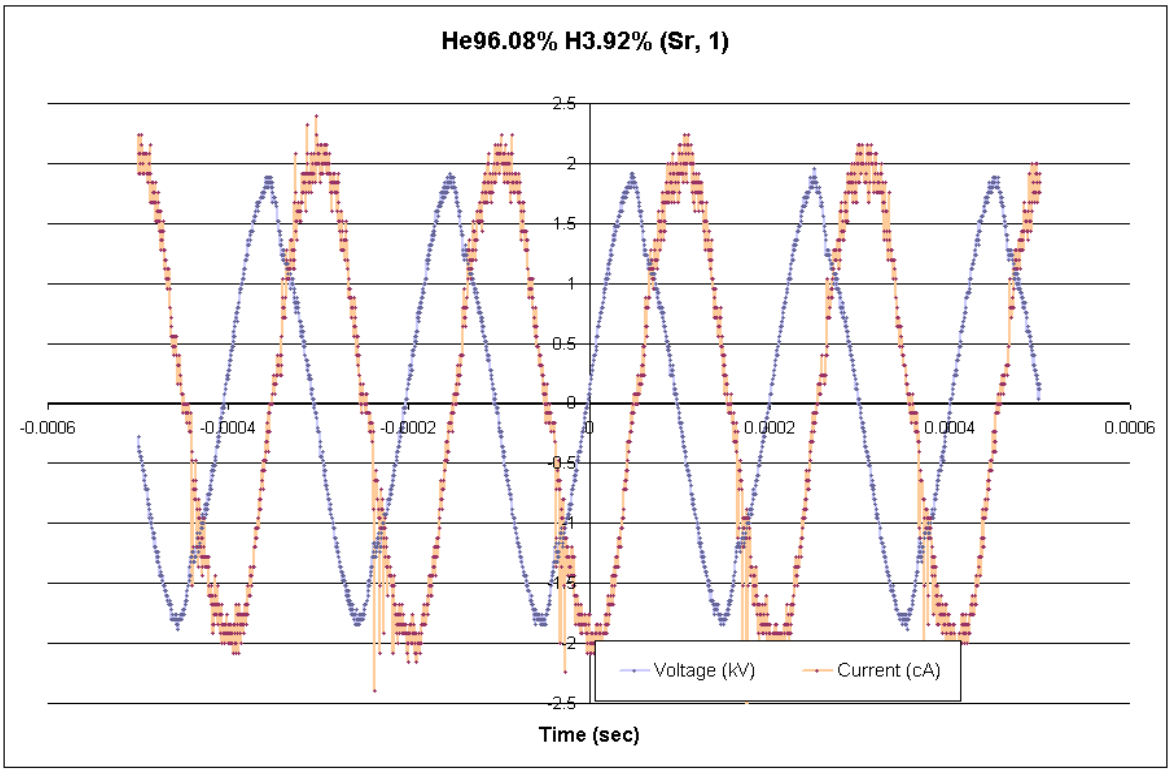
He96.08% H3.92% (Sr, 1)
2.5
2
1.5
1
0.5
0
-0.5
-1
-1.5
-2
-2.5
-0.0006
-0.0004
-0.0002
0
0.0002
0.0004
0.0006
Voltage (kV)
Current (cA)
Time (sec)

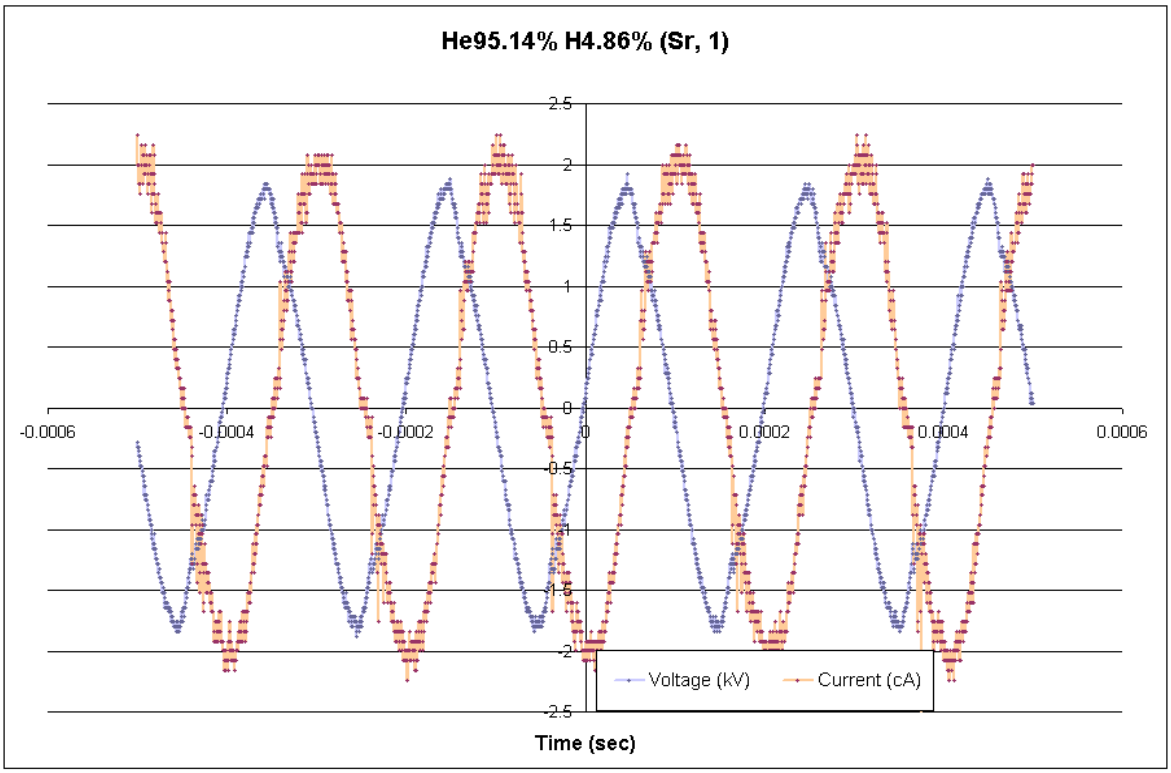
He95.14% H4.86% (Sr, 1)
2.5
2
1.5
1
0.5
0
-0.5
-1
-1.5
-2
-2.5
-0.0006
-0.0004
-0.0002
0
0.0002
0.0004
0.0006
Voltage (kV)
Current (cA)
Time (sec)

Appendix B: Data Set 2; Voltage and Current Waveforms

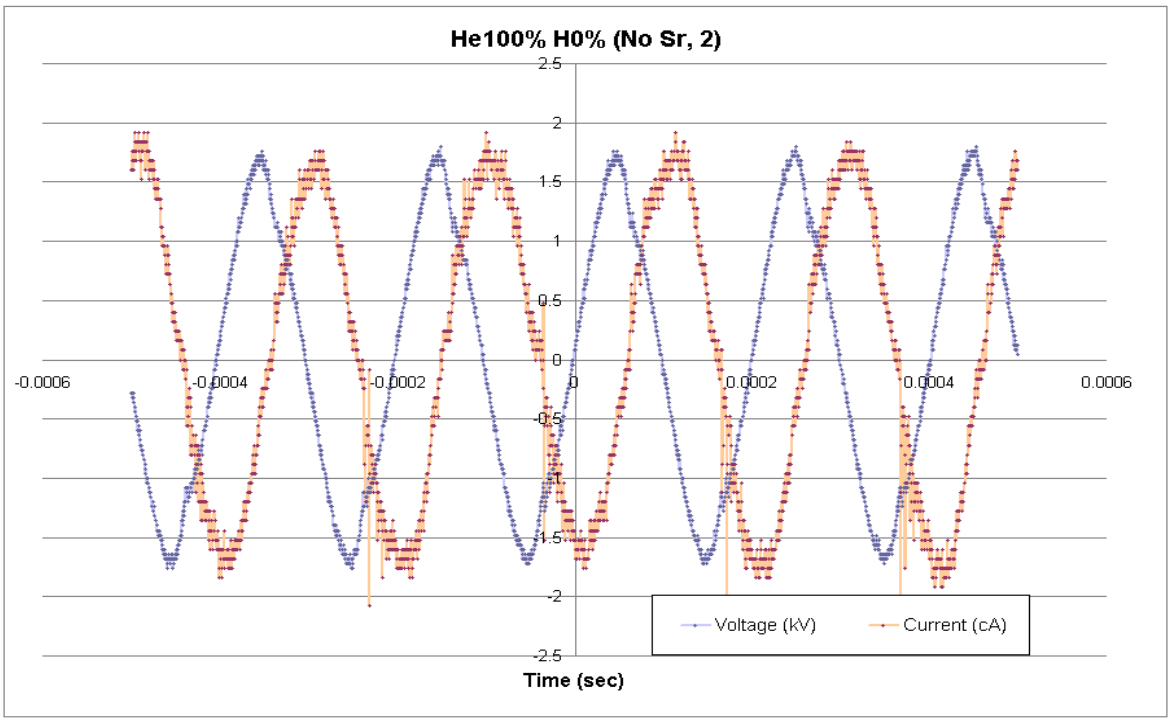

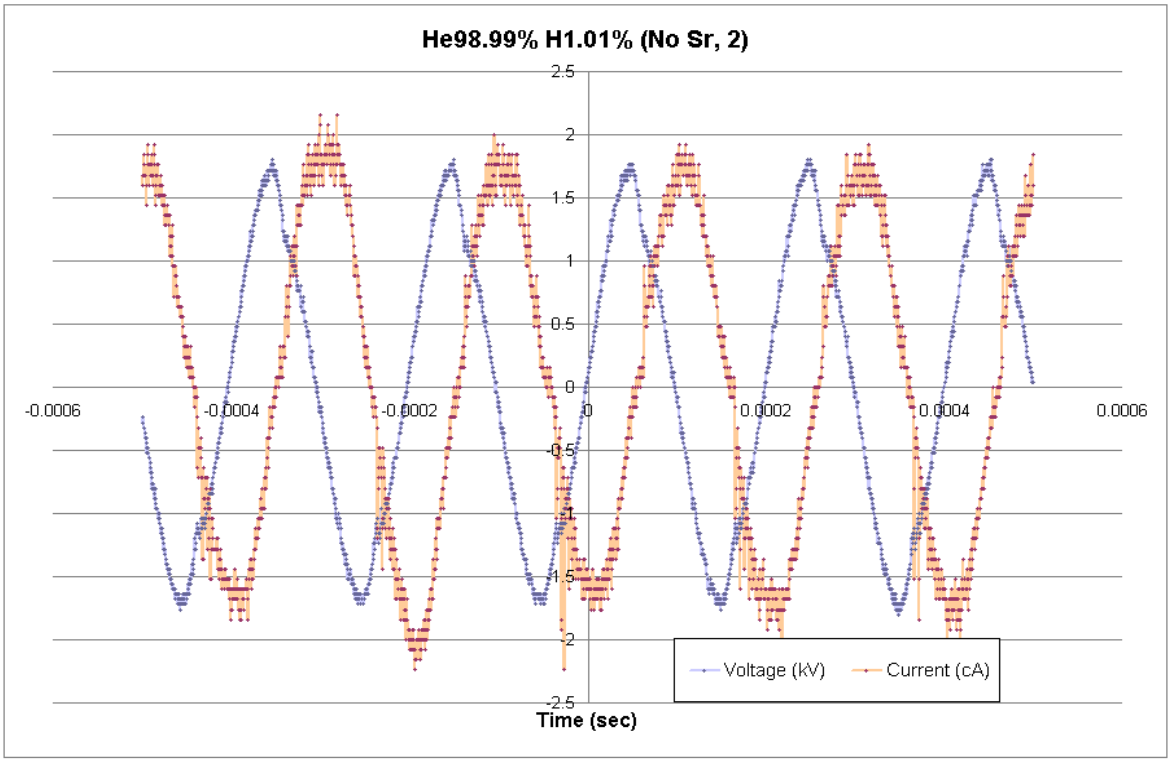

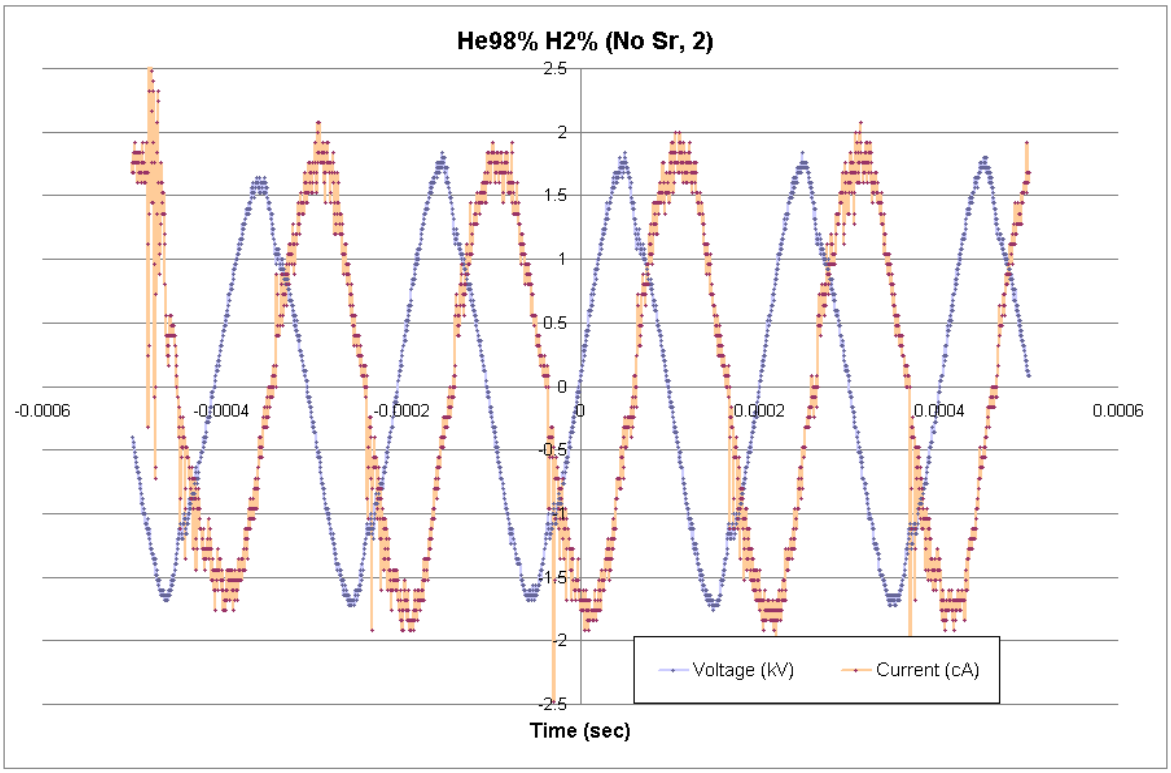
He98% H2% (No Sr, 2)
2.5
2
1.5
1
0.5
0
-0.5
-1
-1.5
-2
-2.5
-0.0006
-0.0004
-0.0002
0
0.0002
0.0004
0.0006
Voltage (kV)
Current (cA)
Time (sec)

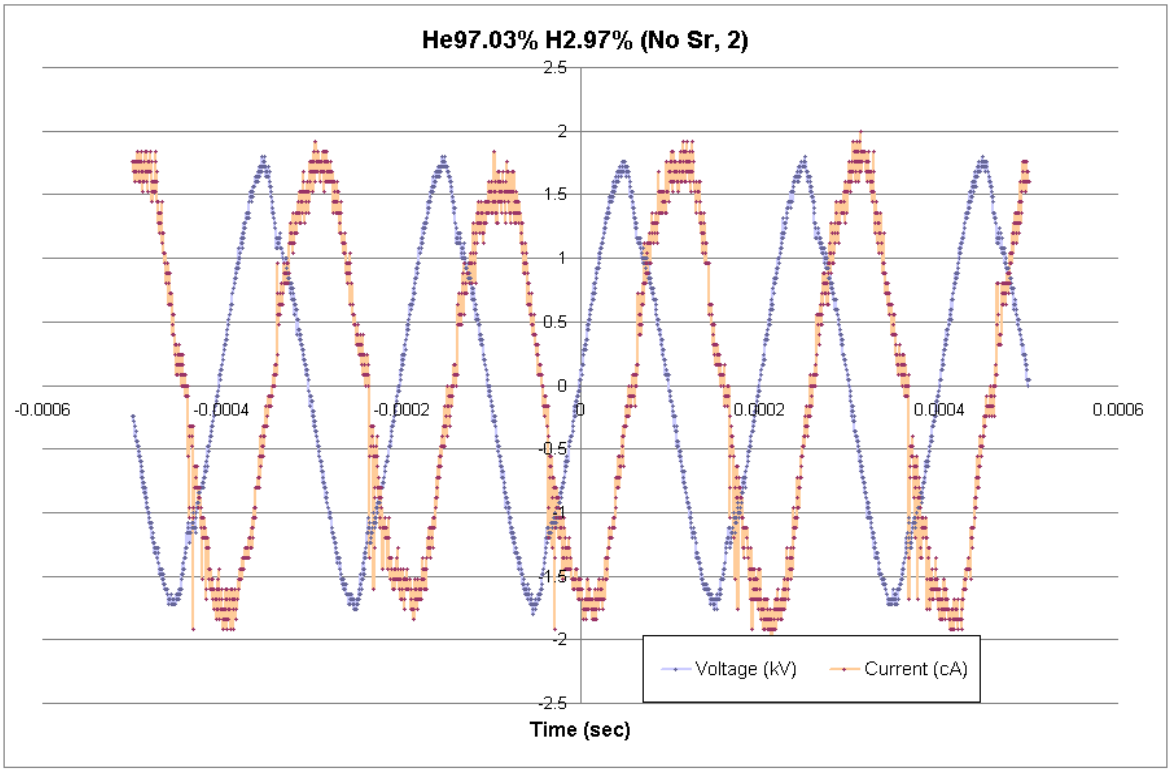
He97.03% H2.97% (No Sr, 2)
2.5
2
1.5
1
0.5
0
-0.5
-1
-1.5
-2
-2.5
-0.0006
-0.0004
-0.0002
0
0.0002
0.0004
0.0006
Voltage (kV)
Current (cA)
Time (sec)

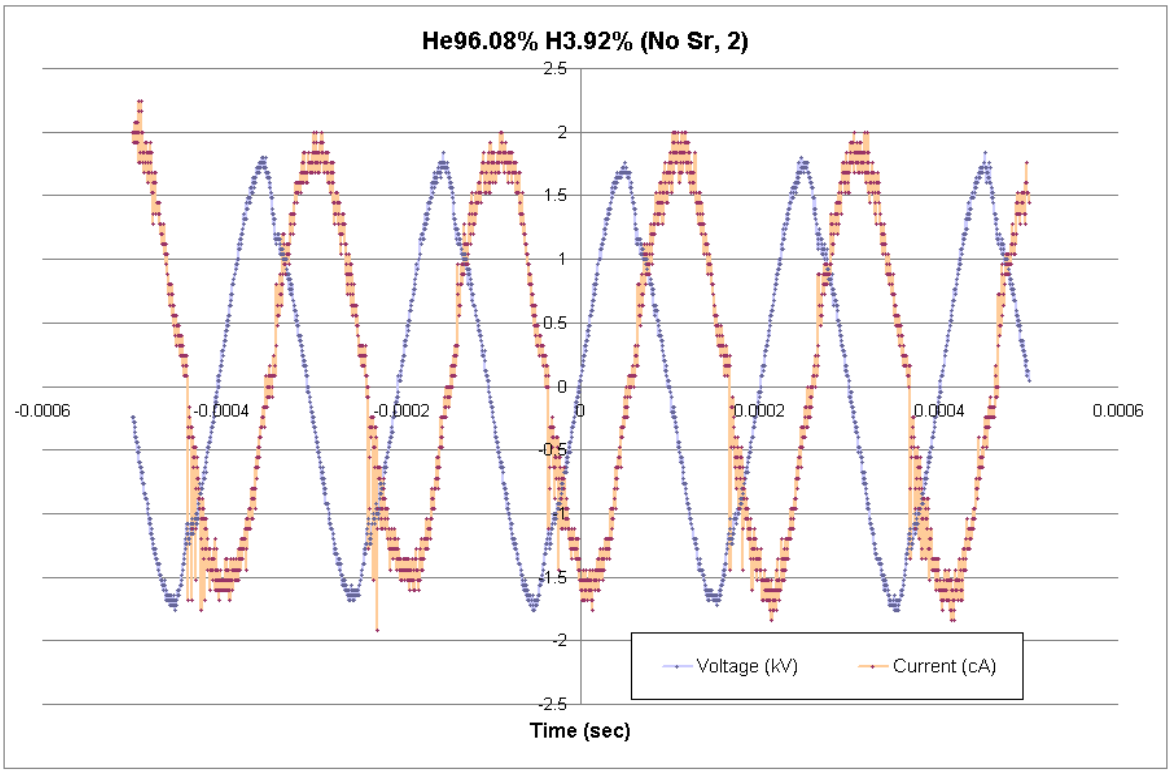
He96.08% H3.92% (No Sr, 2)
2.5
2
1.5
1
0.5
0
-0.5
-1
-1.5
-2
-2.5
-0.0006
-0.0004
-0.0002
0
0.0002
0.0004
0.0006
Voltage (kV)
Current (cA)
Time (sec)

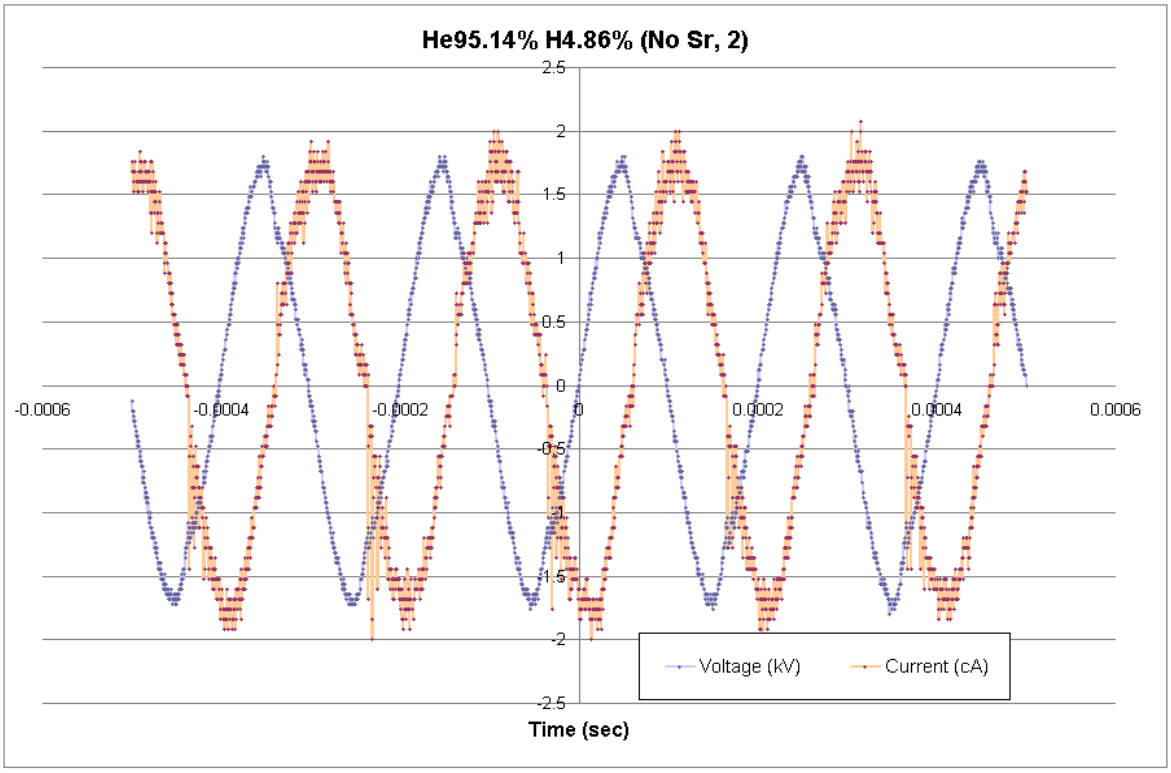
He95.14% H4.86% (No Sr, 2)
2.5
2
1.5
1
0.5
0
-0.5
-1
-1.5
-2
-2.5
-0.0006
-0.0004
-0.0002
0
0.0002
0.0004
0.0006
Voltage (kV)
Current (cA)
Time (sec)

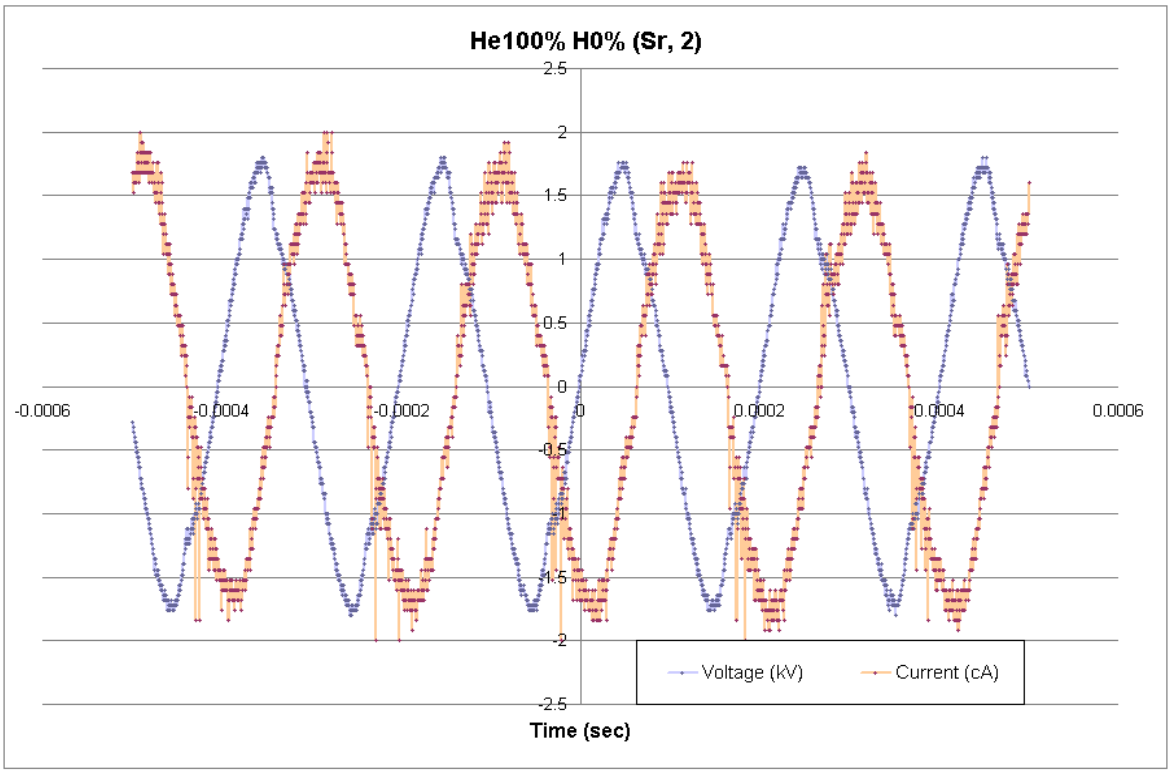
He100% H0% (Sr, 2)
2.5
2
1.5
1
0.5
0
-0.5
-1
-1.5
-2
-2.5
-0.0006
-0.0004
-0.0002
0
0.0002
0.0004
0.0006
Voltage (kV)
Current (cA)
Time (sec)

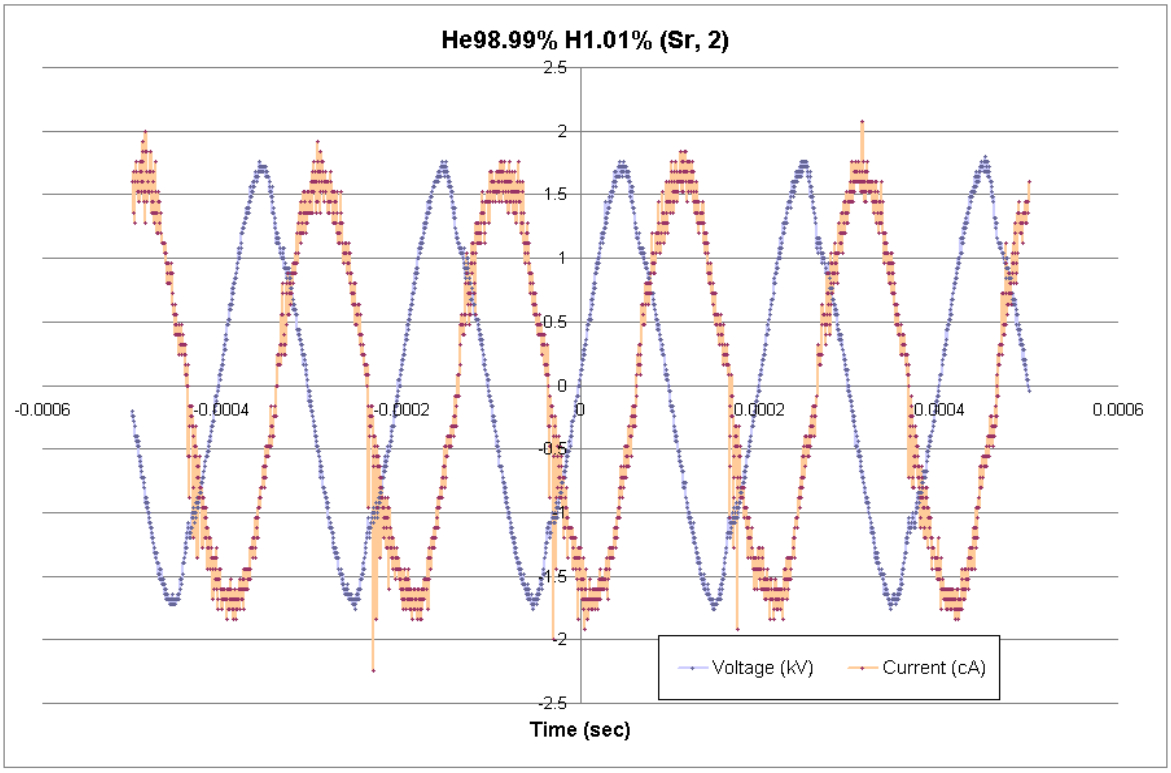
He98.99% H1.01% (Sr, 2)
2.5
2
1.5
1
0.5
0
-0.5
-1
-1.5
-2
-2.5
-0.0006
-0.0004
-0.0002
0
0.0002
0.0004
0.0006
Voltage (kV)
Current (cA)
Time (sec)

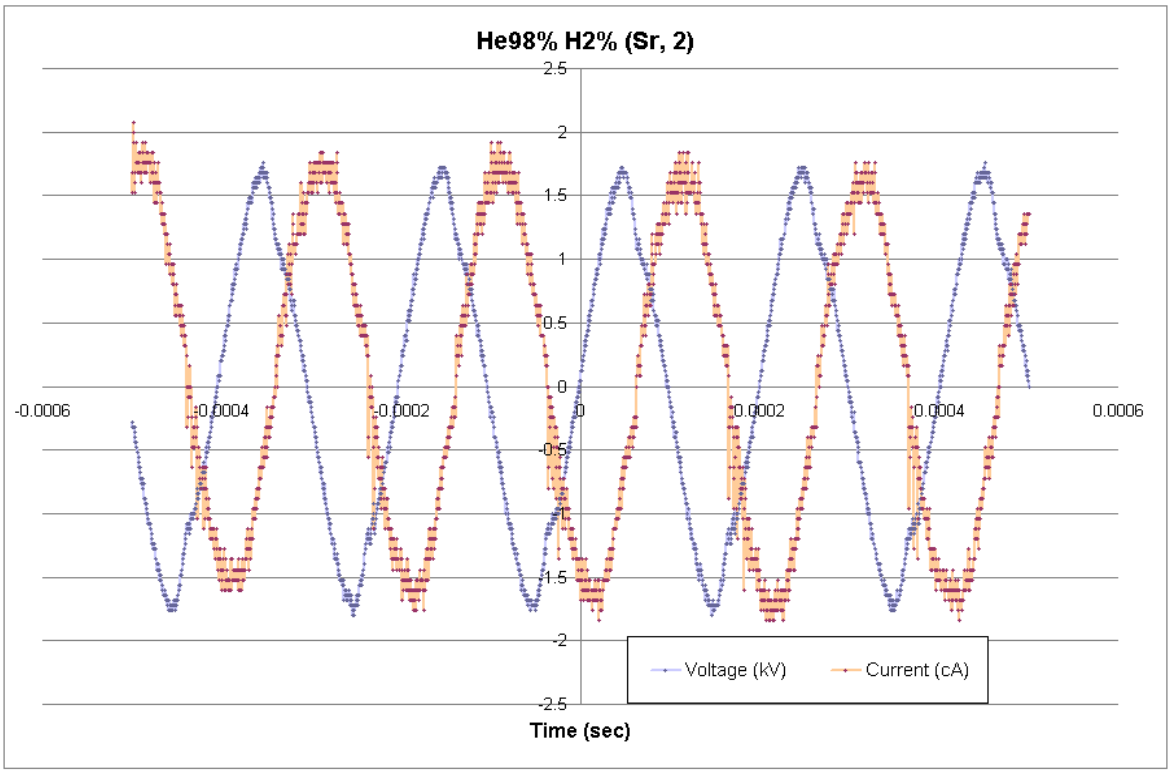
He98% H2% (Sr, 2)
2.5
2
1.5
1
0.5
0
-0.5
-1
-1.5
-2
-2.5
-0.0006
-0.0004
-0.0002
0
0.0002
0.0004
0.0006
Voltage (kV)
Current (cA)
Time (sec)

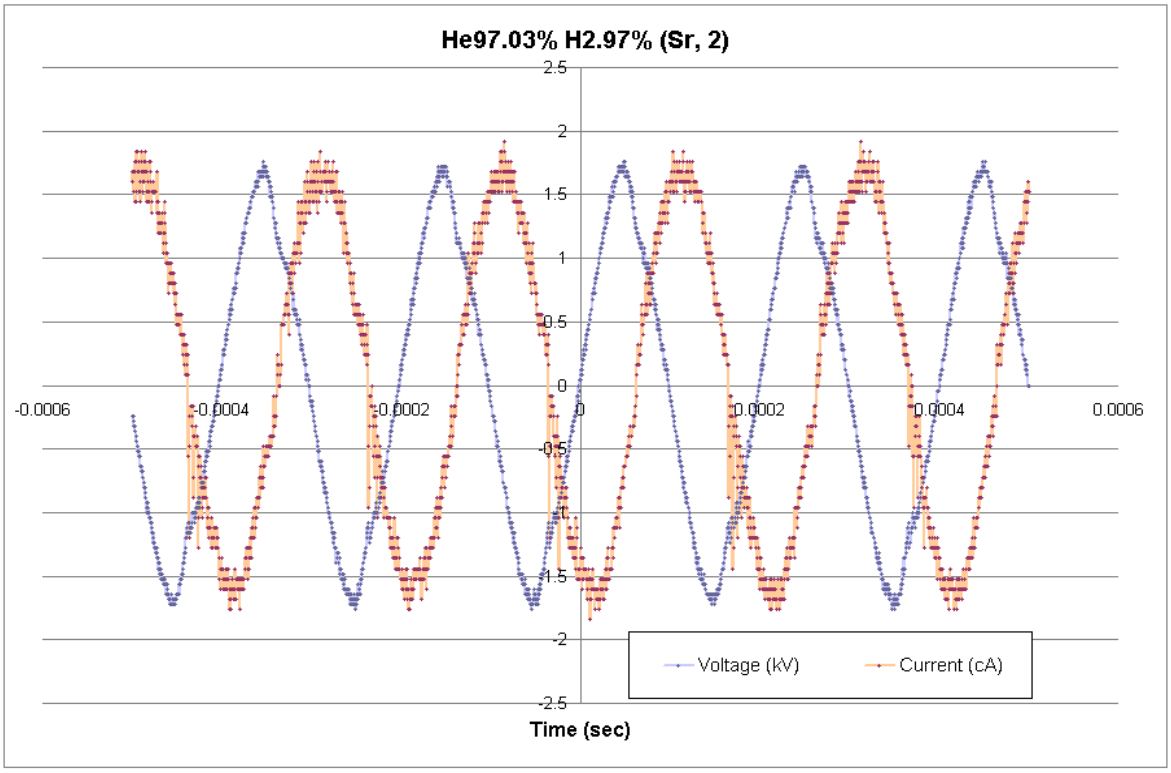
He97.03% H2.97% (Sr, 2)
2.5
2
1.5
1
0.5
0
-0.5
-1
-1.5
-2
-2.5
-0.0006
-0.0004
-0.0002
0
0.0002
0.0004
0.0006
Voltage (kV)
Current (cA)
Time (sec)

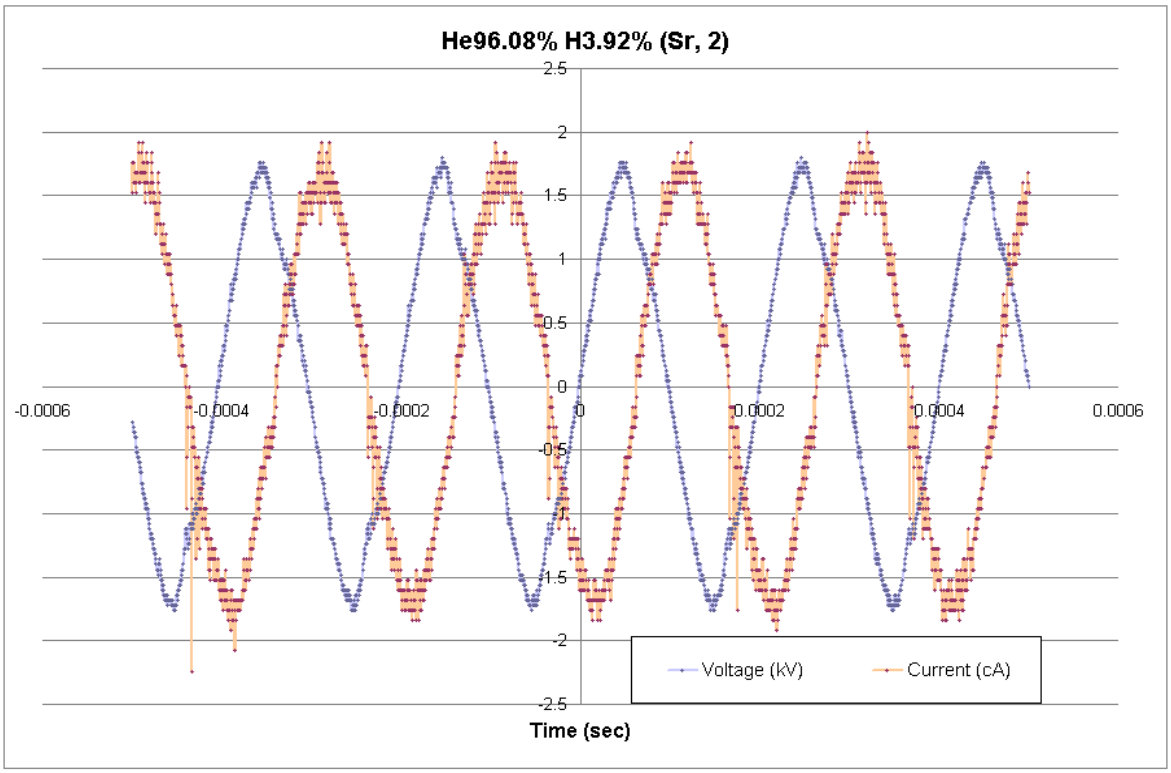
He96.08% H3.92% (Sr, 2)
2.5
2
1.5
1
0.5
0
-0.5
-1
-1.5
-2
-2.5
-0.0006
-0.0004
-0.0002
0
0.0002
0.0004
0.0006
Voltage (kV)
Current (cA)
Time (sec)

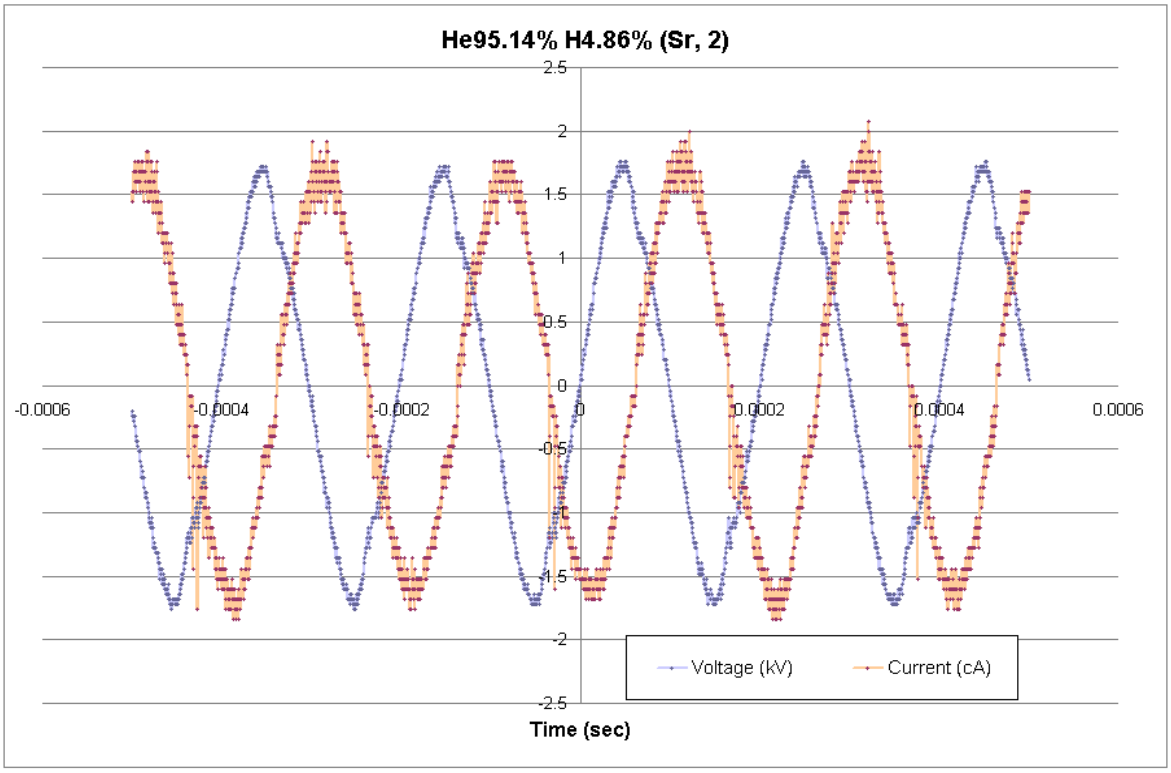
He95.14% H4.86% (Sr, 2)
2.5
2
1.5
1
0.5
0
-0.5
-1
-1.5
-2
-2.5
-0.0006
-0.0004
-0.0002
0
0.0002
0.0004
0.0006
Voltage (kV)
Current (cA)
Time (sec)

Appendix C: Data Set 1; Thermal Data

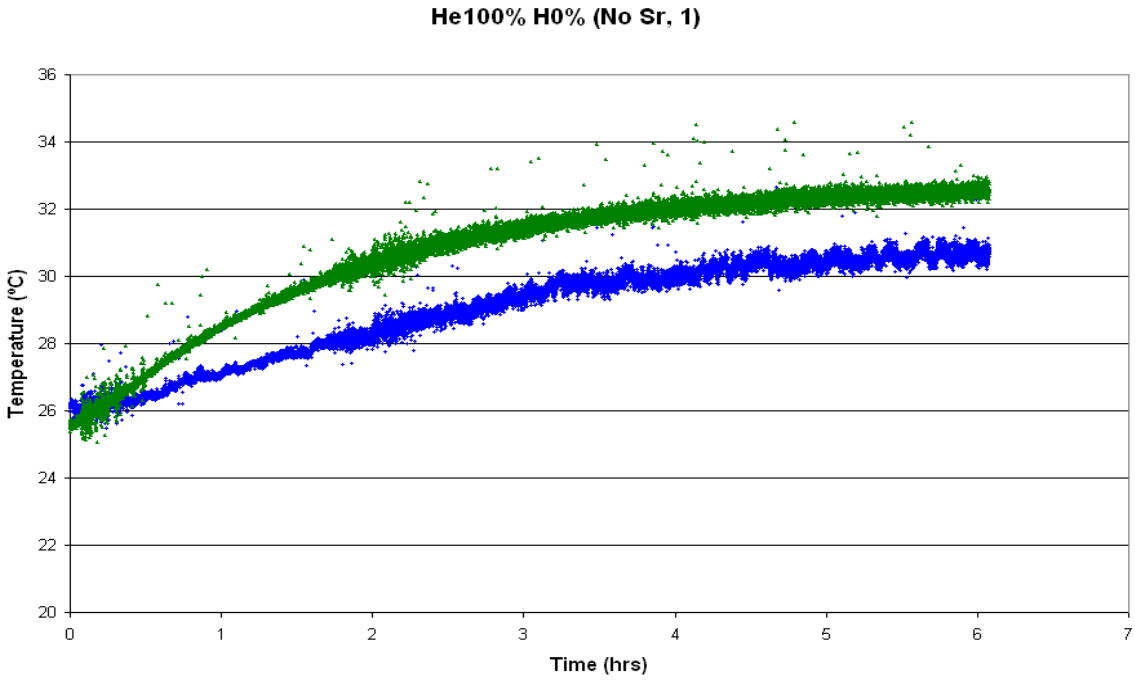

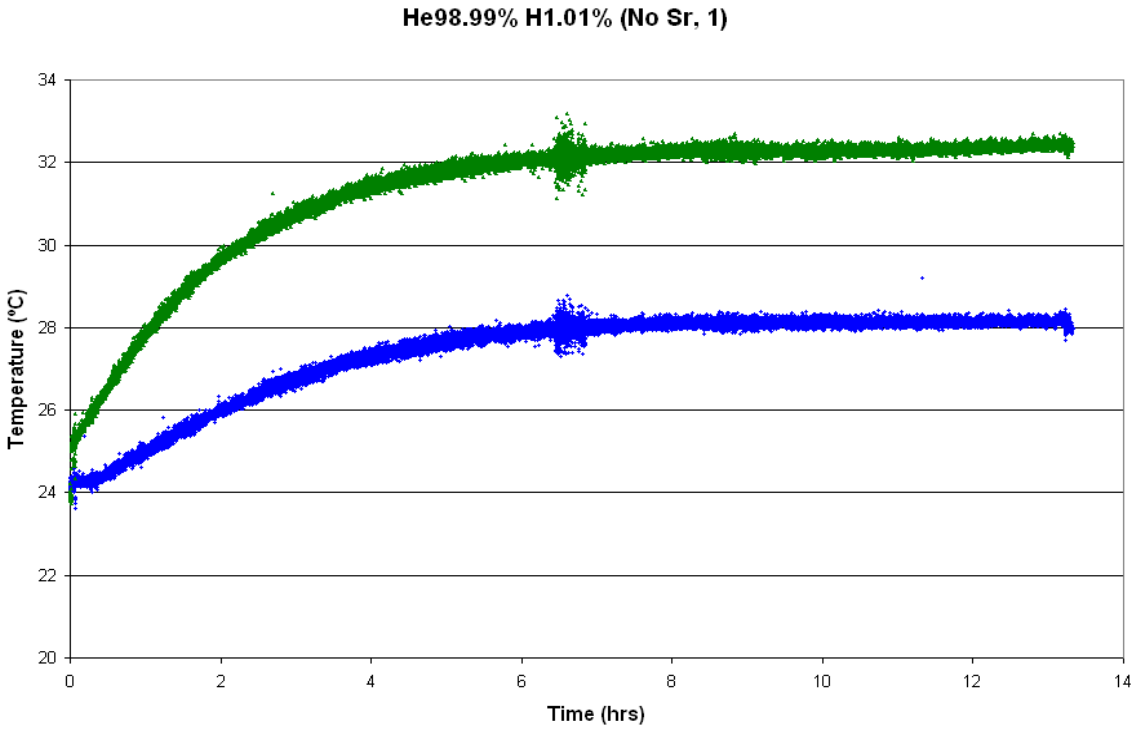

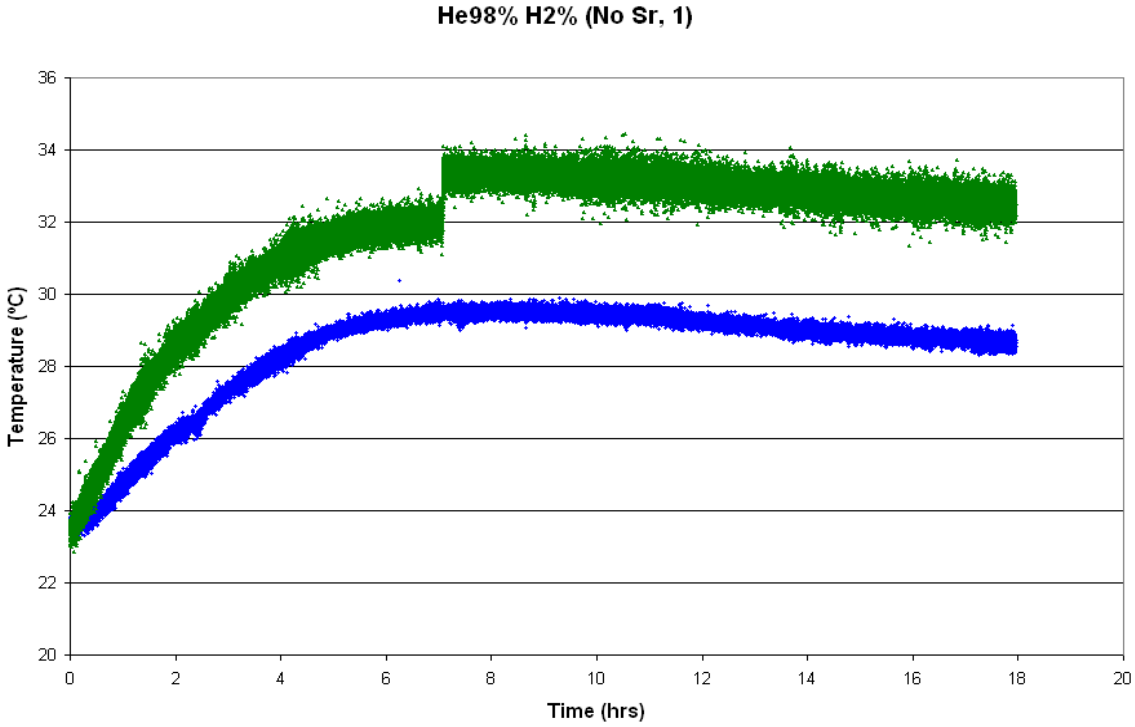
He98% H2% (No Sr, 1)
Temperature (ºC)
Time (hrs)
36
34
32
30
28
26
24
22
20
0
2
4
6
8
10
12
14
16
18
20

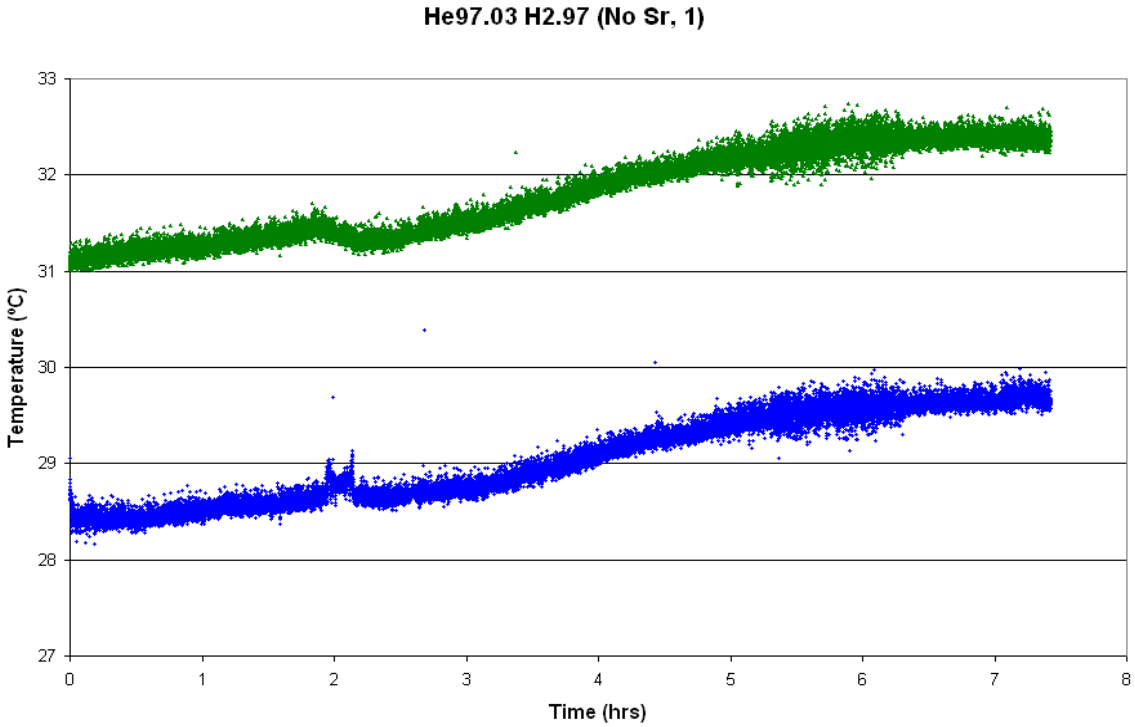
He97.03 H2.97 (No Sr, 1)
Temperature (ºC)
Time (hrs)
33
32
31
30
29
28
27
0
1
2
3
4
5
6
7
8

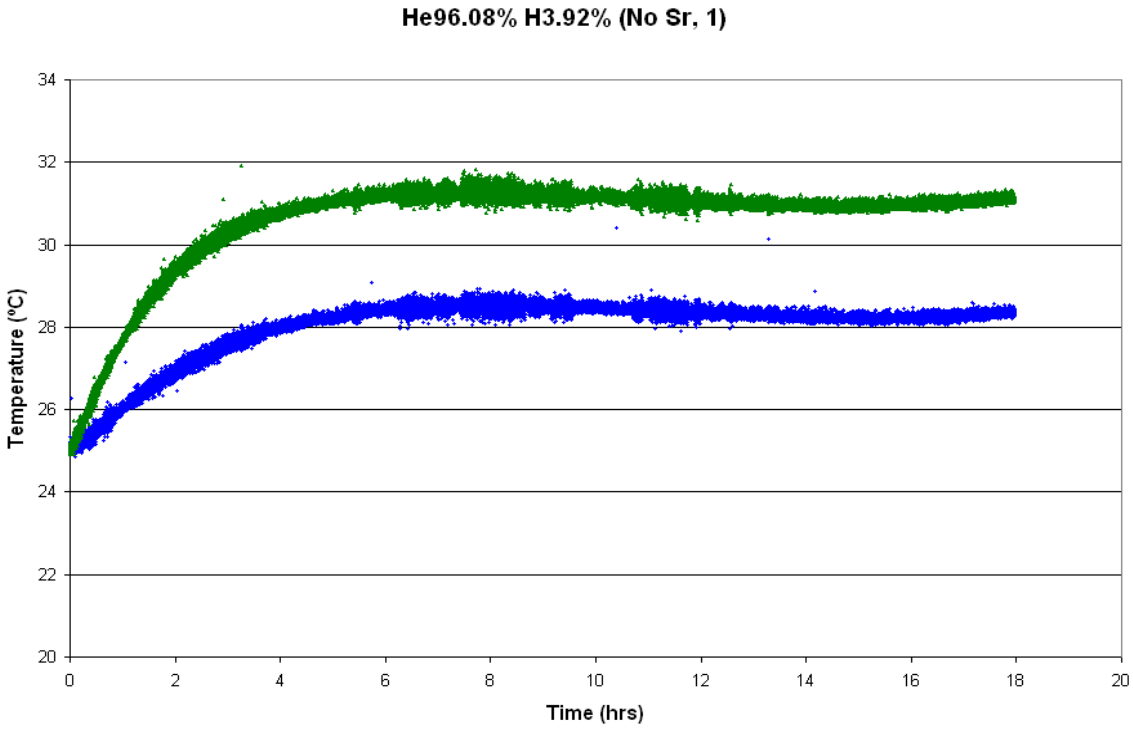
He96.08% H3.92% (No Sr, 1)
Temperature (ºC)
34
32
30
28
26
24
22
20
0
2
4
6
8
10
12
14
16
18
20
Time (hrs)

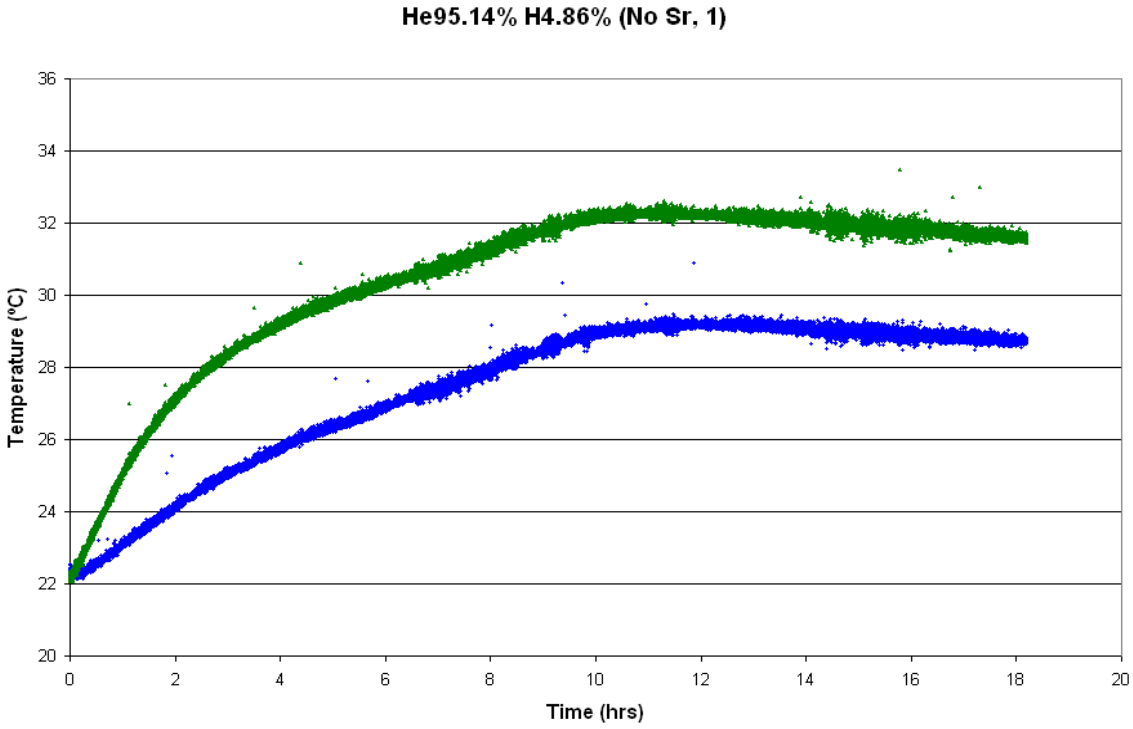
He95.14% H4.86% (No Sr, 1)
Temperature (ºC)
36
34
32
30
28
26
24
22
20
0
2
4
6
8
10
12
14
16
18
20
Time (hrs)

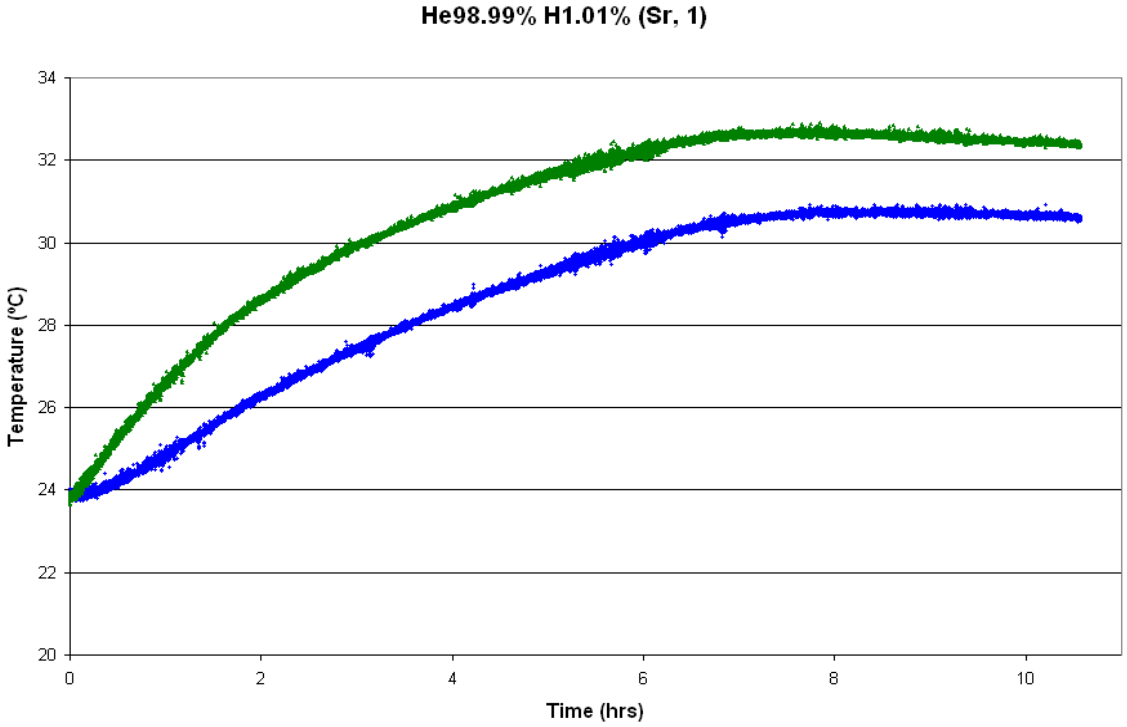
He98.99% H1.01% (Sr, 1)
Temperature (ºC)
34
32
30
28
26
24
22
20
0
2
4
6
8
10
Time (hrs)

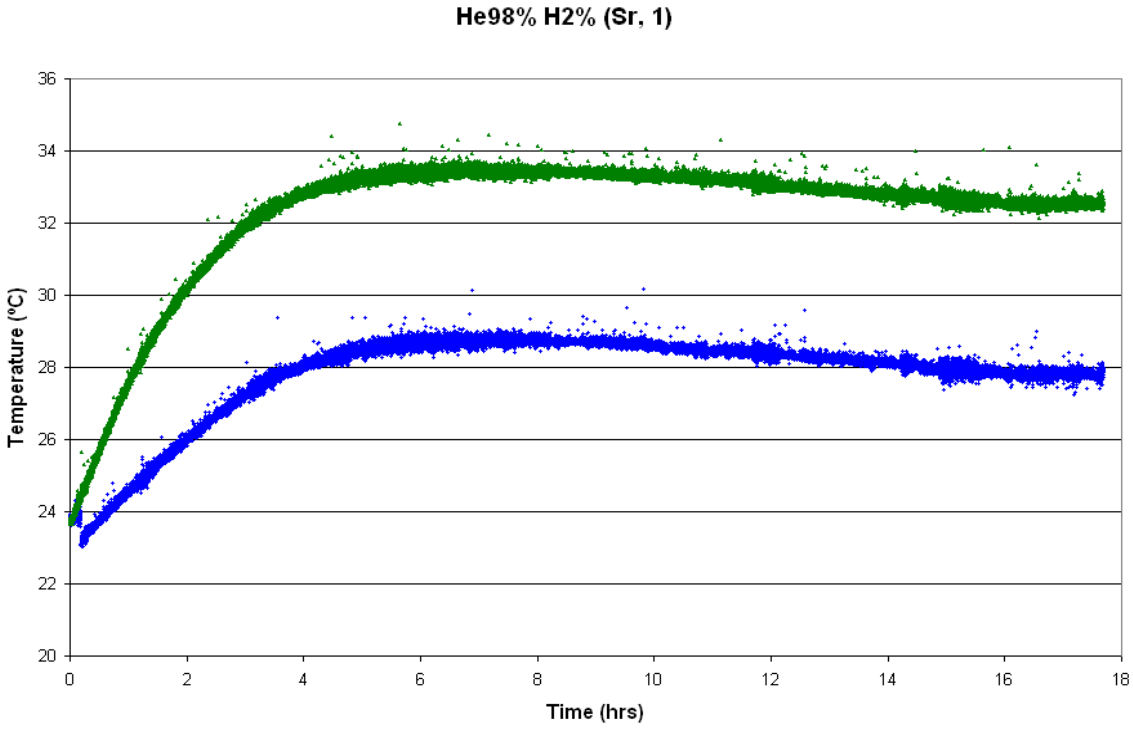
He98% H2% (Sr, 1)
Temperature (ºC)
36
34
32
30
28
26
24
22
20
0
2
4
6
8
10
12
14
16
18
Time (hrs)

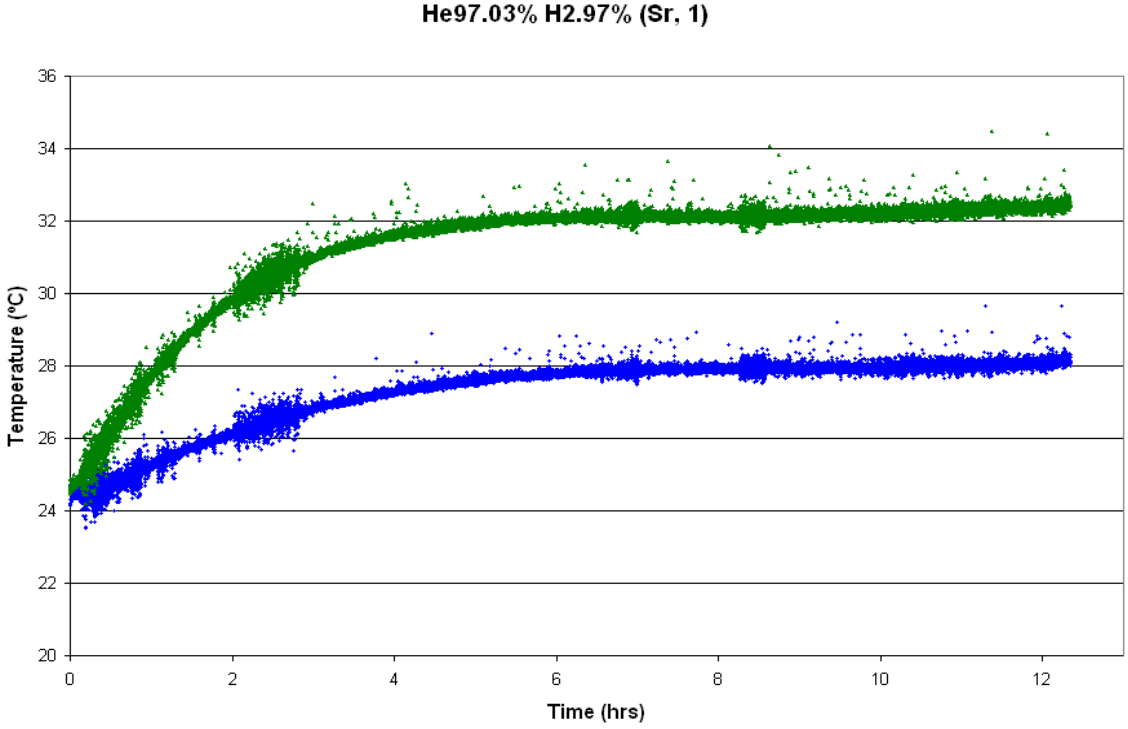
He97.03% H2.97% (Sr, 1)
Temperature (°C)
Time (hrs)
36
34
32
30
28
26
24
22
20
0
2
4
6
8
10
12

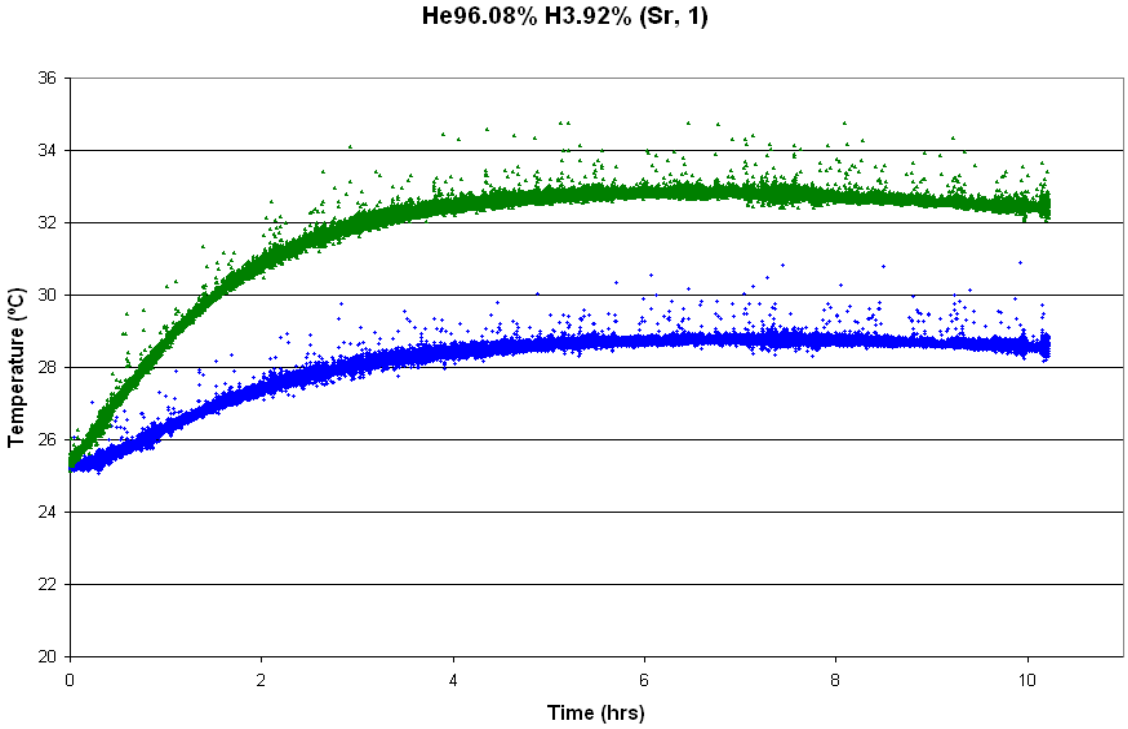
He96.08% H3.92% (Sr, 1)
Temperature (°C)
Time (hrs)
36
34
32
30
28
26
24
22
20
0
2
4
6
8
10

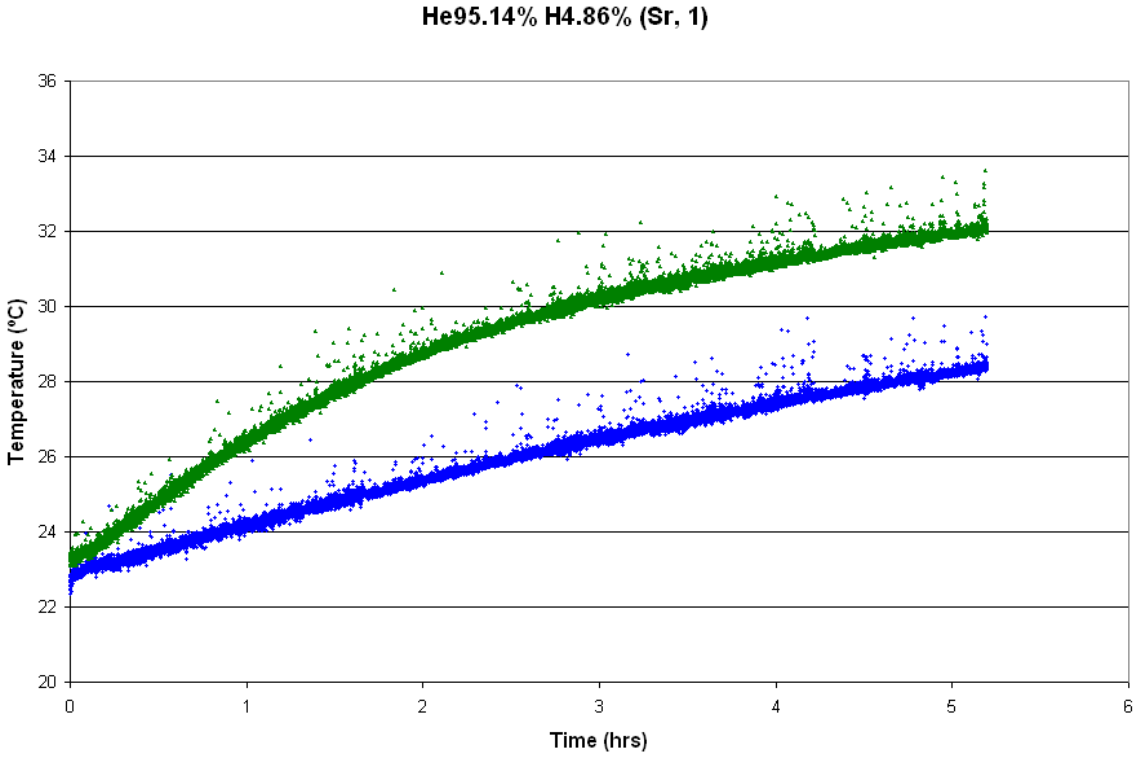
He95.14% H4.86% (Sr, 1)
Temperature (ºC)
Time (hrs)
36
34
32
30
28
26
24
22
20
0
1
2
3
4
5
6

Appendix D: Data Set 2; Thermal Data

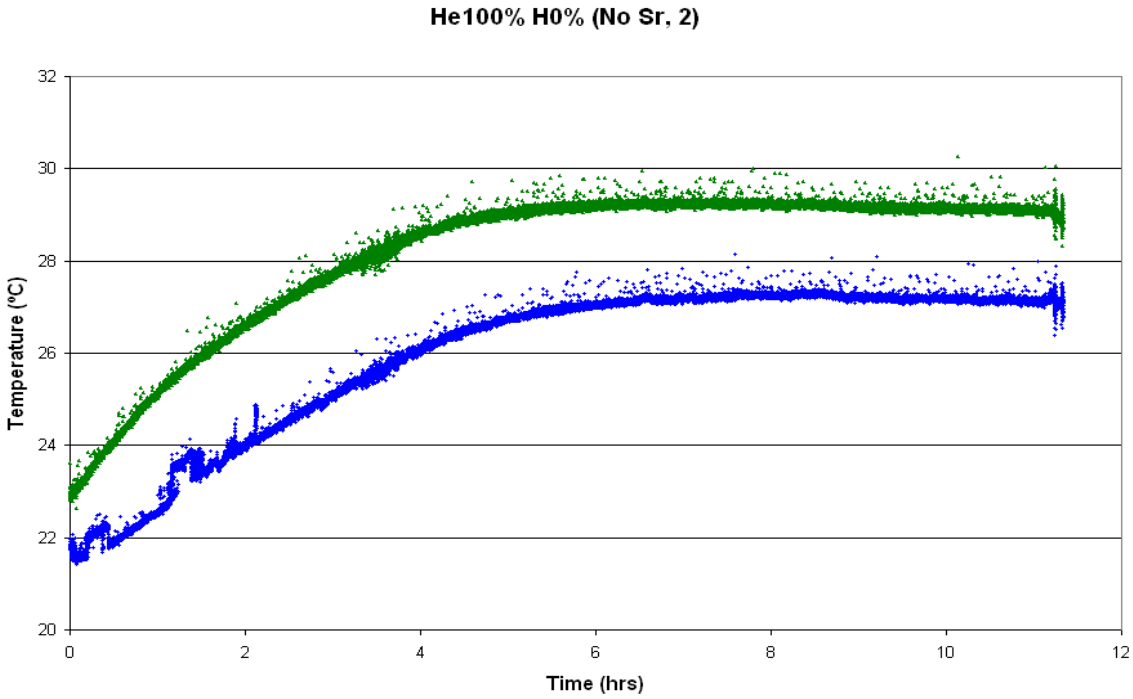

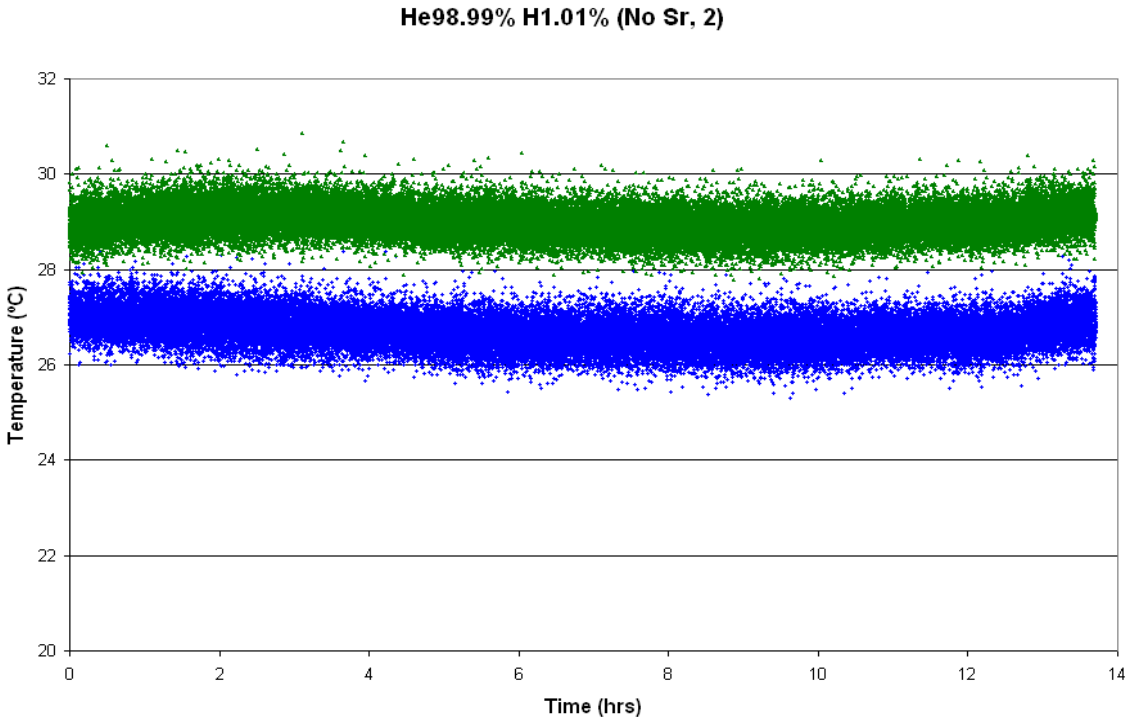

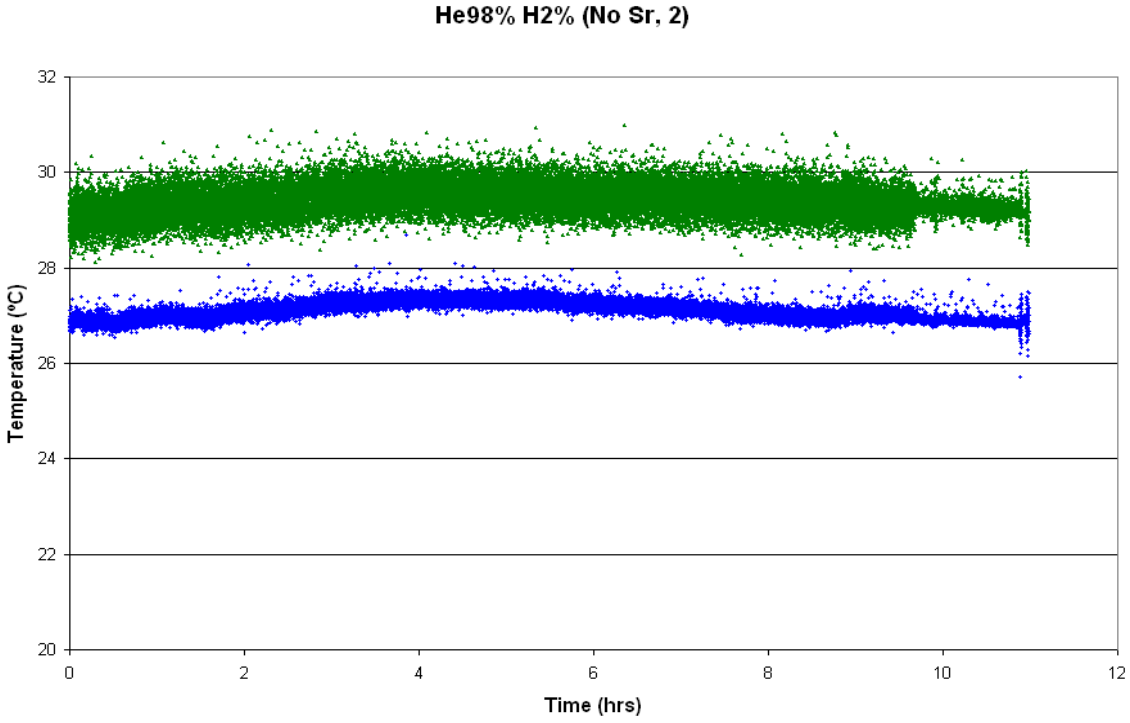
He98% H2% (No Sr, 2)
Temperature (°C)
Time (hrs)
32
30
28
26
24
22
20
0
2
4
6
8
10
12

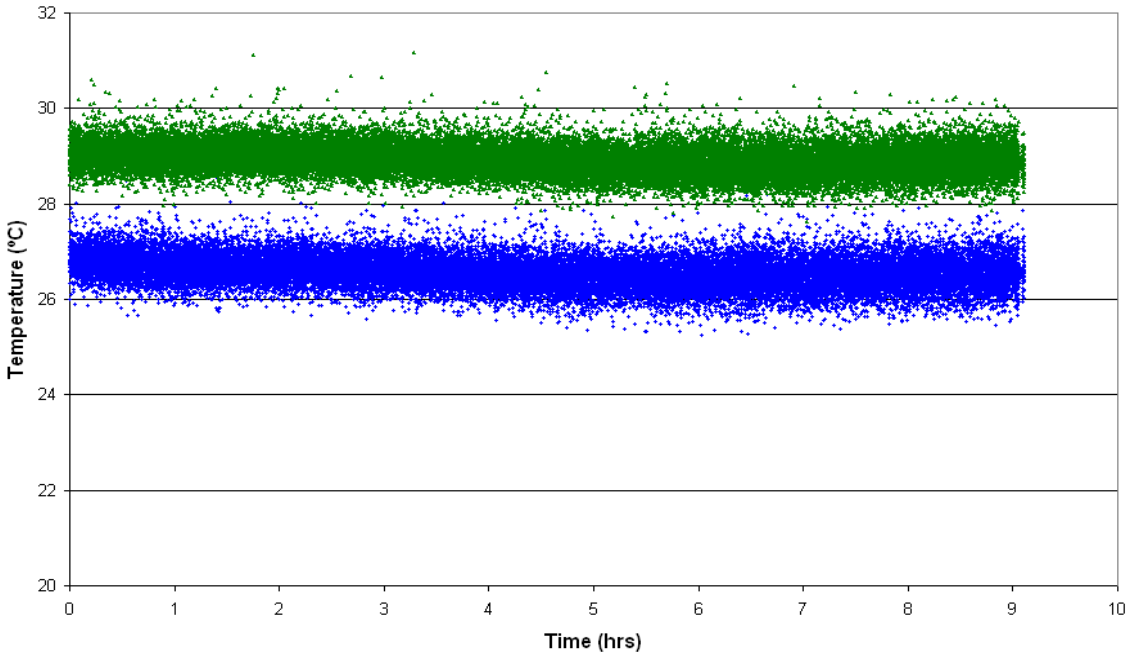
He97.03% H2.97% (No Sr, 2)
Temperature (°C)
Time (hrs)
32
30
28
26
24
22
20
0
1
2
3
4
5
6
7
8
9
10

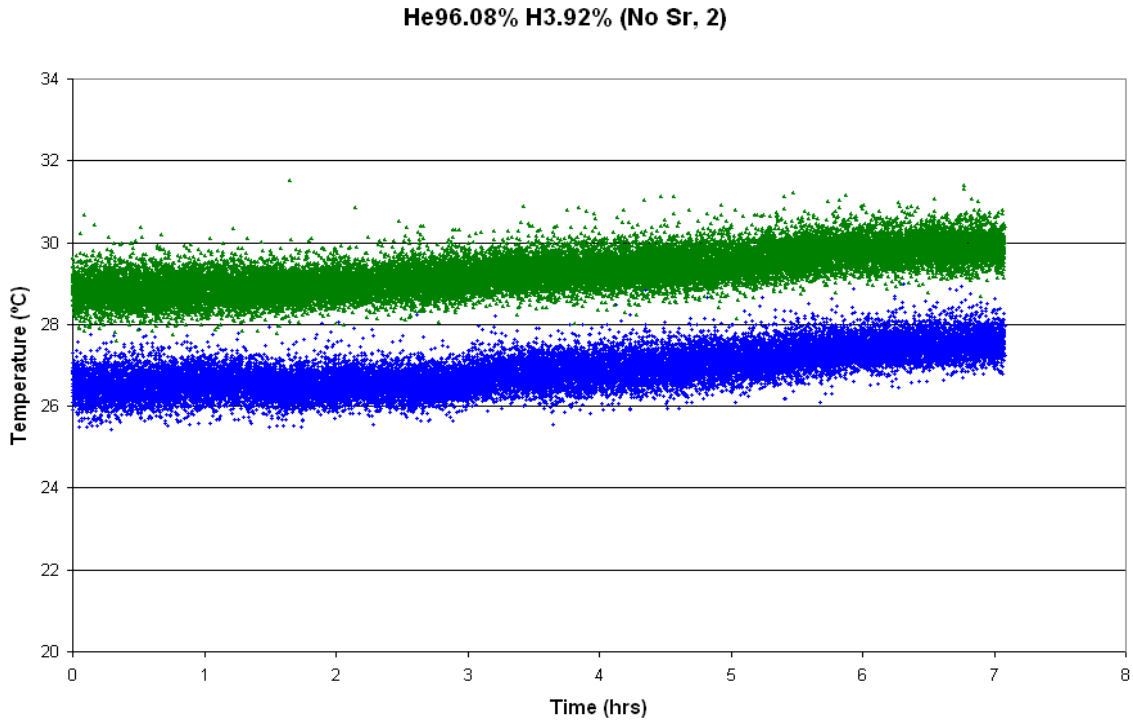
He96.08% H3.92% (No Sr, 2)
Temperature (°C)
Time (hrs)
34
32
30
28
26
24
22
20
0
1
2
3
4
5
6
7
8

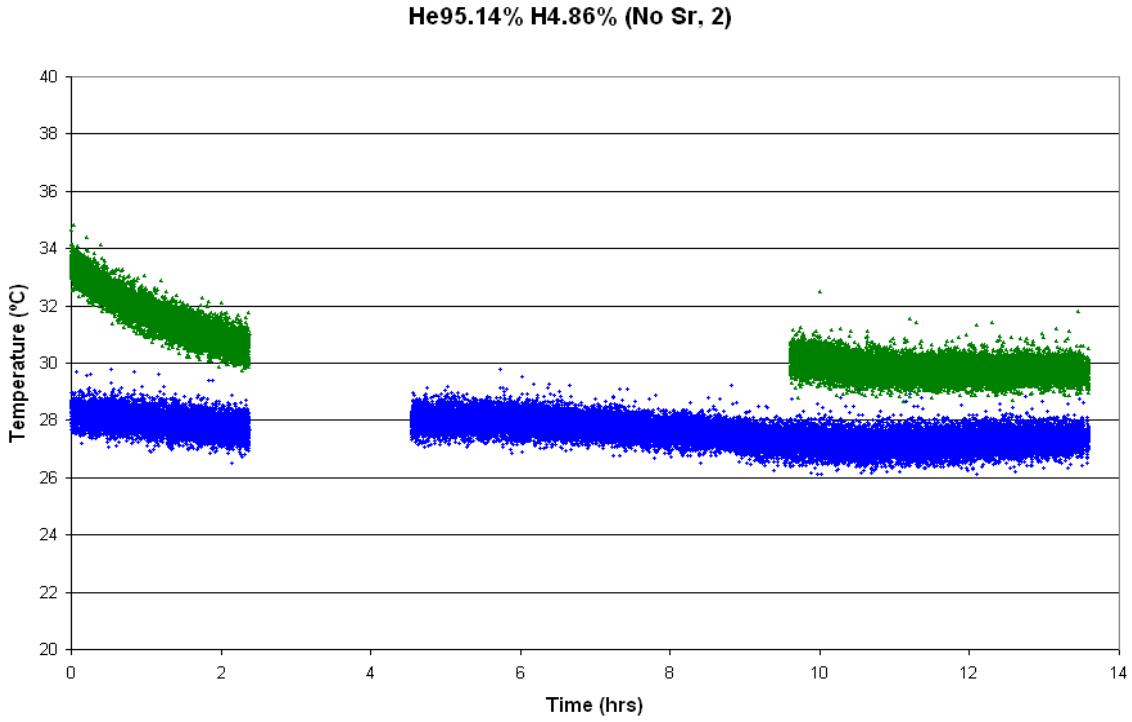
He95.14% H4.86% (No Sr, 2)
Temperature (°C)
Time (hrs)
40
38
36
34
32
30
28
26
24
22
20
0
2
4
6
8
10
12
14

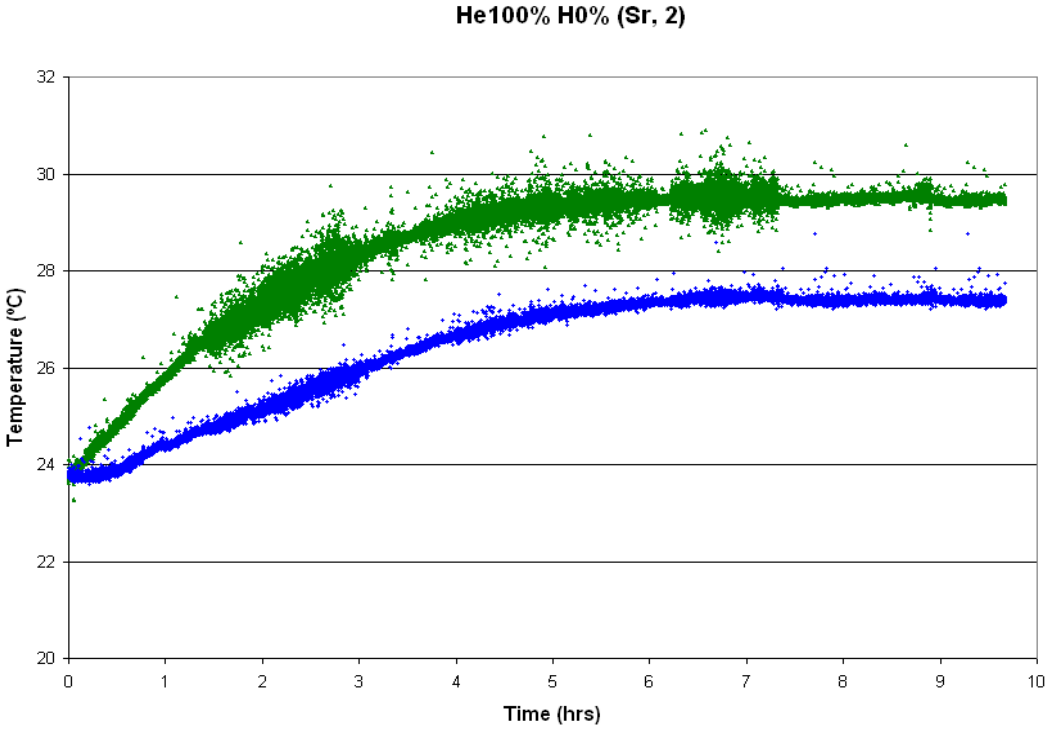
He100% H0% (Sr, 2)
Temperature (°C)
Time (hrs)
32
30
28
26
24
22
20
0
1
2
3
4
5
6
7
8
9
10

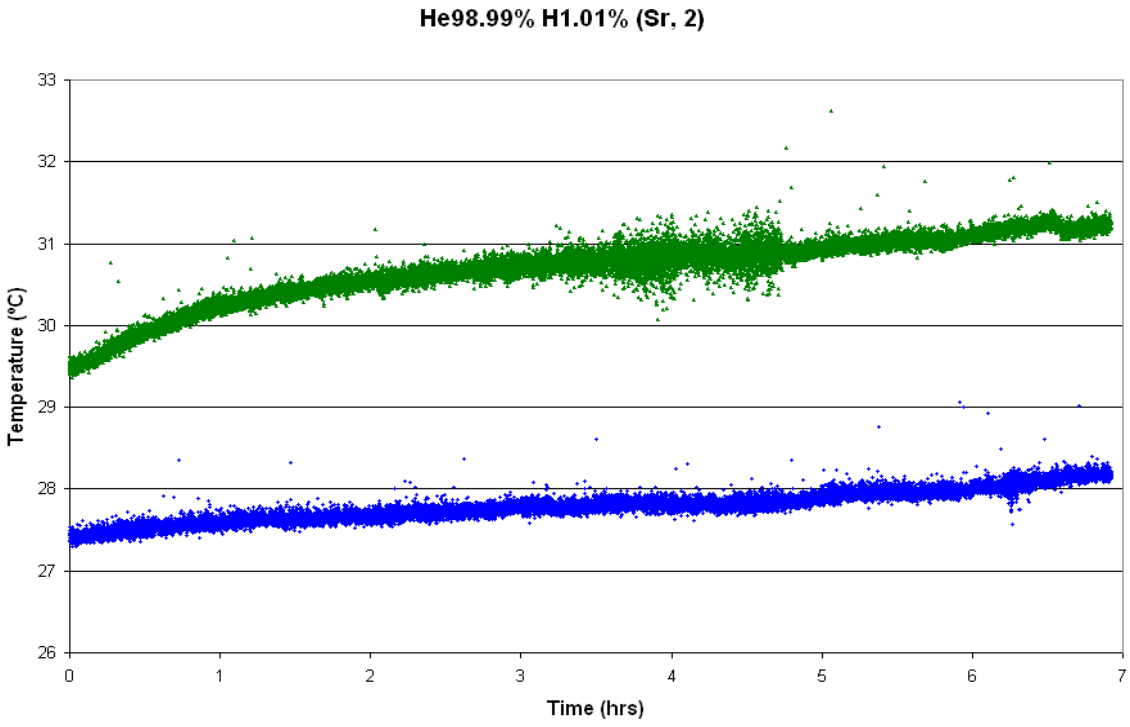
He98.99% H1.01% (Sr, 2)
Temperature (°C)
Time (hrs)
33
32
31
30
29
28
27
26
0
1
2
3
4
5
6
7

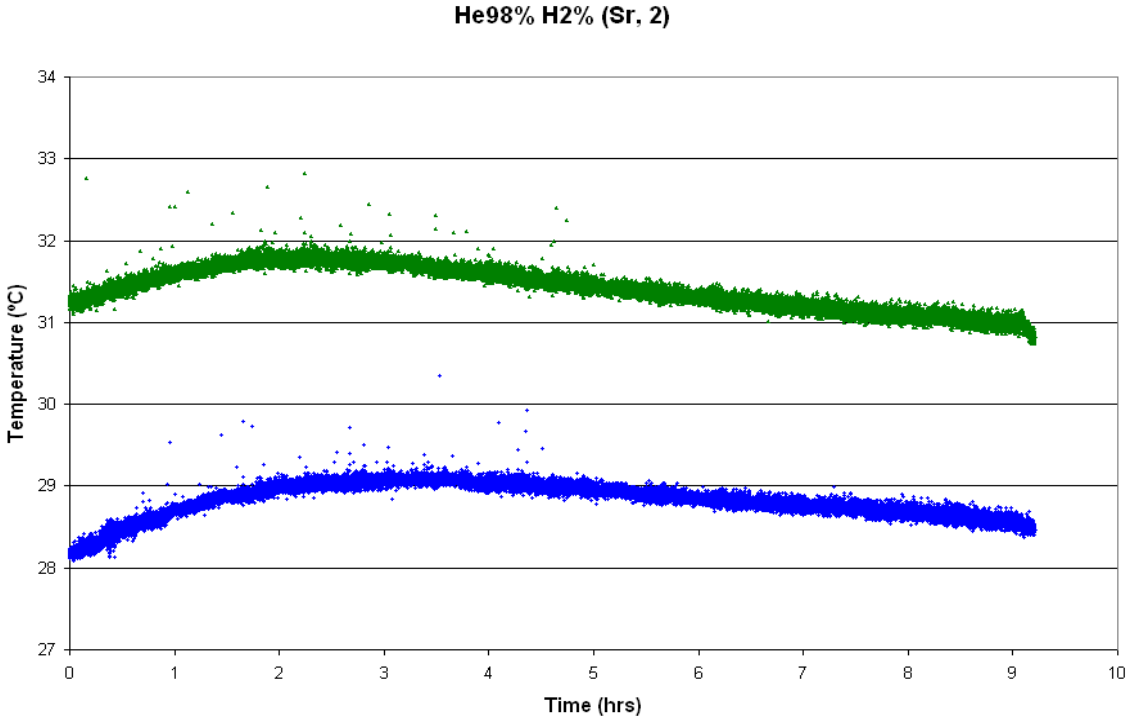
He98% H2% (Sr, 2)
Temperature (°C)
Time (hrs)
34
33
32
31
30
29
28
27
0
1
2
3
4
5
6
7
8
9
10

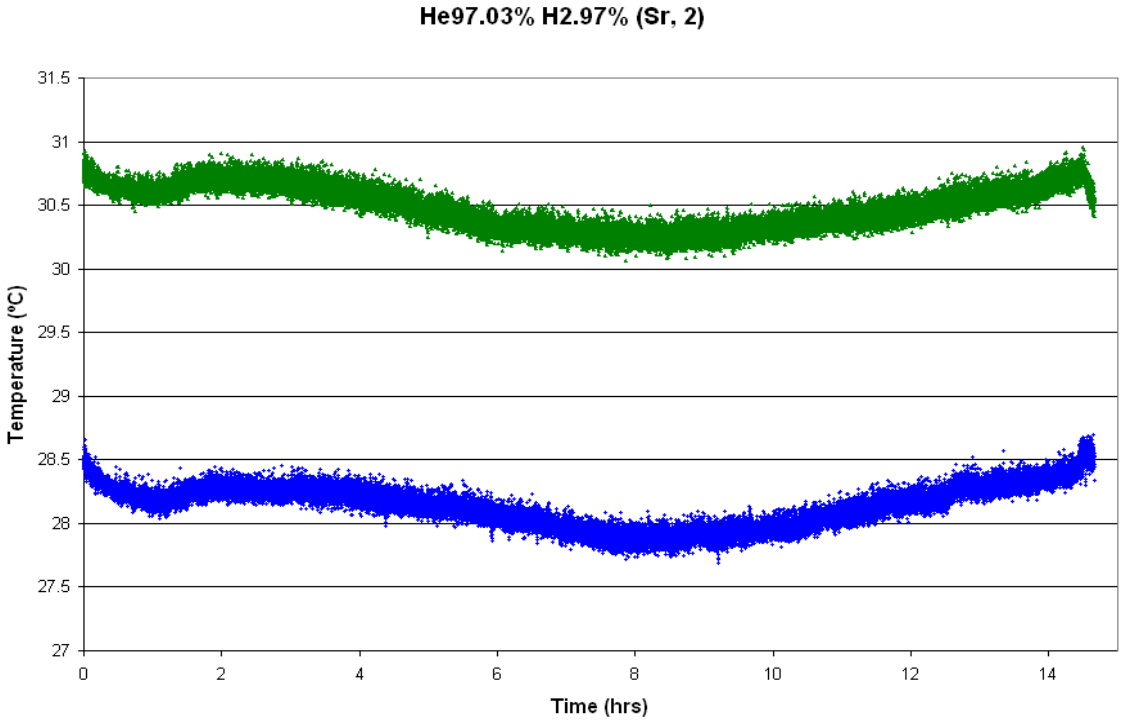
He97.03% H2.97% (Sr, 2)
Temperature (°C)
Time (hrs)
31.5
31
30.5
30
29.5
29
28.5
28
27.5
27
0
2
4
6
8
10
12
14

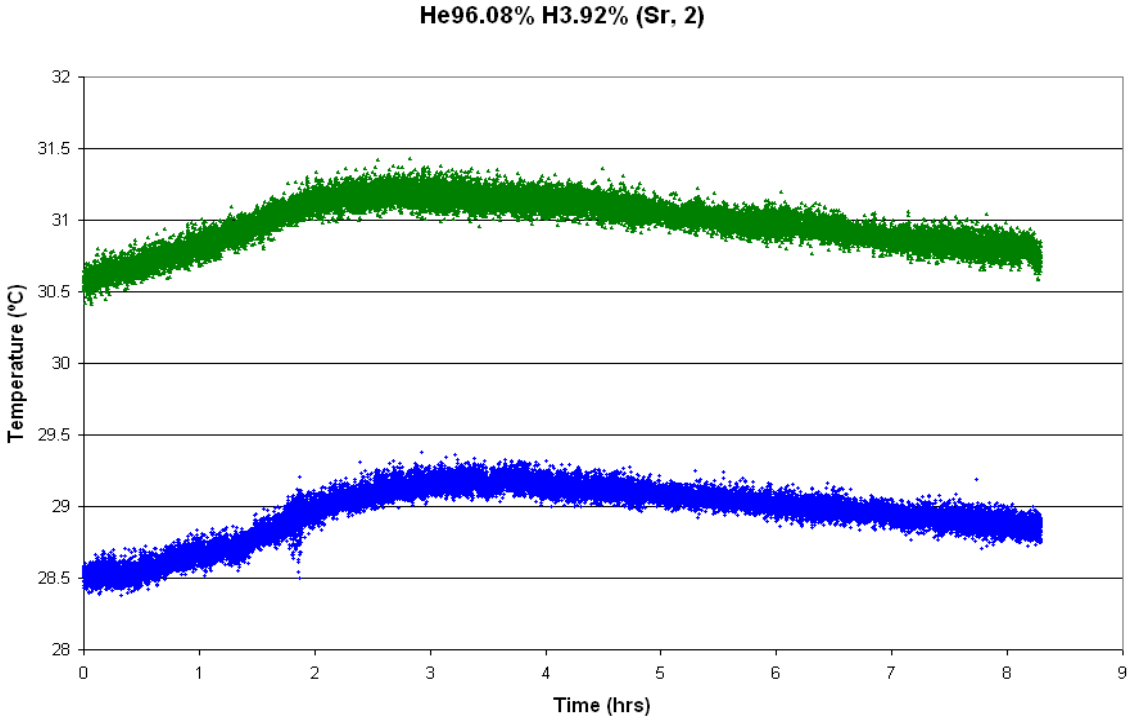
He96.08% H3.92% (Sr, 2)
Temperature (°C)
32
31.5
31
30.5
30
29.5
29
28.5
28
0
1
2
3
4
5
6
7
8
9
Time (hrs)

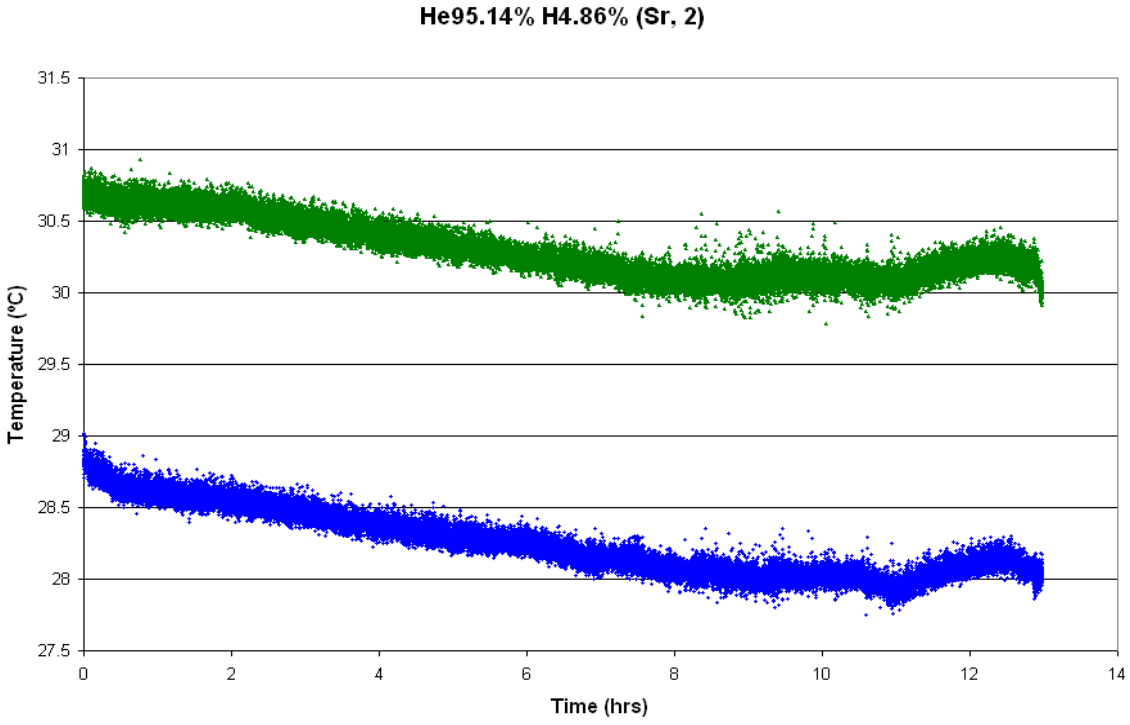
He95.14% H4.86% (Sr, 2)
Temperature (°C)
31.5
31
30.5
30
29.5
29
28.5
28
27.5
0
2
4
6
8
10
12
14
Time (hrs)

Appendix E: Data Set 2; Spectral Data

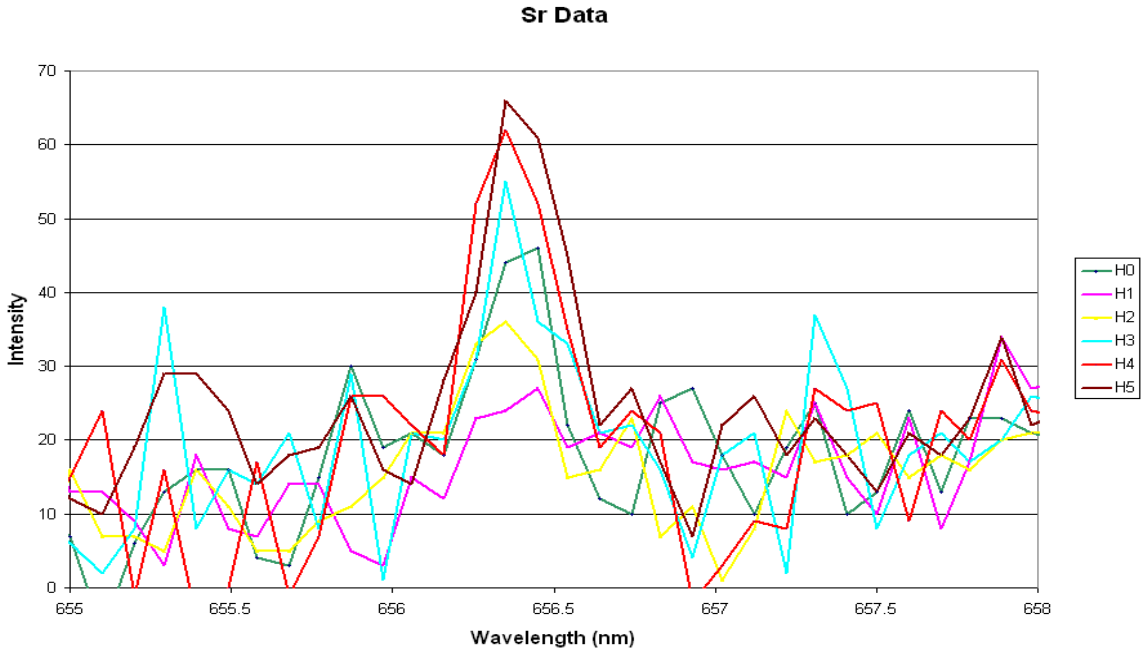

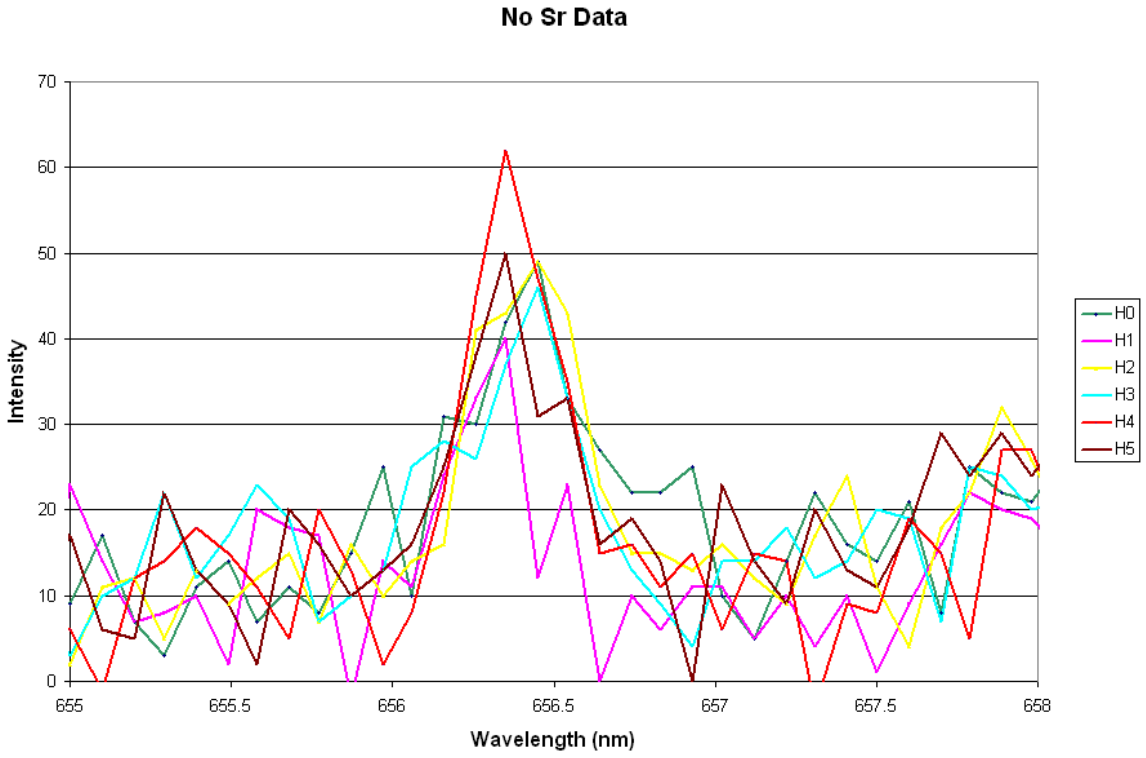

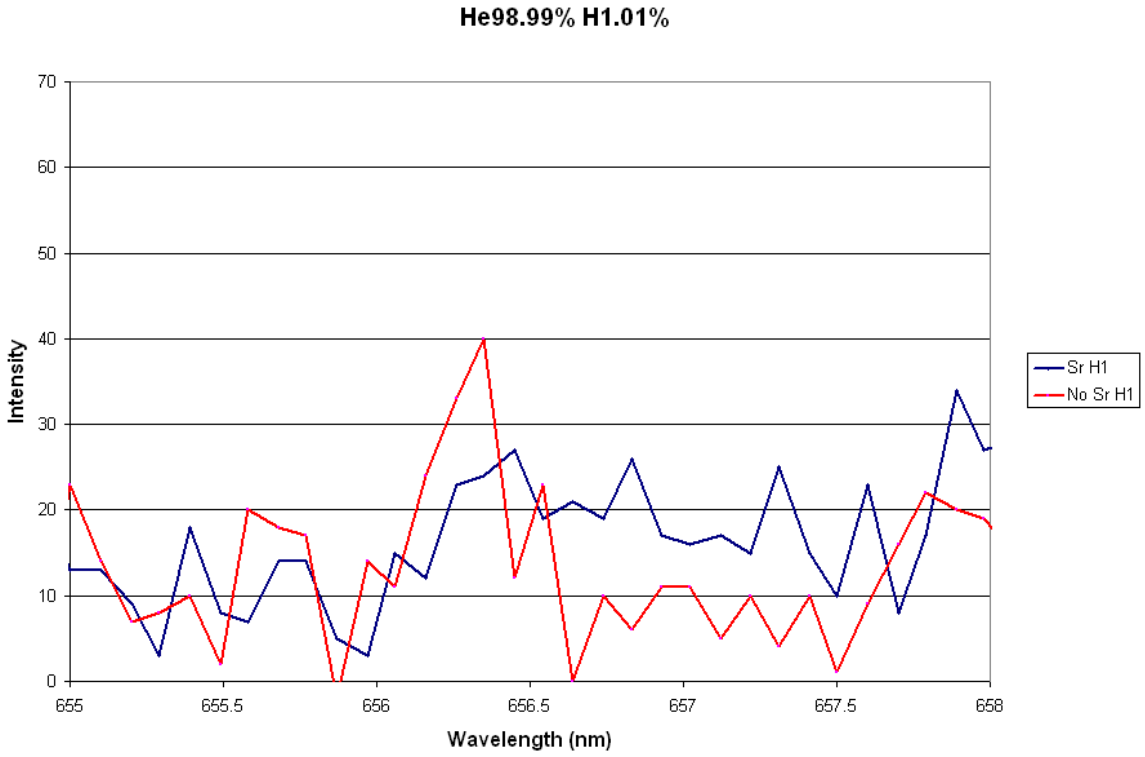
He98.99% H1.01%
Intensity
Wavelength (nm)
Sr H1
No Sr H1
70
60
50
40
30
20
10
0
655
655.5
656
656.5
657
657.5
658

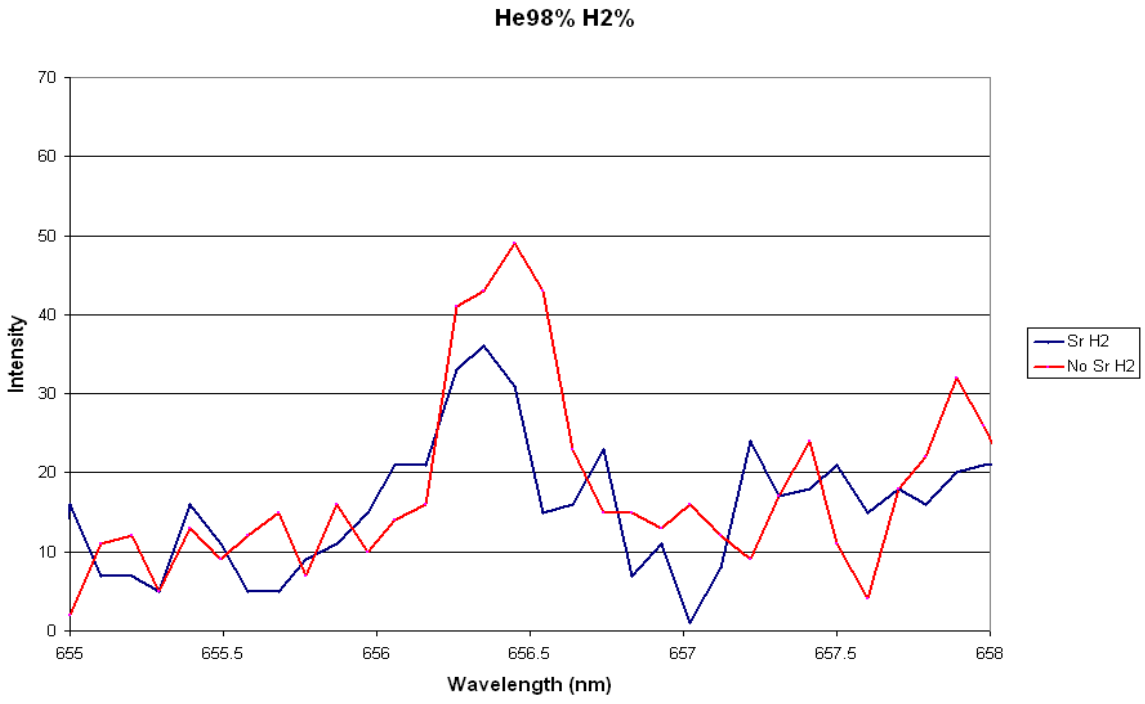
He98% H2%
Intensity
Wavelength (nm)
Sr H2
No Sr H2
70
60
50
40
30
20
10
0
655
655.5
656
656.5
657
657.5
658

He97.03% H2.97%

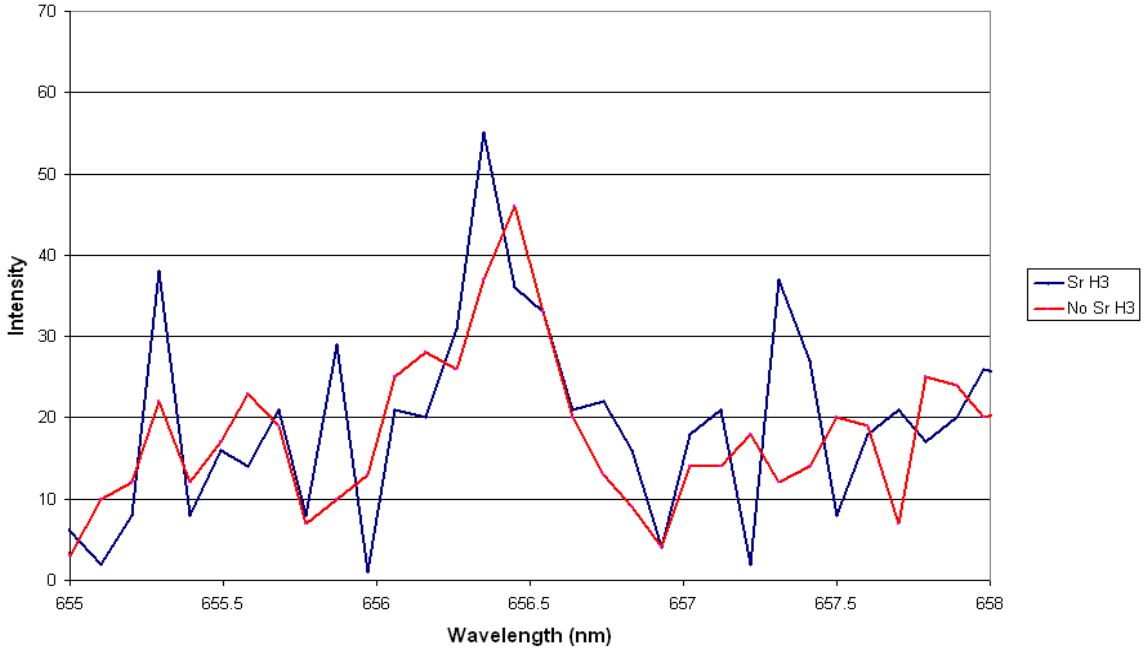

He96.08% H3.92%

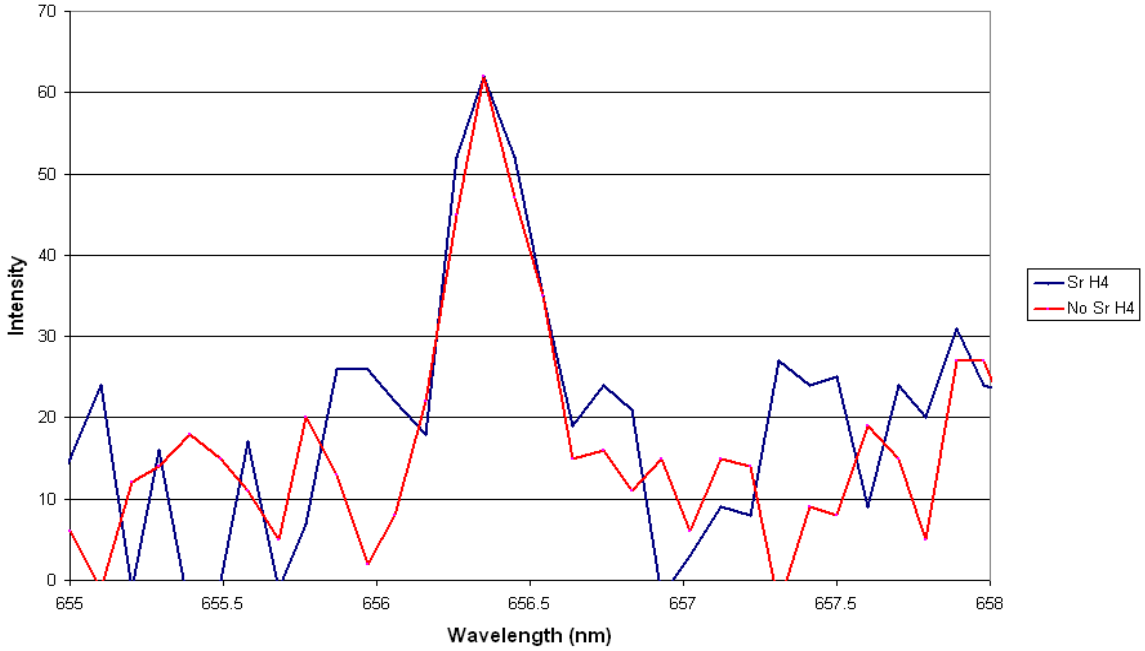

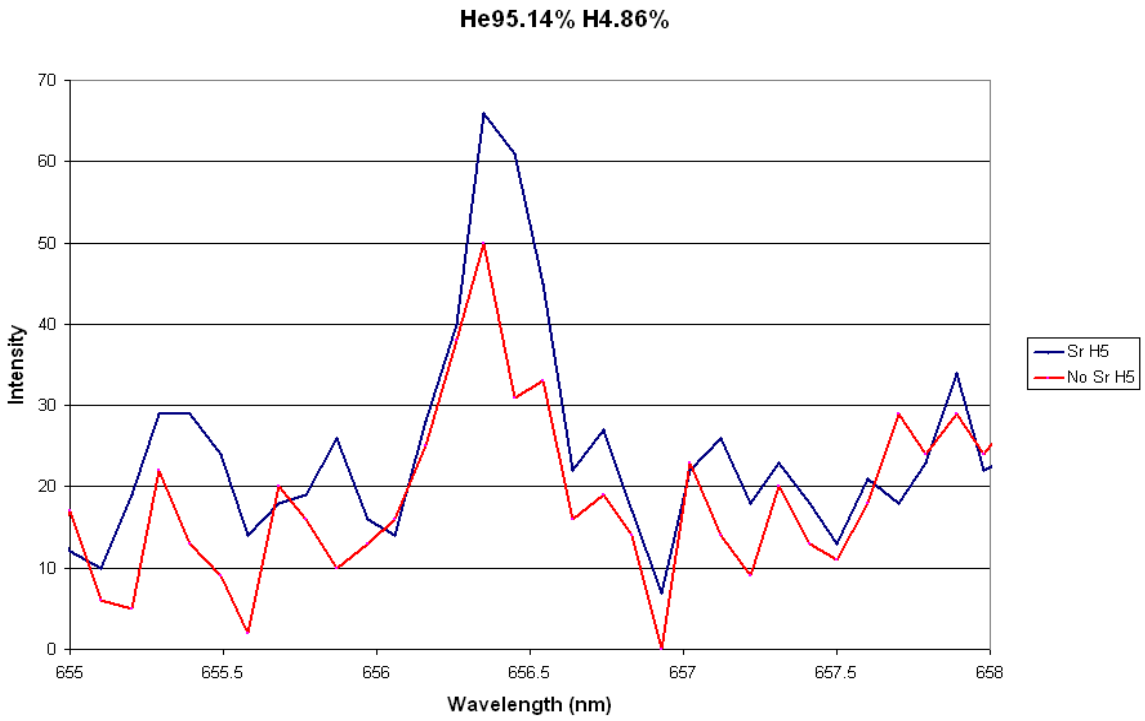
He95.14% H4.86%
Intensity
70
60
50
40
30
20
10
0
655
655.5
656
656.5
657
657.5
658
Wavelength (nm)
Sr H5
No Sr H5

Appendix F: Maple Code

```
>
> restart;
>       #Parameters are set
>
>   #electron mass
> m := 9.1094E-31
>
>   #Boltzmanns constant
> k := 1.3807E-23
>
>   #inlet temperature
> Tin := 305
>
>   #inlet pressure
> Pin := 500
>
>   #atom number density
> nn := Pin / (k · Tin)
>
>   #frequency of power supply
> w := 5E3 · 2 · π
>
>   #voltage
> V := 1745.7
>
>   #current
> Current := .01864
>
>   #phase shift
> Y := 6.12 · π / 9
>
>   #permittivity of free space
> E := 8.854E-12
>
>   #electron charge
> e := 1.6022E-19
>
>   #dielectric constant of garolite
> Kg := 4.2
>
```

>

#length, inner electrode radius, garolite radius, and outer electrode radius

> $l := .3$

> $a := .0025$

> $b := .00325$

> $c := .025$

>

> #electron plasma frequency

> $wp := \mathrm{sqrt}\left(\frac{e^2 \cdot ne}{E \cdot m} \right)$

>

> #Iterate to find electron plasma temperature

> $wo := \frac{4.86}{99}$

> $Te := .5695$

> $ven := nn \cdot \mathrm{sqrt}\left(\frac{8 \cdot Te \cdot 1.602\mathrm{E}-19}{3.14159265\, m} \right) \cdot 6.24\mathrm{E}-20 + (\mathrm{wo}) \cdot nn \cdot \mathrm{sqrt}\left(\frac{8 \cdot Te \cdot 1.602\mathrm{E}-19}{3.14159265\, m} \right) \cdot 13\mathrm{E}-20$

> $Saha := \mathrm{sqrt}\left(2.4\mathrm{E}21 \cdot \left((11600 \cdot (Te))^{\frac{3}{2}} \cdot \exp\left(-\frac{24.587}{Te} \right) \right) \cdot nn \right)$

>

> #Iterate to find maximum sheath thicknesses

> $solve\left(-V = \frac{e \cdot 5.21557929010^{15}}{2 \cdot E} \left(-\frac{sa1^2}{2} + \frac{b^2}{2} + b^2 \cdot \ln\left(\frac{sa1}{b} \right) \right), sa1 \right)$

> $solve\left(-V = \frac{e \cdot 5.28007021810^{15}}{2 \cdot E} \left(-\frac{c^2}{2} + \frac{(sb2)^2}{2} + sb2^2 \cdot \ln\left(\frac{c}{sb2} \right) \right), sb2 \right)$

> $\mathrm{d} := \mathrm{b}$

> $x := 0.0186614671$

>

> #Solve for electron number density

> $\beta := \frac{1}{w \cdot 2 \cdot \pi \cdot l \cdot E} \cdot \left(\frac{\left(w^2 \cdot wp^2 \right) \cdot \ln\left(\frac{\mathrm{x}}{\mathrm{d}} \right)}{\left(\mathrm{w}^4 + ven^2 \cdot w^2 \right)} + \frac{ln\left(\frac{b}{a} \right)}{Kg} - \ln\left(\frac{\mathrm{x}}{\mathrm{d}} \right) \right)$

> $solve\left(\beta = \frac{V}{Current} \cdot \sin(Y), ne \right)$

> >
>

#Put electron number density into sheath thickness equations and iterate

>